POLITECNICO DI MILANO
Master of Science in Space Engineering
Department of Aerospace Science and Technology

Discrete Active Disturbance Rejection Control for Halo Orbit Station-Keeping

SME Lab
(Space Missions Engineering Laboratory)

Supervisor:
Prof. James Douglas Biggs

MSc Student:
Wadee Khoury
ID: 913756

Academic Year 2019/2020

This page was intentionally left blank

Acknowledgement

"Let your light shine before men, that. they may see your good works, and. glorify your Father which is in heaven."

Matthew 5:15–16

The strongest foundation for all of my achievements, my parents, Riad and Khitam, and my siblings, Fadi and Sarah. I am eternally thankful for your invaluable love and support. Without your guidance and encouragement, I would not be where I am today.

This thesis is also dedicated to my wonderful fiancé, Hala. When it felt like no one else in the world could understand what I was going through, I knew that you actually did. A true blessing in my life, I could not have done this without you.

I want to extend my immense gratitude to my supervisor, Professor James Douglas Biggs. Thank you for providing me with the interesting opportunity to work on this project. Your thoughts, encouragement, advice, and support have been invaluable to my research and time at PoliMi. I hope our paths will cross again in the future.

To all the teachers of Politecnico di Milano, thank you for transmitting your invaluable knowledge to me with such passion and motivation. Over two years now, being taught and educated by such outstanding staff members, I can confidently say *the world is my oyster*.

A person is nothing without true friends, thank you for providing me with your unfailing support and continuous encouragement throughout my years of study and through the process of writing this thesis. In particular, Fadi Assad and Fareed Jarbouh, for their help and contribution to editing the thesis.

Special thanks go to Father Hugo and Bishop Georges Abou Khazen, who constantly supported me through the various obstacles I faced during

my stay in Milan. My gratitude goes also for the whole family of Collegio Universitario Bertoni, especially Dr. Andrea Inzaghi, who helped and hosted me for two years, presenting the true meaning of Italian hospitality.

I would have never been able to achieve this dream without the Italian Government who granted me twice the MAECI scholarship. What an honor to be among the few students to whom such a great opportunity was awarded. Thank you, Italy.

I also dedicate this thesis to Amphinicy Technologies Sàrl, Luxembourg, one of the greatest IT space-oriented companies. Thank you for accepting me as an intern, especially Mr. Frane Miloš, CEO, and Mr. Juanjo Garrido Serrato, senior sat-comm engineer. I am thankful for your supervision and assistance, not only concerning the internship but also for your hospitality and the wonderful time I spent in Luxembourg.

Contents

This page was intentionally left blank

List of Figures

This page was intentionally left blank

List of Tables

This page was intentionally left blank

Abstract

This thesis addresses the problem of deep-space station-keeping of an L_2 elliptic halo orbit in the Earth-Moon system. A robust control approach is developed to guarantee closed-loop stability in the presence of unmodeled dynamics and disturbances, such as solar radiation pressure (SRP) and station-keeping errors. The novelty of this control approach compared to the state of the art approaches is its applicability in discrete-time using a few tuning parameters, thus, its suitability for digital implementation and impulsive thrusters.

In the proposed approach, a reference periodic halo orbit is first computed in the elliptical restricted three-body problem (ER3BP) using nonlinear programming optimization methods. Discrete-time finite-horizon linear quadratic regulator (DLQR) is then designed for optimal maneuver calculations required to overcome the instabilities inherited in the reference solution. Disturbance estimation is next investigated using a discrete linear extended state observer (DLESO) that was adopted for impulsive control. The novel discrete active disturbance rejection control (DADRC) is finally structured by extending the calculated maneuver with a disturbance rejection term.

The proposed control approach was tested in several simulation scenarios under the presence of the SRP disturbance, the station-keeping constraints, and the station-keeping errors. Two Monte-Carlo simulations were also performed for a qualitative examination of the effect of station-keeping errors. Using the novel DADRC, both the cost and the position deviation were reduced by 25-35 [%] compared to the DLQR. The results, therefore, reflect the success of the DLESO in adding robustness and enhancing the performance of the DLQR against external disturbance and measurement noises.

This page was intentionally left blank

Chapter 1

Introduction

As the space age evolves, scientific and exploratory missions incorporate spacecraft in a continually expanding variety of tasks. Most missions, however, require spacecraft to orbit one primary celestial body, such as the Sun, Earth, Moon, and Mars. In this two-body system, the orbital dynamics is represented by a single dominant gravitational field while neglecting other influences. One of the main advantages of employing the two-body dynamics is the closed-form analytical solution. This model, therefore, serves as a successful preliminary design tool over a wide range of mission scenarios, such as a satellite orbiting the Moon. To increase the accuracy of the dynamical model, additional forces and attracting bodies can be treated as perturbations in the governing equations.

As the world is racing towards space colonization, mining, and exploration, the simple two-body model is not sufficiently accurate to allow for the prediction and analysis of the true motion of the spacecraft. Therefore, an additional gravitational body can be included to increase the fidelity of the dynamical model, resulting in a formulation based of three gravitational bodies. A good example is the International Sun-Earth Explorer-3 (ISEE-3) spacecraft, launched from Earth on August 12, 1978, and injected into a halo orbit approximately three months later [1]. For about three and a half years, ISEE-3 remained in this three-dimensional (nominally) periodic orbit under the influence of interacting gravitational forces originating from the Sun and the Earth-Moon. ISEE-3 is especially notable as the first man-made object to be placed in this type of orbit. Following the ISEE-3, many similar missions were planned and successfully flown [2], encouraging the development of new and innovative trajectory concepts that provide low-cost solutions to demanding mission requirements.

In reality, spacecraft will deviate from any predefined nominal orbit due

to unknown or unexpected forces not represented in the dynamical model, as well as instabilities inherited in the reference solution. To keep the spacecraft close to its nominal path, station-keeping strategies must be introduced without interfering with the mission constraints or scientific requirements. This research effort is focused on the analysis and development of an innovative station-keeping approach that is suitable for digital implementation and impulsive thrusters.

1.1 Previous Contributions

1.1.1 Multi-Body Dynamics

With the publication of the *Principia* in 1687, Sir Isaac Newton (1643-1727) recorded the laws that govern the motion of N-bodies moving under the Universal Gravitational Law. Thus began the search for an elusive analytical solution to the complex motion that governed the heavens [3]. Years later, in 1722, Leonhard Euler (1707-1983) simplified a model representing the N-body problem with the formulation of the Circular Restricted Three-Body Problem (CR3BP) [4]. A truly key innovation, the view of the problem from the perspective of a rotating frame enabled significant progress. Then, with the assumption of an infinitesimal third body and primary bodies in circular orbits about their common barycenter, understanding the orbital motion drastically increased. Joseph-Louis Lagrange (1736-1813) demonstrated the existence of the triangular equilibrium solutions to the CR3BP in 1772, the same year that Euler recognized the existence of the collinear libration points; the emergence of the equilibrium points led to additional understanding and insight into the problem. Over sixty years later, in 1836, an integral of the motion in the CR3BP, now known as the Jacobi integral or Jacobi constant, was noted by Carl Gustav Jacob Jacobi [5]. This integral, or constant of the motion, bolstered insight into this dynamical regime and led to the recognition of the existence of bounding surfaces of allowable third body motion, known as the zero velocity curves, shown by Hill in 1878 [6].

Within the second volume of *Les Méthodes Nouvelles de la Mécanique Céleste*, Poincaré identified that no additional algebraic integrals of the motion exist in the CR3BP [7]. Since then, countless authors have explored the complex motion in this dynamical regime. In 1881, a technique to visualize complex solutions in the CR3BP was contributed by Henri Poincaré, now recognized as Poincaré map [5]. This tool, not directly utilized by Poincaré due to computational limitations in the early 1900s, offers invaluable insight into dynamical systems. However, not until 1978 was a mission proposed

to exploit the multi-body dynamical motion; the ISEE-3 spacecraft was inserted into a Sun-Earth L_1 halo orbit and was maintained for almost three and a half years. Since then, an increased number of missions incorporated these types of orbits including; missions in the Earth-Moon system, such as ARTEMIS (L_1 and L_2) [8] and Chang'e 5-T1 (L_2) [9]; missions in the Sun-Earth system, such as SOHO, ACE, WIND, and Genesis (L_1) [10, 11] and WMAP (L_2) [12]. Meanwhile, many missions have been proposed to be studied and launched in the future including, ones of relevant importance in this investigation, missions to the Earth-Moon L_2 libration point; EQUULEUS mission [13], proposed by JAXA and the University of Tokyo to NASA, that will help scientists understand the radiation environment in the region of space around Earth; LUMIO mission [14, 15, 16], proposed by a consortium of Politecnico Di Milano and other institutions, that will observe, quantify, and characterize meteoroid impacts on the lunar farside.

1.1.2 Differential Corrections

Differential corrections methods, which date back to Newton's *Principia*, are a fundamental aspect of multi-body trajectory design [3]. Many different formulations of differential corrections algorithms exist within the context of solving two-point boundary value problems. Authors such as Keller [17], as well as Roberts and Shipman [18, 19], produce shooting methods formulations in which a solution to a two-point boundary value problem is determined by integrating an appropriate initial value problem [20]. The advent of modern computers enabled the application of shooting methods to solve complex problems, e.g., trajectory design in the multi-body dynamical regime. A free-variable and constraint method, one specific formulation of a shooting scheme, as detailed by both Pavlak [21] and Zimovan [22], is implemented in this investigation.

1.1.3 Periodic Orbits

As early as 1881, Poincaré demonstrated the existence of an infinite number of periodic solutions in the three-body problem [7]. Since then, many authors have focused on the construction and characterization of these orbits. As an example, Moulton's collection of analytical methods for approximating periodic motion near the libration points in 1920 inspires continuing efforts [23]. However, large computational advances at the onset of the computer era have allowed many periodic solutions to be computed formally only within the last half-century. As recent samples of such efforts, Grebow characterized and defined families of related periodic solutions in the CR3BP in an

application to lunar south pole coverage [24], meanwhile, Schlei developed an algorithm to identify many previously unknown planar periodic solutions and provided a significant number of examples [25].

A specific type of three-dimensional periodic orbit possessing a constant line of sight to the Earth, halo orbits first appeared in the literature in work by Farquhar in 1970 [26] and Kamel [27] in 1973. Breakwell and Brown, in 1979, demonstrated the existence of a family of related solutions, the family denoted as the L_2 halo orbits; a similar family bifurcating from an L_1 Lyapunov orbit also emerged. The L_1 halo family is characterized in the work by Breakwell and Brown and is also continued with representative periodic orbits from the planar Lyapunov orbit towards the increasingly three-dimensional orbits in the vicinity of the smaller primary [28]. Later in 1980, Richardson constructed the third-order analytical solution of halo orbits in the CR3BP using Lindstedt–Poincaré method in the truncated system [29]. Howell extended the families of L_1 and L_2 halo orbits to other systems in addition to offering a characterization of the L_3 halo family [30, 31]. The dynamical system of the CR3BP was explored by many following authors, such as Barden, Lo, Koon, and Gomez [32, 33, 34, 35].

In 1920, Moulton also investigated the periodicity in the elliptical restricted three-body problem (ER3BP). Szebehely later in 1967 simplified the dynamical model derivation of the ER3BP by keeping the primaries at fixed locations through introducing the rotating-pulsating frame [5]. Shortly after, in 1969, Broucke used Moulton's criterion to compute planar periodic orbits in the ER3BP using continuation methods [36]. Heppenheimer then utilized the Jacobi elliptic functions to study the out-of-plane motion in the ER3BP and used Lindstedt–Poincaré method to obtain a third-order expansion [37]. In 1980, Ichtiaroglou [38] and Michalodimitrakis [39] extended Moulton's criteria to three-dimensional orbits. Moreover, Sarris, in 1989, continued vertical Lyapunov orbits starting from orbits in the CR3BP and studied their stability [40]. More recently, Campagnola et al. succeeded in computing periodic halo orbits in the ER3PB, which they called elliptic halo orbits since they bifurcate from special halo orbits of the CR3BP [41]. Hou and Liu in 2011 constructed analytical expansion of collinear libration point orbits in the ERTBP by using Lindstedt–Poincaré method [42]. The characterization and stability analysis of orbits in the ER3BP was continued by many other authors, such as Gurfil, Meltzer, and Kasdin [43, 44], Antoniadou and Voyatzis [45], and Mahajan and Pernicka [46]. In particular, Peng and Xu [47] applied nonlinear programming optimization methods to generate periodic orbits in the ER3BP at a lower computational cost than differential correction methods.

1.1.4 Station-Keeping

Since the late 1970s, supported by the aforementioned research and studies, libration points and bounded trajectories around them have become of practical interest, allowing several convenient and useful properties Keplerian motion does not possess. The most attractive mission targets are periodic and quasi-periodic trajectories around collinear libration points. However, the associated dynamics are unstable, requiring effective methods of station-keeping to keep a spacecraft within the vicinity of the nominal trajectory.

Shirobokov e al. [2] distinguished two categories of station-keeping methods; the first category (I) includes those methods that effectively exploit insights into the three-body dynamical effects, mainly by the Floquet theory. These methods are aimed at eliminating the unstable component of motion, e.g. by removing the unstable Floquet modes associated with the reference orbit; the second category (II) represent the advanced control theory methods in application to the station-keeping problem. These techniques differ in their approaches to solving optimal control problems and are independent of the specific character of dynamics. Inside each categories, further classification is made between the continuous control (cont.) techniques and the impulsive control (impul.) techniques. Table 1.1 summarizes most of the station-keeping method applied in literature until date.

Station-keeping is also recognized depending on the control device used to perform the maneuver. As most of the flown mission uses chemical propulsion to carry on the required impulse, continuous propulsion was also investigated in literature by several authors, such as Biggs and Narula [73, 74] who employed low thrust electric propulsion. Researchers, such as Cui, Huang, Biggs e al., also explored the utilization of solar radiation pressure to continuously control the spacecraft using solar sails and reflective devices [87, 88, 89]. Meanwhile, Biggs e al. have recently achieved the station-keeping using a hybrid approach of a solar sail supported by a single-degree-of-freedom electric thruster [90].

1.2 Current Work

This investigation focuses on the design and station-keeping of halo orbits in the Earth-Moon system. In particular, an L_2 halo orbit was selected because of its complex dynamical behavior comparing to other collinear points [91], which makes its station-keeping more challenging for orbital controllers. The outcome of this work is expressed in two main deliverables; the first one is to provide a comprehensive reference for the calculation of periodic halo

Table 1.1: Summary of previous control methods.

Cat.	Method	Type
I	Pole-placement technique [48]	cont.
	Use of the characteristic exponent [49]	cont.
	Elimination of instability in linear dynamics [50, 51]	impul.
	Minimization of integral characteristics of instability [52]	impul.
	Floquet mode approach [53, 54, 55, 56, 57, 58, 59]	impul.
	Method of Osculating Parameters [60]	impul.
II	LQR techniques [61, 62, 63, 64, 65]	cont./impul.
	Nonlinear regulation techniques [66, 67]	cont.
	Backstepping technique [68, 49]	cont.
	Nonlinear and linear programming techniques [64, 69]	cont.
	Disturbance accommodating control [70, 71]	cont.
	Disturbance rejection control [72, 73, 74]	cont./impul.
	Model predictive control [75, 76, 77]	cont.
	H_2 and H_∞ Control Techniques [78, 79, 80]	cont.
	Targeting strategies [81, 82, 83, 57, 58, 84, 85]	impul.
	Sliding mode control [65]	impul.
	Chebyshev-Picard iterations [86]	impul.

orbits in the ER3BP; the second is to construct and verify a novel impulsive control method that is easy to tune and suitable for digital implementation and impulsive thrusters.

This investigation is carried out following the work of both Gómez e al. [65], who investigated the design of discrete LQR and sliding mode controllers, and Gao e al. [72], who designed an active disturbance rejection control (ADRC) using both continuous and discrete nonlinear extended state observers. Both studies investigated the design of robust discrete controllers for station-keeping. However, their approaches require tuning many parameters, which is difficult to implement, and have both switching and sliding functions that may cause chattering. The proposed control method, therefore, offers a novel robust discrete controller that is easy to implement and requires a fewer tuning parameters. A discrete finite-horizon linear quadratic regulator (DLQR) is first designed similar to [65]. Following, a novel discrete linear extended state observer (DLESO) is investigated and adopted for impulsive control. The suggested discrete active disturbance rejection control (DADRC) is then structured by extending the maneuver calculated using the DLQR with a disturbance rejection term obtained from the DLESO. The novel DADRC is found to provide increased robustness, comparing to the

DLQR, against uncertainties, disturbances, and measurement noises, such as SRP and station-keeping errors. This investigation is organized as follows:

- **Chapter 02:** Dynamical Models - In this chapter, the mathematical models that describe the motion of the spacecraft in the CR3BP were derived and presented alongside the utilized reference frames. The differential equations were then formulated within the context of the ER3BP by including the eccentricity of the moon's orbit. The solar radiation pressure perturbation was discussed later and its effect embedded into the dynamics. Finally, the mathematical model of the thruster was developed for the case of impulsive control and also added to the dynamics.

- **Chapter 03:** Differential Correction - In this chapter, the concept of the State Transition Matrix (STM) was explored for both the CR3BP and ER3BP. Single and multi-segment shooting methods were then described and their corresponding mathematical representations were derived. Orbit continuation was presented later to illustrate the shift from the CR3BP to the ER3BP. Finally, the discussed strategies were applied for both the CR3BP and the ER3BP to obtain periodic halo orbits.

- **Chapter 04:** Station-Keeping - In this chapter, several methods were first discussed to represent the reference orbit. Later, the main constraints and errors applied in the station-keeping problem were introduced and calculated. A DLQR was then discussed and designed for optimal maneuver calculations. A novel DLESO was next developed for disturbance estimation and adopted for the case of impulsive control. Finally, the structure of DADRC was presented and discussed.

- **Chapter 05:** Simulation and Results - In this chapter, the simulation model was first introduced with the main parameters. Several station-keeping scenarios were simulated later to differentiate between the DLQR and DADRC and to highlight the advantages obtained after adding the DLESO. Finally, two Monte-Carlo simulations were performed for a qualitative examination of the effect of station-keeping errors.

- **Chapter 06:** Conclusion - In this chapter, a summary of the current research, results, and future recommendations is introduced.

This page was intentionally left blank

Chapter 2

Dynamical Models

As the objectives of missions become more ambitious, the simple two-body model is not sufficiently accurate to allow for prediction and analysis of the true motion of the spacecraft. Since the inclusion of an additional gravitational body can increase the fidelity of the dynamical model, exploring the CR3BP provides a general understanding of the multi-body design space. In the Earth-Moon system, however, the eccentricity of the Moon's orbit around the Earth presents a large perturbation source. Therefore, the differential equations are formulated within the context of the ER3BP to allow for a more accurate preliminary investigation. The solar radiation pressure perturbation is also discussed and embedded into the dynamics alongside the propulsion system, which increased the fidelity of the presented model.

2.1 Reference Frames

Several reference frames are considered throughout this analysis for both computation and visualization purposes. In this section, a brief description of these frames and their corresponding transformations are presented.

2.1.1 Inertial Frame

This frame is centered at the barycenter of the two primaries, B, as shown in Figure 2.1, and indicated using the subscript I. The $\hat{X}$-axis is directed towards the right side from the barycenter, $\hat{Y}$-axis is perpendicular upwards, and the $\hat{Z}$-axis is perpendicular to both according to the right-hand rule (RHR).

2.1.2 Rotating Frame

This frame is also centered at the barycenter, as shown in Figure 2.1, and indicated using the subscript R. The $\hat{x}$-axis is directed from the larger primary to the smaller one, $\hat{y}$-axis is perpendicular upwards, and the $\hat{z}$-axis is perpendicular to both according to the RHR.

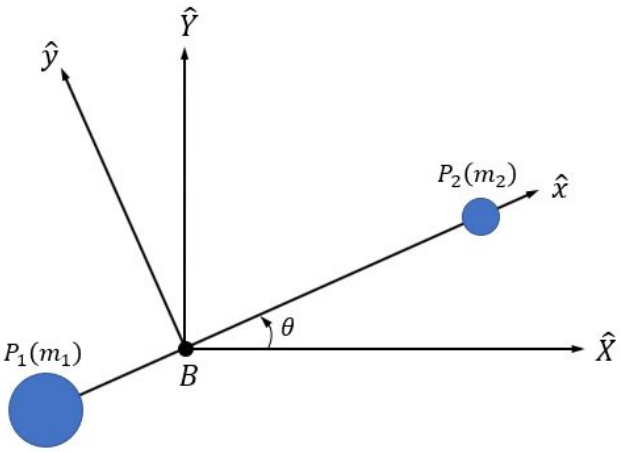

Figure 2.1: The inertial and the rotating frames centered at the barycenter of masses m_1 and m_2.

2.1.3 Transformations

After defining the inertial and rotating frames, shown in Figure 2.1, the ability to transform the solution between the two frames is required for visualization purposes. Since the $\hat{X}\hat{Y}$-plane and the $\hat{x}\hat{y}$-plane coincide for all time, and assuming that both frames are equivalent at time zero, the orientation of the rotating frame with respect to the inertial frame is described simply by the angle, θ. Accordingly, the transformation of a position vector in the rotating frame, $\mathbf{R}_R$, to the inertial frame is expressed as:

$$\mathbf{R}_I = \mathbf{T}_{\mathbf{R/I}}\mathbf{R}_R \tag{2.1}$$

while the corresponding velocity vector, $\dot{\mathbf{R}}_I$, is expressed as:

$$\dot{\mathbf{R}}_I = \dot{\mathbf{T}}_{\mathbf{R/I}}\mathbf{R}_R + \mathbf{T}_{\mathbf{R/I}}\dot{\mathbf{R}}_R \tag{2.2}$$

where the transformation matrix and its time derivative are given as:

$$\mathbf{T}_{\mathbf{R/I}} = \begin{bmatrix} \cos\theta & -\sin\theta & 0 \\ \sin\theta & \cos\theta & 0 \\ 0 & 0 & 1 \end{bmatrix} \tag{2.3}$$

$$\dot{\mathbf{T}}_{\mathbf{R/I}} = \dot{\theta} \begin{bmatrix} -\sin\theta & -\cos\theta & 0 \\ \cos\theta & -\sin\theta & 0 \\ 0 & 0 & 0 \end{bmatrix} \tag{2.4}$$

Defining a state vector that includes both the position and velocity vectors, it possible to construct the full transformation matrix as:

$$\begin{bmatrix} \mathbf{R} \\ \dot{\mathbf{R}} \end{bmatrix}_I = \begin{bmatrix} \mathbf{T}_{\mathbf{R/I}} & \mathbf{0}_{3\times3} \\ \dot{\mathbf{T}}_{\mathbf{R/I}} & \mathbf{T}_{\mathbf{R/I}} \end{bmatrix} \begin{bmatrix} \mathbf{R} \\ \dot{\mathbf{R}} \end{bmatrix}_R \tag{2.5}$$

Meanwhile, the transformation from the inertial to the rotating frame is performed by inverting Equation (2.5).

Although the full transformation matrix in Equation (2.5) transforms the state vector to the inertial frame centered at the barycenter, if desired, it is possible to center the inertial frame at one of the primaries. To achieve this, a simple translation in the rotating frame from the barycenter to the desired primary is first performed, mainly by shifting along with the $\hat{x} - axis$, before applying the transformation.

2.2 Circular Restricted Three-Body Problem

The general three-body problem is defined as the inclusion of three bodies, P_1, P_2, and P_3 of masses m_1, m_2, and m_3, respectively, where each is gravitationally influencing the others. Since the Earth-Moon mass ratio is large compared to other planet-moon systems, a spacecraft in cislunar space is strongly influenced by both bodies simultaneously. Consequently, the CR3BP serves as a particularly effective model in the preliminary design for applications within the Earth-Moon system.

2.2.1 Simplifying Assumptions

Modeling the system behavior of the general three-body problem requires three second-order vector differential equations. Hence, 18 state variables are necessary to solve the problem while only ten integrals of the motion are known to exist when formulating in terms of the inertial frame. Consequently, an analytical closed-form solution is no longer achievable and numerical integration is required to explore the solution space. To further simplify the problem, the following assumptions lead directly to the reduced CR3BP formulation:

1. The bodies are modeled as centrobaric point-masses only capable of translational motion.

2. The third gravitational body, P_3, possesses a significantly smaller mass than the other two bodies ($m_3 << m_1, m_2$), and thus, it does not influence the motion of P_1 or P_2.

3. The primary bodies, P_1 and P_2 ($m_1 \geq m_2$), move in closed circular Keplerian orbits about their common barycenter. This Keplerian motion is assumed to be circular for this formulation.

2.2.2 Equations of Motion

According to the statement of the CR3BP, a spacecraft of negligible mass, m_3, moves under the gravitational attraction of two primary bodies, shown in Figure 2.2, where both are assumed to be spherically homogeneous and affecting the spacecraft by the following gravitational force:

$$\mathbf{F} = -\frac{Gm_1m_3}{R_{13}^3}\mathbf{R}_{13} - \frac{Gm_2m_3}{R_{23}^3}\mathbf{R}_{23} \tag{2.6}$$

where $G = 6.67259 \times 10^{-20}$ $[km^3/kg/sec^2]$ is the gravitational constant, $\mathbf{R}_{13}$ and $\mathbf{R}_{23}$ are the position vectors of the s/c with respect to the first and the second primaries, respectively, while R_{13} and R_{23} are their corresponding magnitudes. Meanwhile, $\mathbf{F}$, the gravitation force, can also be expressed using Newton's second law as:

$$\mathbf{F} = m_3(\ddot{\mathbf{R}}_3)_I \tag{2.7}$$

where $(\ddot{\mathbf{R}}_3)_I$ is the inertial acceleration of the s/c. From Equations (2.6) and (2.7), the inertial acceleration of the s/c is found as:

$$(\ddot{\mathbf{R}}_3)_I = -\frac{Gm_1}{R_{13}^3}\mathbf{R}_{13} - \frac{Gm_2}{R_{23}^3}\mathbf{R}_{23} \tag{2.8}$$

Since numerical methods are employed instead of the unavailable closed-from analytical solution, parameters non-dimensionalization is performed for both generalization and computational purposes. Some useful characteristic quantities for distance, mass, and time are introduced starting with the characteristic length, l^*, which is defined as the distance between the two primaries as:

$$l^* = R_1 + R_2 \tag{2.9}$$

where R_1 and R_2 are the corresponding magnitudes of the position vectors $\mathbf{R}_1$ and $\mathbf{R}_2$, respectively, as as shown in Figure 2.2. Note that l^* also represents the semi-major axis of the orbit of the second primary with respect

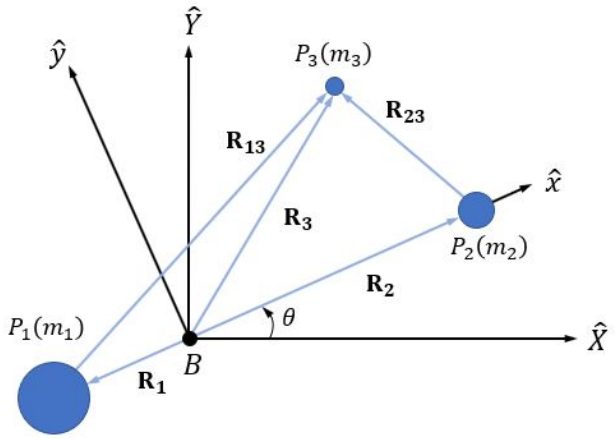

Figure 2.2: Geometry of the three-body system viewed in the inertial and the rotating Frames.

to the first primary. Similarly, the characteristic mass, m^* is defined as the sum of the masses of the primaries as:

$$m^* = m_1 + m_2 \tag{2.10}$$

Meanwhile, the characteristic time, t^*, is defined as the inverse of the dimensional angular velocity, N, which is expressed in terms of Kepler's Third Law as:

$$t^* = \frac{1}{N} = \frac{T}{2\pi} = \sqrt{\frac{l^{*3}}{Gm^*}} \tag{2.11}$$

where T is the orbital period of the second primary with respect to the first primary. Note that t^* was chosen such that the non-dimensional angular velocity of the rotating frame, n, is normalized to one as:

$$n = Nt^* = 1 \tag{2.12}$$

while the non-dimensional time, τ, is expressed as:

$$\tau = \frac{t}{t^*} \tag{2.13}$$

Other useful non-dimensional parameters are also defined as:

$$\mu = \frac{m_2}{m^*} = \frac{R_1}{l^*} \tag{2.14}$$

$$1 - \mu = \frac{m_1}{m^*} = \frac{R_2}{l^*} \tag{2.15}$$

where μ represents the non-dimensional distance and also called the mass ratio. By substituting for the Earth-Moon system, the characteristic quantities are computed as listed in Table 2.1. Deriving the non-dimensional form

Table 2.1: Characteristic parameters of the CR3BP.

Parameter	Value
μ	1.215059×10^{-2}
m^* $[kg]$	6.045860×10^{24}
l^* $[km]$	3.844000×10^{5}
t^* $[sec]$	3.751858×10^{5}

of the equation of motion in Equation (2.8) is performed by first deriving the non-dimensional position vectors as:

$$\mathbf{r}_3 = \frac{\mathbf{R}_3}{l^*} = x\hat{x} + y\hat{y} + z\hat{z} \tag{2.16}$$

$$\mathbf{r}_{13} = \frac{\mathbf{R}_{13}}{l^*} = (x+\mu)\hat{x} + y\hat{y} + z\hat{z} \tag{2.17}$$

$$\mathbf{r}_{23} = \frac{\mathbf{R}_{23}}{l^*} = (x-1+\mu)\hat{x} + y\hat{y} + z\hat{z} \tag{2.18}$$

Applying Equations (2.9) through (2.18) into Equation (2.8), the non-dimensional inertial acceleration is obtained as:

$$(\ddot{\mathbf{r}}_3)_I = -\frac{1-\mu}{r_{13}^3}\mathbf{r}_{13} - \frac{\mu}{r_{23}^3}\mathbf{r}_{23} \tag{2.19}$$

where $(\ddot{\mathbf{r}}_3)_I$ is the non-dimensional acceleration vector of P_3 relative to an inertial observer and expressed in terms of rotating frame coordinates. For expressing the equation of motion in Equation (2.19) in the rotating frame, the transport theorem is applied to find the velocity in the inertial frame in terms of the rotating frame as:

$$(\dot{\mathbf{r}}_3)_I = \dot{\mathbf{r}}_3 + \boldsymbol{\omega}_{R/I} \times \mathbf{r}_3 \tag{2.20}$$

where $\boldsymbol{\omega}_{R/I}$ is the angular velocity vector of the rotating frame with respect to the inertial frame, henceforward referred to as $\boldsymbol{\omega}$, and is given as:

$$\boldsymbol{\omega} = n\hat{z} \tag{2.21}$$

Applying the transport theorem for Equation (2.20), the inertial acceleration is found as:

$$(\ddot{\mathbf{r}}_3)_I = \ddot{\mathbf{r}}_3 + \dot{\boldsymbol{\omega}} \times \mathbf{r}_3 + \boldsymbol{\omega} \times (\boldsymbol{\omega} \times \mathbf{r}_3) + 2\boldsymbol{\omega} \times \dot{\mathbf{r}}_3 \tag{2.22}$$

Substituting Equation (2.21) in Equations (2.20) and (2.22), and taking into account that $\dot{\boldsymbol{\omega}} = 0$ for the CR3BP, the inertial velocity and acceleration of in CR3BP are found as:

$$(\dot{\mathbf{r}}_3)_I = \begin{bmatrix} \dot{x} - y \\ \dot{y} + x \\ \dot{z} \end{bmatrix} \tag{2.23}$$

$$(\ddot{\mathbf{r}}_3)_I = \begin{bmatrix} \ddot{x} - x - 2\dot{y} \\ \ddot{y} - y + 2\dot{x} \\ \ddot{z} \end{bmatrix} \tag{2.24}$$

Substituting Equation (2.24) in Equation (2.19), the Equation of motion of the CR3BP in the rotating frame is obtained as:

$$\ddot{\mathbf{r}}_3 = -\Big(\frac{1-\mu}{r_{13}^3}\mathbf{r}_{13} + \frac{\mu}{r_{23}^3}\mathbf{r}_{23}\Big) - \boldsymbol{\omega} \times (\boldsymbol{\omega} \times \mathbf{r}_3) - 2\boldsymbol{\omega} \times \dot{\mathbf{r}}_3 \tag{2.25}$$

Where the three terms refer to the gravitational, centrifugal, and Coriolis accelerations, respectively. Projecting Equation (2.25) along the three axes, the non-linear equations of motion of the CR3BP written in the rotating frame are obtained as:

$$\begin{aligned} \ddot{x} &= -\frac{1-\mu}{r_{13}^3}(x+\mu) - \frac{\mu}{r_{23}^3}\big(x - (1-\mu)\big) + x + 2\dot{y} \\ \ddot{y} &= -\frac{1-\mu}{r_{13}^3}y - \frac{\mu}{r_{23}^3}y + y - 2\dot{x} \\ \ddot{z} &= -\frac{1-\mu}{r_{13}^3}z - \frac{\mu}{r_{23}^3}z \end{aligned} \tag{2.26}$$

where these equations are autonomous and their solution is time-invariant. Introducing the pseudo-potential function, U_C, which refers to the balance between the gravitational and centrifugal accelerations, given as:

$$U_C = \frac{1-\mu}{r_{13}} + \frac{\mu}{r_{23}} + \frac{1}{2}(x^2 + y^2) \tag{2.27}$$

the equations of motion in Equation (2.26) are rewritten as:

$$\begin{aligned} \ddot{x} - 2\dot{y} &= \frac{\partial U_C}{\partial x} \\ \ddot{y} + 2\dot{x} &= \frac{\partial U_C}{\partial y} \\ \ddot{z} &= \frac{\partial U_C}{\partial z} \end{aligned} \tag{2.28}$$

Note that for solving these equations analytically in the rotating frame, six integrals of motions are required. However, since only one integral of motion exists, numerical integration is required instead.

2.2.3 Integrals of the Motion

In contrast to the Keplerian two-body problem, the differential equations in the CR3BP do not yield sufficient constants of the motion to produce an analytical closed-form solution. However, one useful constant of the motion does emerge in the CR3BP rotating-frame formulation.

Jacobi Constant

One energy-like constant of the motion does exist in the rotating-frame formulation of the CR3BP. This scalar, called the Jacobi constant, J_C, provides significant insight into the dynamical behavior in the CR3BP and aids the process of numerical integration. Deriving an expression for the Jacobi constant, the vector gradient of the pseudo-potential function is found as:

$$\nabla U_C = -\Big(\frac{1-\mu}{r_{13}^3}\mathbf{r}_{13} + \frac{\mu}{r_{23}^3}\mathbf{r}_{23}\Big) - \boldsymbol{\omega} \times (\boldsymbol{\omega} \times \mathbf{r}_3) \tag{2.29}$$

Taking the dot product of Equation (2.27) with $\dot{\mathbf{r}}_3$, the Jacobi constant is found as:

$$J_C = 2U_C - \dot{r}_3^2 \tag{2.30}$$

Note that in the rotating frame formulation of the CR3BP, the Jacobi constant is the only integral of the motion.

Lagrangian Points

Given the CR3BP, it can be shown that there are five positions in space, the Lagrangian (libration) points, at which a s/c maintains its position relative to the two primaries. These points represent time-invariant equilibrium solutions to the autonomous equations of motion, at which the gravitational and centrifugal forces are in balance, and they are found by setting Equation (2.29) to zero as:

$$\nabla U_C = 0 \tag{2.31}$$

which is equivalent to setting to zero all the velocities and accelerations as:

$$\begin{aligned}
0 &= -\frac{1-\mu}{r_{13_{eq}}^3}(x_{eq}+\mu) - \frac{\mu}{r_{23_{eq}}^3}\big(x_{eq}-(1-\mu)\big) + x_{eq} \\
0 &= -\frac{1-\mu}{r_{13_{eq}}^3}y_{eq} - \frac{\mu}{r_{23_{eq}}^3}y_{eq} + y_{eq} \\
0 &= -\frac{1-\mu}{r_{13_{eq}}^3}z_{eq} - \frac{\mu}{r_{23_{eq}}^3}z_{eq}
\end{aligned} \tag{2.32}$$

where the subscript eq indicates equilibrium positions as identified in the rotating reference frame. Solving Equations (2.32), the five equilibrium Lagrangian points, found by Lagrange in 1772, are obtained as shown in Figure 2.3 where all points are found to have a zero out-of-plane component, that is $z_{eq} = 0$.

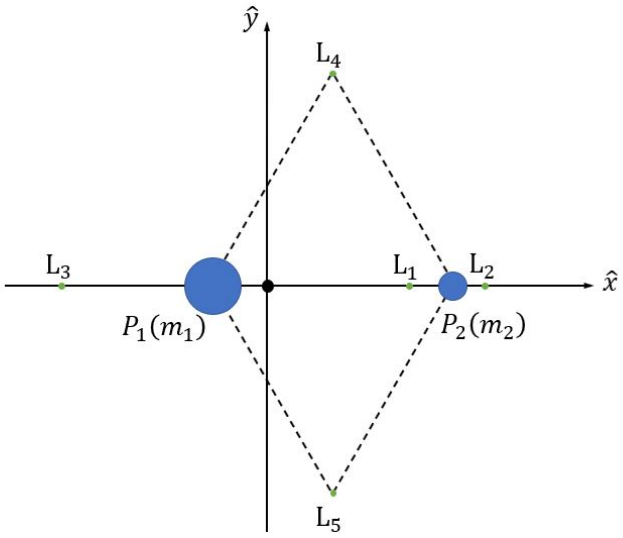

Figure 2.3: Libration points viewed in the rotating frame.

The equilibrium points, L_i, are numbered in the order of decreasing value of Jacobi constant; such a numbering is consistent with the order at which they become accessible with increasing orbital energy. Note that L_4 and L_5 become accessible at the same value of Jacobi constant but, by convention, L_4 reflects the equilateral point that leads along the $\hat{y}$-axis while L_5 lies on the opposite side. Meanwhile, the locations of the libration points and their corresponding Jacobi constants for the Earth-Moon system are listed in Table 2.2.

Table 2.2: Libration points location of the Earth-Moon system in the rotating frame.

Libration Point	Coordinates	J_C
$L_1(x, y, z)$	$(0.836915, 0, 0)$	3.18834
$L_2(x, y, z)$	$(1.155682, 0, 0)$	3.17216
$L_3(x, y, z)$	$(-1.005063, 0, 0)$	3.01215
$L_4(x, y, z)$	$(0.487849, 0.866025, 0)$	2.98799
$L_5(x, y, z)$	$(0.487849, -0.866025, 0)$	2.98799

Zero Velocity Curves

The existence of the Jacobi constant allows the definition of the Zero-Velocity Curves (ZVC), or Hill surfaces, which defines regions in which the s/c is allowed to move in space. They have the advantage of giving a qualitative picture of the motion of the s/c under the influence of the two primaries. The ZVC are obtained from the intersection of the energy of the s/c at $\dot{\mathbf{r}}_3 = 0$, which is represented by J_C, with the potential energy, U_C. In turn, since U_C is a function of x, y, and z, every value of J_C corresponds to different ZVC, as shown in Figure 2.4

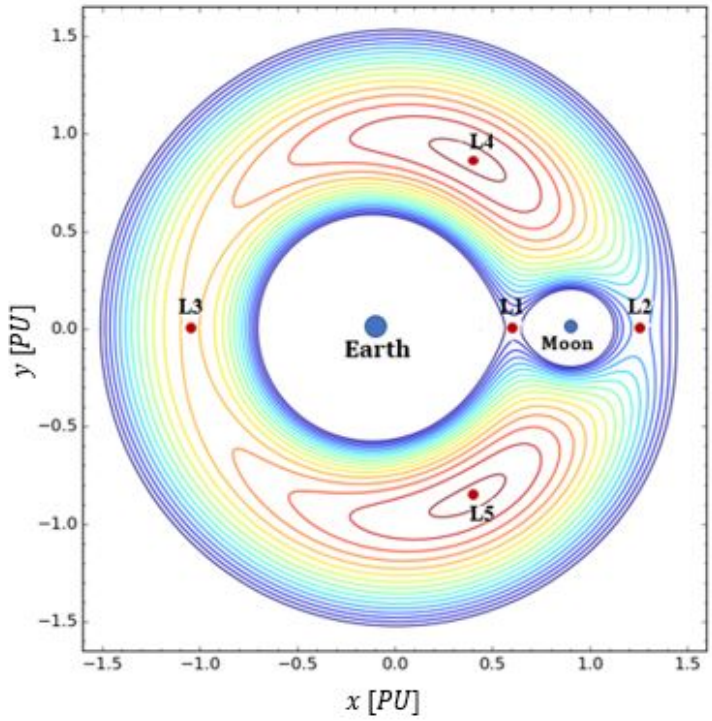

Figure 2.4: Contour line of the three-body potential function in the rotating frame, where the Position Unit [PU] is the characteristic length, l^*.

2.3 Elliptical Restricted Three-Body Problem

In the previous section, the equations of motion were formulated in the CR3BP using a uniformly rotating coordinate system in which the primaries are fixed and the Jacobi constant does not depend explicitly on time. However, since the CR3BP does not consider the eccentricity of the secondary around the primary, a more general model is needed. The inclusion of

the eccentricity into the equations of motion defines a more general model, known as the elliptic restricted three-body problem (ER3BP). Formulating the equations of motion in ER3BP requires the definition of the rotating-pulsating coordinates [5], in which the primaries are kept at fixed locations. Meanwhile, the Jacobi constant becomes explicitly a function of the independent variable, which is the true anomaly. This pulsating, or oscillating, coordinate system is first introduced by defining the variable distance between the primaries, r_{E-M}, which is found using the analysis of the two-body Keplerian motion [92] of the orbit of the Moon around the Earth as:

$$r_{E-M} = \frac{a(1-e^2)}{1+e\cos\theta} \tag{2.33}$$

where a is the semi-major axis, $e = 0.0549$ is the eccentricity, and θ is the true anomaly. Accordingly, the dimensional angular velocity is given as:

$$N = \frac{d\theta}{dt} = \frac{h}{r_{E-M}^2} = \frac{\sqrt{Gm^*a(1-e^2)}}{r_{E-M}^2} = \frac{\sqrt{Gm^*}(1+e\cos\theta)^2}{a^{\frac{3}{2}}(1-e^2)^{\frac{3}{2}}} \tag{2.34}$$

where h is the angular momentum of the Keplerian orbit. Meanwhile, the characteristic length is redefined as:

$$l^* = a \tag{2.35}$$

It should be noted that Equation (2.35) is similar to Equation (2.9) such that l^* is also equal to the distance between the primaries. However, in the case of the CR3BP, the geocentric lunar radius with respect to the Earth was considered, while in the case of the ER3BP, the heliocentric lunar semi-major axis was taken. The new values of the characteristic quantitis are listed in Table 2.3.

Table 2.3: Characteristic parameters of the ER3BP.

Parameter	Value
l^* $[km]$	3.838000×10^5
t^* $[sec]$	3.743077×10^5

Following the same analogy taken in the CR3BP, the non-dimensional equations of motion are obtained in the rotating coordinates in terms of the time as the independent variable. Next, the transformation of the equations of motion from the rotating coordinates to the rotating-pulsating coordinates, while still in the rotating frame of reference, requires several considerations:

1. The rotating and rotating-pulsating coordinates are related as:

$$s_{Rotating} = \rho s_{Rotating-Pulsating} \tag{2.36}$$

where s represents the coordinates, x, y, and z, while ρ is the non-dimensional variable distance:

$$\rho = \frac{r_{E-M}}{l^*} = \frac{(1-e^2)}{1+e\cos\theta} \tag{2.37}$$

2. The equations are rewritten in terms of the new independent variable, the true anomaly, which is introduced by the following equation:

$$\frac{d}{d\tau} = \frac{d\theta}{d\tau}\frac{d}{d\theta} \tag{2.38}$$

where the non-dimensional angular velocity:

$$n = \frac{d\theta}{d\tau} = Nt^* = \frac{(1+e\cos\theta)^2}{(1-e^2)^{\frac{3}{2}}} \tag{2.39}$$

Applying Equations (2.36) and (2.39) to Equation (2.28), the equations of motion are rewritten as [41]:

$$\begin{aligned} \ddot{x} - 2\dot{y} &= \frac{1}{1+e\cos\theta}\Big(\frac{\partial U_E}{\partial x}\Big) \\ \ddot{y} + 2\dot{x} &= \frac{1}{1+e\cos\theta}\Big(\frac{\partial U_E}{\partial y}\Big) \\ \ddot{z} &= \frac{1}{1+e\cos\theta}\Big(\frac{\partial U_E}{\partial z}\Big) \end{aligned} \tag{2.40}$$

where the dots are now denoting to the derivation in terms of the true anomaly as the independent variable instead of the time. These non-linear equations are known as the equations of motion of the ER3BP, written in the rotating frame and expressed using rotating-pulsating coordinates. Meanwhile, the pseudo-potential function of the ER3BP, U_E, is given as:

$$U_E = \frac{1-\mu}{r_{13}} + \frac{\mu}{r_{23}} + \frac{1}{2}(x^2 + y^2 - z^2 e\cos\theta) \tag{2.41}$$

Note that in case of a circular orbit, $e = 0$, it is obtained from Equations (2.37) and (2.39) that $\rho = n = 1$, and by looking also at Equation (2.36), it is found that the rotating and rotating-pulsating coordinates are equal. Moreover, the independent variable, θ, becomes equivalent to τ, such that $\frac{d}{d\tau} = \frac{d}{d\theta}$ as shown from Equation (2.38). Therefore, the CR3BP can be considered as a special case of the ER3BP when the eccentricity is zero, and for this reason, the same nomenclature used in the CR3BP was adopted also for the ER3BP.

2.4 Environmental Disturbances

A Spacecraft in the Earth-Moon system is generally subjected to several disturbance forces and torques, their magnitude and direction depend on different physical parameters, such as the shape, material, mass, and environmental conditions. There are two main sources of disturbances to be considered; solar radiation pressure (SRP) and the gravitational effect of other planets, known as the forth-body effect. Unlike the SRP effect, the forth-body effect of all planets can be blended into the dynamical model by using the N-body full ephemeris model, which can be reviewed in detail in [22]. Meanwhile, following the aim of this work of developing a robust and efficient control system, the ER3BP, supported by the SRP disturbance, is considered a sufficient environment for assessing the functionality and performance of the proposed control approach.

2.4.1 Solar Radiation Pressure

The SRP disturbance is generated through the impact of the solar radiation on the surfaces of the s/c facing the Sun. Its magnitude depends on the spacecraft's mass, size, surface material properties, and distance from the Sun, and is calculated similar to [93] as:

$$\overline{\mathbf{a}}_{SRP} = -\sum_{i=0}^{n} \frac{PA_i}{m}(\hat{\mathbf{s}}.\hat{\mathbf{n}}_i)\Big[(1-\rho_s)\hat{\mathbf{s}} + \big(2\rho_s(\hat{\mathbf{s}}.\hat{\mathbf{n}}_i) + \frac{2}{3}\rho_d\big)\hat{\mathbf{n}}_i\Big] \tag{2.42}$$

where $\overline{\mathbf{a}}_{SRP}$ is the dimensional acceleration, $P = 4.52e{-}6\ [Pa]$ is the nominal SRP constant at 1 astronomical units from the sun, m is the spacecraft mass, $\hat{\mathbf{s}}$ is the spacecraft-Sun unit vector, A_i and $\hat{\mathbf{n}}_i$ are the area and normal to the surface unit vector of surface i, respectively, n is the total number of surfaces, and ρ_s and ρ_d are the specular and diffuse reflection coefficient of the surfaces, respectively. Equation (2.42) is then rewritten for the maximum acceleration case as:

$$\mathbf{a}_{SRP} = -\frac{PA_{max}}{m}\big(1+\rho_s+\frac{2}{3}\rho_d\big)\hat{\mathbf{s}} \times \left(\frac{(t^*)2}{l^*\rho}\right) \tag{2.43}$$

where $\mathbf{a}_{SRP}$ represents the non-dimensional acceleration, A_{max} denotes the maximum possible cross-section area of the spacecraft when completely normal to the incident radiation, and $\big((t^*)2/(l^*\rho)\big)$ is the acceleration non-dimensionalization ratio. Meanwhile, the spacecraft-Sun unit vector, $\hat{\mathbf{s}}$, is calculated using NASA's JPL-DE430 ephemeris, check its MATLAB extension in [94], at a certain epoch. Adding the SRP disturbances, Equation

(2.40) is augmented as:

$$\begin{aligned}
\ddot{x} - 2\dot{y} &= \frac{1}{1+e\cos\theta}\left(\frac{\partial U_E}{\partial x}\right) + \mathbf{a}_{SRP}(1) \\
\ddot{y} + 2\dot{x} &= \frac{1}{1+e\cos\theta}\left(\frac{\partial U_E}{\partial y}\right) + \mathbf{a}_{SRP}(2) \\
\ddot{z} &= \frac{1}{1+e\cos\theta}\left(\frac{\partial U_E}{\partial z}\right) + \mathbf{a}_{SRP}(3)
\end{aligned} \tag{2.44}$$

In this investigation, the LUMIO mission 12U CubeSate model [95, 96] was adopted with the main parameters of interest summarized in Table 2.4. Next and choosing the starting epoch time on January 1, 2030, Equation

Table 2.4: Spacecraft parameters.

Parameter	Value
$m\ [kg]$	22.82
$A_{max}\ [m^2]$	0.3
ρ_s	0.6
ρ_d	0.1

(2.43) is computed over a time span of one year as shown in Figure 2.5. It should be noted that the shadowing effect of the Earth (when the Earth blocks the radiation coming from the Sun) was not included following the aim of considering the maximum SRP effect.

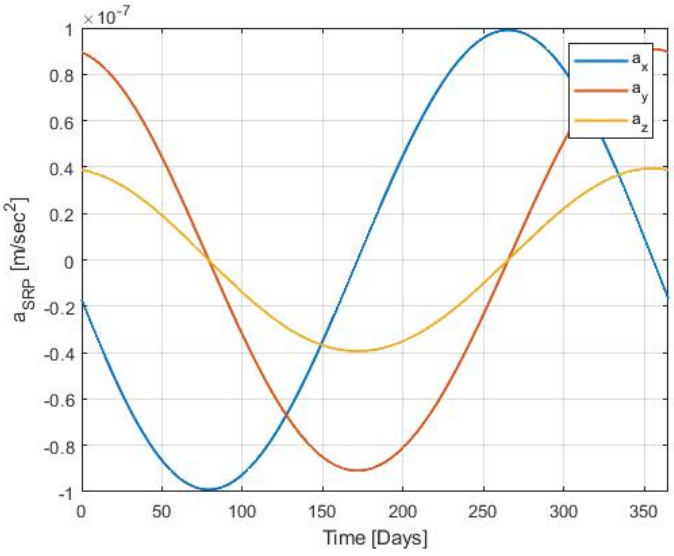

Figure 2.5: Acceleration disturbance due to SRP starting from January 1, 2030.

2.5 Propulsion System

In this section, the propulsion system used to achieve the station-keeping maneuvers is presented in detail considering the LUMIO mission. Following the initial design proposed for the LUMIO mission [97], the propulsion system is based on a partially customized version of the VACCO Hybrid ADN MiPS, including one main mono-propellant thruster (ADN green propellant) providing a thrust of 0.1 $[N]$ for the main maneuvers. This thrust force is then translated into an acceleration given by the equation:

$$a_T = \frac{F_T}{m} \times \left(\frac{(t^*)2}{l^* \rho} \right) \tag{2.45}$$

where a_T is the non-dimensional nominal scalar thrust acceleration, F_T is the thrust force (considered constant during the simulation), m is the mass of spacecraft, and $\big((t^*)2/(l^*\rho)\big)$ is the acceleration non-dimensionalization ratio. For an increased accuracy, the mass of the spacecraft was considered as a variable whose dynamics is given as:

$$\frac{dm}{dt} = -\frac{F_T}{I_s g_0} \tag{2.46}$$

where $g_0 = 9.81\ [m/sec^2]$ is the standard sea level acceleration of gravity and I_s is the specific impulse of the thruster. After the maneuver calculation, which is going to be discussed in detail in Chapter 4, the spacecraft is then to be reoriented to align the thruster with the required maneuver direction. The thrust acceleration vector is then obtain as:

$$\mathbf{a}_{Thruster} = a_T \frac{\Delta \mathbf{v}}{|\Delta \mathbf{v}|} \tag{2.47}$$

where $\Delta \mathbf{v}$ is the calculated maneuver. Note that since a discrete control approach is sought in this investigation, the operation time of the thruster is determined as:

$$t_{ON} = \frac{|\Delta \mathbf{v}|}{a_T} \tag{2.48}$$

Augmenting Equation (2.44) with Equation (2.47), the overall equations of motion are now expressed as:

$$\begin{aligned}
\ddot{x} - 2\dot{y} &= \frac{1}{1 + e\cos\theta}\left(\frac{\partial U_E}{\partial x}\right) + \mathbf{a}_{SRP}(1) + \mathbf{a}_{Thruster}(1) \\
\ddot{y} + 2\dot{x} &= \frac{1}{1 + e\cos\theta}\left(\frac{\partial U_E}{\partial y}\right) + \mathbf{a}_{SRP}(2) + \mathbf{a}_{Thruster}(2) \\
\ddot{z} &= \frac{1}{1 + e\cos\theta}\left(\frac{\partial U_E}{\partial z}\right) + \mathbf{a}_{SRP}(3) + \mathbf{a}_{Thruster}(3)
\end{aligned} \tag{2.49}$$

In this investigation, the Bradford ECAPS 0.1N High Performance Green Propulsion (HPGP) thruster [98] was selected, with the main parameters listed in Table 2.5. It should be noted that this type of thrusters is flight proven as it has successfully flown aboard the PRISMA satellites [99].

Table 2.5: Bradford ECAPS 0.1N HPGP parameters.

Parameter	Value
Thrust Range $[mN]$	$30 - 100$
Propellant	LMP-103S
Specific Impulse $[sec]$	$196 - 209$
Total Impulse $[N - sec]$	3320
Minimum Impulse Bit $[mN - sec]$	< 5
Longest Continuous Firing $[min]$	30

.

This page was intentionally left blank

Chapter 3

Differential Correction

As the governing equations of motion in both the CR3BP and the ER3BP do not acquire closed-form analytical solutions, numerical strategies were adopted to propagate trajectories in these models. Moreover, since arbitrary sets of initial conditions rarely yield the desired behavior, differential correction strategies are required to meet design requirements. In this chapter, correction strategies based on single and multi-segment shooting methods are employed for computing periodic halo orbits in the CR3BP. Orbit continuation is also introduced to shift the initial solutions to the ER3BP using the eccentricity of the moon's orbit as a continuation parameter. The calculation of periodic elliptic halo orbits is finally presented using continuation and nonlinear programming optimization methods.

3.1 State Transition Matrix

Correction strategies are based on an assessment of the sensitivities. Thus, to implement various shooting methods, a scheme to relate variations or perturbations in the initial state, $\mathbf{x}(t_0)$, to variations in a downstream state, $\mathbf{x}(t, \mathbf{x}(t_0))$, must be derived. For this purpose, the equations of motion can be rewritten in first order form as:

$$\dot{\mathbf{x}}(t) = \mathbf{f}(t, \mathbf{x}(t), \boldsymbol{\kappa}) \tag{3.1}$$

where the state vector, $\mathbf{x}(t)$ is defined as:

$$\mathbf{x}(t) = \begin{bmatrix} x(t) & y(t) & z(t) & \dot{x}(t) & \dot{y}(t) & \dot{z}(t) \end{bmatrix}^T \tag{3.2}$$

while $\boldsymbol{\kappa}$ is a vector of additional variables or parameters. Considering a reference nominal path point, $\mathbf{x}_n(t)$, the vector variation relative to that

point is defined as:

$$\delta\mathbf{x}(t) = \mathbf{x}(t) - \mathbf{x}_n(t) \tag{3.3}$$

where $\mathbf{x}(t)$ identifies a state of a nearby trajectory at time t. Using a first-order Taylor series expansion relative to the nominal path, the linear variational equations, derived from the equations of motion, are written as:

$$\delta\dot{\mathbf{x}}(t) = \mathbf{A}(t)\delta\mathbf{x}(t) \tag{3.4}$$

where the matrix $\mathbf{A}(t)$ is the Jacobian matrix consisted of the partials of the equations of motion and is given as:

$$\mathbf{A}(t) = \frac{\partial\mathbf{f}(t, \mathbf{x}(t), \boldsymbol{\kappa})}{\partial\mathbf{x}(t)} \tag{3.5}$$

Equation (3.4) is then written in the form of the matrix derivative that relates variations in the initial state to variations in the downstream state as:

$$\delta\mathbf{x}(t) = \frac{\partial\mathbf{x}(t)}{\partial\mathbf{x}(t_0)}\delta\mathbf{x}(t_0) \tag{3.6}$$

Finding the matrix $\frac{\partial\mathbf{x}(t)}{\partial\mathbf{x}(t_0)}$ is then performed by deriving its first-order differential equation as:

$$\frac{d}{dt}\Big(\frac{\partial\mathbf{x}(t)}{\partial\mathbf{x}(t_0)}\Big) = \frac{d}{d\mathbf{x}(t_0)}\frac{\partial\mathbf{x}(t)}{\partial t} = \frac{d}{d\mathbf{x}(t_0)}\dot{\mathbf{x}}(t) \tag{3.7}$$

Rearranging, since $\mathbf{x}(t_0)$ and t are independent, and applying the chain rule, Equation (3.7) is written as:

$$\frac{d}{dt}\Big(\frac{\partial\mathbf{x}(t)}{\partial\mathbf{x}(t_0)}\Big) = \frac{d}{d\mathbf{x}(t_0)}\dot{\mathbf{x}}(t) = \frac{\partial\mathbf{f}(t, \mathbf{x}(t), \boldsymbol{\kappa})}{\partial\mathbf{x}(t)}\frac{\partial\mathbf{x}(t)}{\partial\mathbf{x}(t_0)} = \mathbf{A}(t)\frac{\partial\mathbf{x}(t)}{\partial\mathbf{x}(t_0)} \tag{3.8}$$

It is now possible to define the state transition matrix (STM) as:

$$\boldsymbol{\Phi}(t, t_0) = \frac{\partial\mathbf{x}(t)}{\partial\mathbf{x}(t_0)} \tag{3.9}$$

Substituting Equation (3.9) in Equation (3.8), the first-order matrix differential equation governing the evolution of the STM, also called first variational equation [100], is reduced to:

$$\dot{\boldsymbol{\Phi}}(t, t_0) = \mathbf{A}(t)\boldsymbol{\Phi}(t, t_0) \tag{3.10}$$

with the initial conditions given as $\boldsymbol{\Phi}(t_0, t_0) = \mathbf{I}_{6\times6}$. Note that Equation (3.10) is propagated along the equations of motion, which is required for updating the elements the matrix $\mathbf{A}(t)$ simultaneously.

3.1.1 STM for the CR3BP

The governing equations for the STM in the CR3BP in Equation (3.10) are numerically integrated along with the equations of motion governing the states. The equations for the individual elements of STM are derived from the linear variational equations relative to a reference arc in the CR3BP, where any path or arc in the CR3BP is a nonlinear solution to Equation (2.28). Therefore, the differential equations governing the variations, derived from the equations of motion of the CR3BP, are given as:

$$\begin{aligned}
\delta\ddot{x} - 2\delta\dot{y} &= \frac{\partial^2 U_C}{\partial x \partial x}\delta x + \frac{\partial^2 U_C}{\partial x \partial y}\delta y + \frac{\partial^2 U_C}{\partial x \partial z}\delta z \\
\delta\ddot{y} + 2\delta\dot{x} &= \frac{\partial^2 U_C}{\partial y \partial x}\delta x + \frac{\partial^2 U_C}{\partial y \partial y}\delta y + \frac{\partial^2 U_C}{\partial y \partial z}\delta z \\
\delta\ddot{z} &= \frac{\partial^2 U_C}{\partial z \partial x}\delta x + \frac{\partial^2 U_C}{\partial z \partial y}\delta y + \frac{\partial^2 U_C}{\partial z \partial z}\delta z
\end{aligned} \tag{3.11}$$

Substituting Equation (3.11) into Equation (3.4), the matrix $\mathbf{A}(t)$ is obtained as:

$$\mathbf{A}(t) = \begin{bmatrix} \mathbf{0}_{3\times 3} & \mathbf{I}_{3\times 3} \\ \mathbf{U_C}_{dd} & 2\boldsymbol{\Omega} \end{bmatrix} \tag{3.12}$$

where $\mathbf{0}_{3\times 3}$ and $\mathbf{I}_{3\times 3}$ are (3×3) zero and identity matrices, respectively, and $\boldsymbol{\Omega}$ represents the Coriolis acceleration contribution:

$$\boldsymbol{\Omega} = \begin{bmatrix} 0 & 1 & 0 \\ -1 & 0 & 0 \\ 0 & 0 & 0 \end{bmatrix} \tag{3.13}$$

while $\mathbf{U_C}_{dd}$ is the symmetric matrix of second partial derivatives of the potential energy function:

$$\mathbf{U_C}_{dd} = \begin{bmatrix} \frac{\partial^2 U_C}{\partial x \partial x} & \frac{\partial^2 U_C}{\partial x \partial y} & \frac{\partial^2 U_C}{\partial x \partial z} \\ \frac{\partial^2 U_C}{\partial y \partial x} & \frac{\partial^2 U_C}{\partial y \partial y} & \frac{\partial^2 U_C}{\partial y \partial z} \\ \frac{\partial^2 U_C}{\partial z \partial x} & \frac{\partial^2 U_C}{\partial z \partial y} & \frac{\partial^2 U_C}{\partial z \partial z} \end{bmatrix} \tag{3.14}$$

where

$$\frac{\partial^2 U_C}{\partial x \partial x} = 1 - \frac{1-\mu}{r_{13}^3} - \frac{\mu}{r_{23}^3} + \frac{3(1-\mu)(x+\mu)^2}{r_{13}^5} + \frac{3\mu(x-1+\mu)^2}{r_{23}^5}$$

$$\frac{\partial^2 U_C}{\partial y \partial y} = 1 - \frac{1-\mu}{r_{13}^3} - \frac{\mu}{r_{23}^3} + \frac{3(1-\mu)y^2}{r_{13}^5} + \frac{3\mu y^2}{r_{23}^5}$$

$$\frac{\partial^2 U_C}{\partial z \partial z} = -\frac{1-\mu}{r_{13}^3} - \frac{\mu}{r_{23}^3} + \frac{3(1-\mu)z^2}{r_{13}^5} + \frac{3\mu z^2}{r_{23}^5}$$

$$\frac{\partial^2 U_C}{\partial x \partial y} = \frac{\partial^2 U_C}{\partial y \partial x} = \frac{3(1-\mu)(x+\mu)y}{r_{13}^5} + \frac{3\mu(x-1+\mu)y}{r_{23}^5}$$
$$\frac{\partial^2 U_C}{\partial x \partial z} = \frac{\partial^2 U_C}{\partial z \partial x} = \frac{3(1-\mu)(x+\mu)z}{r_{13}^5} + \frac{3\mu(x-1+\mu)z}{r_{23}^5}$$
$$\frac{\partial^2 U_C}{\partial y \partial z} = \frac{\partial^2 U_C}{\partial z \partial y} = \frac{3(1-\mu)yz}{r_{13}^5} + \frac{3\mu yz}{r_{23}^5}$$

where x, y, and z are obtained from the integration of the equations of motion, and then used in obtaining an updated $\mathbf{A}(t)$, which is employed in the integration of Equation (3.10), yielding the STM of the CR3BP.

3.1.2 STM for the ER3BP

The definition of the STM in the ER3BP follows a similar discussion as in the CR3BP. Therefore, the differential equations governing the variations, derived from the equations of motion of the ER3BP, are given as:

$$\begin{aligned}
\delta\ddot{x} - 2\delta\dot{y} &= \frac{1}{1+e\cos\theta}\Big(\frac{\partial^2 U_E}{\partial x \partial x}\delta x + \frac{\partial^2 U_E}{\partial x \partial y}\delta y + \frac{\partial^2 U_E}{\partial x \partial z}\delta z\Big) \\
\delta\ddot{y} + 2\delta\dot{x} &= \frac{1}{1+e\cos\theta}\Big(\frac{\partial^2 U_E}{\partial y \partial x}\delta x + \frac{\partial^2 U_E}{\partial y \partial y}\delta y + \frac{\partial^2 U_E}{\partial y \partial z}\delta z\Big) \\
\delta\ddot{z} &= \frac{1}{1+e\cos\theta}\Big(\frac{\partial^2 U_E}{\partial z \partial x}\delta x + \frac{\partial^2 U_E}{\partial z \partial y}\delta y + \frac{\partial^2 U_E}{\partial z \partial z}\delta z\Big)
\end{aligned} \tag{3.15}$$

Substituting Equation (3.15) into Equation (3.4), the matrix $\mathbf{A}(t)$ is obtained as:

$$\mathbf{A}(t) = \begin{bmatrix} \mathbf{0}_{3\times 3} & \mathbf{I}_{3\times 3} \\ \frac{1}{1+e\cos\theta}\mathbf{U}_{\mathbf{E}dd} & 2\boldsymbol{\Omega} \end{bmatrix} \tag{3.16}$$

where $\boldsymbol{\Omega}$ is defined in Equation (3.13) and $\mathbf{U}_{\mathbf{E}dd}$ is defined similar to Equation (3.14) as:

$$\mathbf{U}_{\mathbf{E}dd} = \begin{bmatrix} \frac{\partial^2 U_E}{\partial x \partial x} & \frac{\partial^2 U_E}{\partial x \partial y} & \frac{\partial^2 U_E}{\partial x \partial z} \\ \frac{\partial^2 U_E}{\partial y \partial x} & \frac{\partial^2 U_E}{\partial y \partial y} & \frac{\partial^2 U_E}{\partial y \partial z} \\ \frac{\partial^2 U_E}{\partial z \partial x} & \frac{\partial^2 U_E}{\partial z \partial y} & \frac{\partial^2 U_E}{\partial z \partial z} \end{bmatrix} \tag{3.17}$$

where

$$\frac{\partial^2 U_E}{\partial x \partial x} = 1 - \frac{1-\mu}{r_{13}^3} - \frac{\mu}{r_{23}^3} + \frac{3(1-\mu)(x+\mu)^2}{r_{13}^5} + \frac{3\mu(x-1+\mu)^2}{r_{23}^5}$$
$$\frac{\partial^2 U_E}{\partial y \partial y} = 1 - \frac{1-\mu}{r_{13}^3} - \frac{\mu}{r_{23}^3} + \frac{3(1-\mu)y^2}{r_{13}^5} + \frac{3\mu y^2}{r_{23}^5}$$
$$\frac{\partial^2 U_E}{\partial z \partial z} = -e\cos\theta - \frac{1-\mu}{r_{13}^3} - \frac{\mu}{r_{23}^3} + \frac{3(1-\mu)z^2}{r_{13}^5} + \frac{3\mu z^2}{r_{23}^5}$$

$$\frac{\partial^2 U_E}{\partial x \partial y} = \frac{\partial^2 U_E}{\partial y \partial x} = \frac{3(1-\mu)(x+\mu)y}{r_{13}^5} + \frac{3\mu(x-1+\mu)y}{r_{23}^5}$$
$$\frac{\partial^2 U_E}{\partial x \partial z} = \frac{\partial^2 U_E}{\partial z \partial x} = \frac{3(1-\mu)(x+\mu)z}{r_{13}^5} + \frac{3\mu(x-1+\mu)z}{r_{23}^5}$$
$$\frac{\partial^2 U_E}{\partial y \partial z} = \frac{\partial^2 U_E}{\partial z \partial y} = \frac{3(1-\mu)yz}{r_{13}^5} + \frac{3\mu yz}{r_{23}^5}$$

Meanwhile, the simultaneous integration of the equations of motion in Equation (2.40) and the first variational equation in Equation (3.10) yields the STM of the ER3BP.

3.2 Shooting Methods

Two-point boundary value problems are fundamental to differential corrections algorithms as core formulations to multi-body trajectory design. In this investigation, differential corrections formulated as shooting schemes are used to design the reference nominal orbit under some given constraints. The algorithm for the implementation of a shooting method allows for the manipulation of design variables to satisfy a given set of constraints. Particularly, the chosen implementation strategies employs a free variable and constraint method, where the free design variables vector is defined as:

$$\mathbf{X} = \begin{bmatrix} X_1 \\ X_2 \\ \vdots \\ X_n \end{bmatrix} \tag{3.18}$$

where the elements of $\mathbf{X}$ are the n design variables, which are allowed to be modified during the process. These design variable are then changed to satisfy a set of m scalar constraint equations given as:

$$\mathbf{F}(\mathbf{X}) = \begin{bmatrix} F_1(\mathbf{X}) \\ F_2(\mathbf{X}) \\ \vdots \\ F_m(\mathbf{X}) \end{bmatrix} = 0 \tag{3.19}$$

Having the constraints defined properly, an iterative process to determine a free variable vector, $\mathbf{X}^*$, such that $\mathbf{F}(\mathbf{X}^*) = 0$ is derived. Given an initial guess for the free variable vector, $\mathbf{X}_0$, and by expanding the constraint vector in a Taylor series about the initial guess, it is obtained:

$$\mathbf{F}(\mathbf{X}) = \mathbf{F}(\mathbf{X}_0) + \frac{\partial \mathbf{F}(\mathbf{X}_0)}{\partial \mathbf{X}_0}(\mathbf{X} - \mathbf{X}_0) + \dots \tag{3.20}$$

where $\frac{\partial \mathbf{F}(\mathbf{X}_0)}{\partial \mathbf{X}_0}$ is an $m \times n$ Jacobian matrix, which consists of the partial derivatives of the constraints with respect to the free variables, henceforward denoted $D\mathbf{F}(\mathbf{X}_0)$. Truncating the Taylor series in Equation (3.20) to first-order yields:

$$\mathbf{F}(\mathbf{X}) = \mathbf{F}(\mathbf{X}_0) + D\mathbf{F}(\mathbf{X}_0)(\mathbf{X} - \mathbf{X}_0) \tag{3.21}$$

Since the solution is achieved at $\mathbf{F}(\mathbf{X}) = 0$, Equation (3.21) is written in the following iterative form:

$$\mathbf{F}(\mathbf{X}_j) + D\mathbf{F}(\mathbf{X}_j)(\mathbf{X}_{j+1} - \mathbf{X}_j) = 0 \tag{3.22}$$

where $\mathbf{X_j}$ and $\mathbf{X}_{j+1}$ are the current and next iteration of the free variable vector, respectively, and $\mathbf{F}(\mathbf{X}_j)$ is the value of the current constraint vector evaluated by propagating the equations of motion using the initial condition $\mathbf{X_j}$. Meanwhile, $D\mathbf{F}(\mathbf{X}_j)$ is calculated in terms of the current free variable and constraint vectors and it will be discussed later in detail. Rearranging Equation (3.22) to solve for $\mathbf{X}_{j+1}$ yields:

$$\mathbf{X}_{j+1} = \mathbf{X}_j - D\mathbf{F}(\mathbf{X}_j)^{-1}\mathbf{F}(\mathbf{X}_j) \tag{3.23}$$

Starting from an initial guess, iteration stops when $||\mathbf{F}(\mathbf{X}_{j+1})||_2 < \epsilon$, where ϵ is a predefined tolerance while the subscript, 2, refers to the $L2$ norm. It should be noted, however, that if the design vector includes more free variables than the constraint vector, or $n > m$, the $D\mathbf{F}(\mathbf{X})$ matrix becomes non square and therefore, the the minimum norm solution is selected to solve this problem as:

$$\mathbf{X}_{j+1} = \mathbf{X}_j - D\mathbf{F}(\mathbf{X}_j)^T(D\mathbf{F}(\mathbf{X}_j)D\mathbf{F}(\mathbf{X}_j)^T)^{-1}\mathbf{F}(\mathbf{X}_j) \tag{3.24}$$

Note that the minimum norm solution was selected because it seeks a solution as close as possible to the initial guess, which allows preserving the characteristics of the initial free variable vector.

3.2.1 Simple Targeting Scheme Formulation

A simple targeting scheme, also called a single shooting method, is one of the most basic correction strategies; a single trajectory arc with the appropriate initial state vector is the solution to a two-point boundary value problem. The formulation of the free variable vector and constraint vector is problem dependent, however, the elements of the algorithm are consistent. Having the spacecraft initial state defined as:

$$\mathbf{x}(t_0) = \begin{bmatrix} x(t_0) & y(t_0) & z(t_0) & \dot{x}(t_0) & \dot{y}(t_0) & \dot{z}(t_0) \end{bmatrix}^T \tag{3.25}$$

starting from the initial time, t_0, the first-order equations of motion in Equation (3.1) are propagated to some later time, $t_0 + T$, such that the spacecraft arrives at some point downstream at the state $\mathbf{x}(t_0 + T)$. By modifying the initial state values (position and/or velocity), the spacecraft arrives at an alternative downstream location. As shown in Figure 3.1, to determine an initial state such that the final state of the spacecraft is equal to some desired final position state, $\mathbf{x}_d(t_0 + T)$, the shooting scheme employs the update equation in Equation (3.23) or Equation (3.24). Note that in the single shooting approach, the design variable vector, $\mathbf{X}$, includes initial state elements, while the constraint equation, $\mathbf{F}(\mathbf{X})$, incorporates constraints to enforce some desired final state.

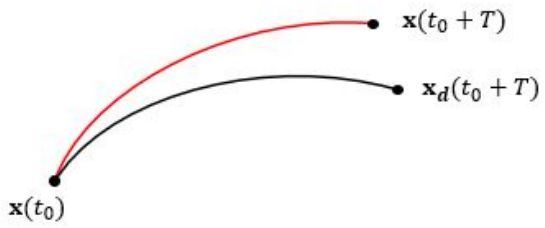

Figure 3.1: Single-shooting corrections algorithm schematic.

3.2.2 Multi-Segment Corrections Algorithm Formulation

In more complex design problems, or for longer integration times, a multi-segment corrections algorithm is better suited than the single shooting scheme. A multiple shooting method simultaneously solves several two-point boundary value problems to meet design constraints. To formulate a multiple shooting procedure, a trajectory must be discretized into $(n-1)$ segments, or arcs, that are separated by n patchpoints, or nodes. As shown in Figure 3.2, $\mathbf{x}_i^0$ and $\mathbf{x}_i^f$ refer to the initial and final desired state vectors corresponding to patch-point i while T_i refers to the integration time along segment i. Note that the initial guess of the state vector at the patchpoints and the resulting arcs do not necessarily yield a continuous path. Therefore, continuity constraints, in the form of $\mathbf{x}_{i-1}^f - \mathbf{x}_i^0$, are employed to enforce full state continuity along the converged trajectory.

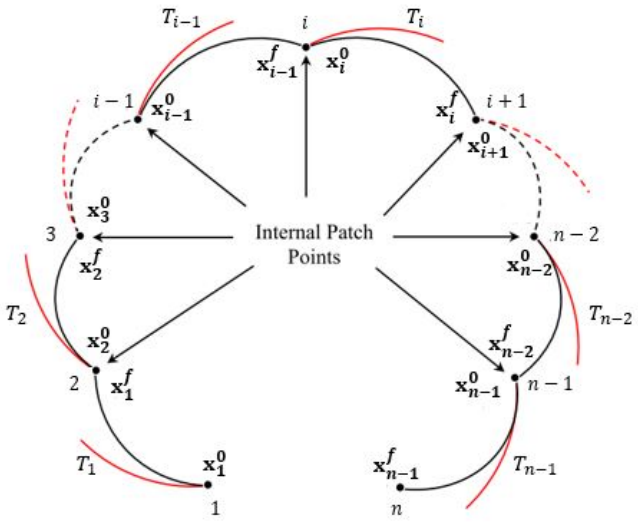

Figure 3.2: Multi-shooting corrections algorithm schematic.

3.3 Continuation of an Orbit Family

Single shooting and multiple shooting schemes are employed to compute a single point solution for a trajectory based on one given set of initial conditions. In general, it is useful to construct a range of related solutions, or a family, if possible. Families of orbits deliver insight into the dynamical characteristics across an entire region and offer various options for trajectory design. Additionally, since a family of orbits spans a range of characteristics, an individual orbit, or family member, is then able to be selected more carefully to meet mission requirements. Multiple strategies to compute families of orbits exist; for example, a natural parameter continuation scheme offers a straightforward approach to compute a family member based on a previously converged solution. Additionally, a strategy that requires less intuition and a broader range of applications, the pseudo-arclength continuation scheme, is also an option.

To begin, a single converged solution is determined by implementing a numerical corrections process given some initial guess. For example, as described previously, a single shooting easily delivers a periodic orbit. Then, one parameter associated with the converged solution is varied by a small amount. The previously converged solution, now with one varied parameter, is then employed as an initial guess for a new trajectory in a new differential corrections process. The natural parameter continuation process is then repeated to construct additional related trajectories. This continua-

tion scheme applies to both periodic orbits and non-periodic trajectory arcs. Although natural parameter continuation is insightful and straightforward to implement, it requires intuition of selecting the appropriate size for the parameter depending on its sensitivity to the solution.

Using the eccentricity as a continuation parameter, a family of related solutions can associate the solution obtained in the CR3BP to a solution in the ER3BP. In this investigation, therefore, natural parameter continuation is used to move the reference periodic halo orbit from the CR3BP to the ER3BP using the eccentricity of the Moon's orbit as the continuation parameter.

3.4 Periodic Orbits in the CR3BP

As mission concepts are increasingly demanding orbits with repeating predictable behavior, periodic orbits are employed in a variety of trajectory design and mission applications, such as a long-duration lunar orbiter or a deep-space telescope. Precisely, periodic motion exists in the CR3BP about the primaries and in the vicinity of the Lagrange points. A simple type of periodic motion appears in the form of symmetric orbits in the CR3BP. Although other types of non-symmetric periodic motion exist, xz-symmetric orbits are the primary focus in this investigation, and therefore, a strategy to numerically compute this type of periodic motion is introduced. Any numerical corrections algorithm requires a reasonable starting point or guess. An initial guess for trajectory arcs in the CR3BP can originate from a variety of sources; for periodic solutions near libration points, a linear approximation of the behavior serves as a straightforward initial guess for the true motion; periodic behavior about the primary bodies is reasonably approximated as a two-body Keplerian solution; as a third option, initial guesses also originate from previously converged solutions. Given an initial guess, the corrections process in the CR3BP proceeds.

A single shooting algorithm serves as the basis for a simple and efficient corrections process to compute symmetric periodic trajectories. Solutions are constructed by constraining the departure and arrival condition at the $\hat{x}\hat{z}$-plane crossing to be perpendicular. To illustrate the process, a state on the $\hat{x}\hat{z}$-the plane is selected, such that $y_0 = 0$, where the subscript 0 represents the initial state. Meanwhile, to ensure a periodic departure from the $\hat{x}\hat{z}$-plane, $\dot{x}_0 = \dot{z}_0 = 0$. The initial condition vector is, therefore, of the form:

$$\mathbf{x}_0 = \begin{bmatrix} x_0 & 0 & z_0 & 0 & \dot{y}_0 & 0 \end{bmatrix}^T \tag{3.26}$$

Accordingly, the following free variable vector, considering a fixed-time shooting method, is constructed to maintain the initial condition as:

$$\mathbf{X} = \begin{bmatrix} x_0 \\ z_0 \\ \dot{y}_0 \end{bmatrix} \tag{3.27}$$

Note that omitting any of the states in the free-variable vector essentially forces the missing variable to remain equal to the value assumed in the initial guess, $\mathbf{X}$. The constraints on the state variables used to enforce a downstream perpendicular $\hat{x}\hat{z}$-plane crossing are then defined as:

$$\mathbf{F}(\mathbf{X}) = \begin{bmatrix} y(T_{1/2}) \\ \dot{x}(T_{1/2}) \\ \dot{z}(T_{1/2}) \end{bmatrix} \tag{3.28}$$

where $T_{1/2}$ is the half-period time. Taking into account the definition of the STM, the Jacobian matrix $D\mathbf{F}(\mathbf{X})$ is found as:

$$D\mathbf{F}(\mathbf{X}) = \begin{bmatrix} \phi_{21} & \phi_{23} & \phi_{25} \\ \phi_{41} & \phi_{43} & \phi_{45} \\ \phi_{61} & \phi_{63} & \phi_{65} \end{bmatrix} \tag{3.29}$$

where ϕ_{ij} corresponds to elements of the STM evaluated at time $T_{1/2}$. After performing the iteration process and acquiring the solution, the periodic orbit is obtained by integrating the converged initial state for $T_C = 2T_{1/2}$.

3.4.1 Halo Orbit around the L2 Point

In the Earth-Moon gravitational regime, a critical element in constructing three-dimensional halo orbits is the initial guess of the state vector. An initial guess for an L_2 halo orbit is available from many previous authors. In this investigation, an initial guess for a northern L_2 halo orbit is obtained from Narula [73] as:

$$\mathbf{x}_0 = \begin{bmatrix} 1.1354 & 0 & 0.1699 & 0 & -0.2247 & 0 \end{bmatrix}^T \tag{3.30}$$

An estimated period of this particular halo orbit is 3.064 non-dimensional units, or 13.30536 days. Using the single shooting algorithm for a fixed half period, $T_{1/2} = \pi/2$, and setting a tolerance for the iterative process of

$\epsilon = 1e^{-13}$, the initial condition is updated to:

$$\mathbf{x}_0 = \begin{bmatrix} 1.14375036395082 \\ 0 \\ 0.157506628901081 \\ 0 \\ -0.221868821703559 \\ 0 \end{bmatrix} \tag{3.31}$$

Note that the converged solution is obtained for a periodic orbit of a period $T_C = \pi$ non-dimensional units, or 13.6423 days. The periodic halo orbit that corresponds to the updated initial condition is shown in Figure 3.3.

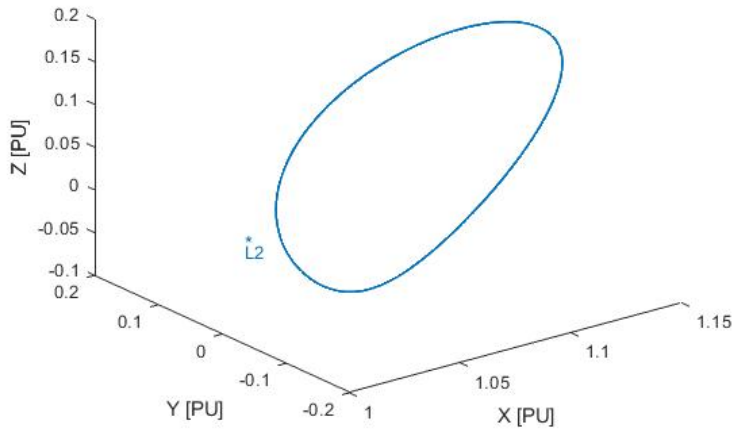

Figure 3.3: The reference L_2 halo orbit in the CR3BP expressed in the rotating coordinates where the Position Unit (PU) is the characteristic length, l^*.

3.5 Periodic Orbits in the ER3BP

The right-hand side of the equations of motion in Equation (2.40) is periodic with a period 2π, and thus, periodic solutions of the ER3BP must have a principal period $T_E = 2N\pi$, $N = 1, 2, ...$; they are also periodic in the inertial reference frame. Under such considerations, Moulton [23] formulated the periodicity criterion of planar orbits in the ER3BP such that to have two perpendicular crossings, with respect to the $\hat{x}\hat{z}$-plane, when the two primaries are at an apse. Later, Broucke [36] used Moulton's criterion to compute

planar orbits in the ER3BP, starting from periodic orbits in the CR3BP, for different eccentricities using a continuation method. In particular, he managed to obtain two branches of orbits, periapsis orbits and apoapsis orbits, depending on the true anomaly of the primaries at the starting point on the $\hat{x}$-axis. This criterion was later extended to three-dimensional orbits by Ichtiaroglou [38] and Michalodimitrakis [39]. Recently, Campagnola [41] succeeded in computing periodic halo orbits in the ER3PB, which he called elliptic halo orbits since they bifurcate from special halo orbits of the CR3BP.

To compute an elliptic halo orbit, a halo orbit in the CR3BP is first chosen to have a period $T_C = 2r\pi$, where $r = \frac{N}{M}$ is the resonant ratio between the number of the primary revolutions, N, and the number of the spacecraft revolutions, M. Accordingly, by assembling M revolutions of the halo orbit, an elliptic halo orbit is built with a period $T_E = MT_C = 2N\pi$, which is the solution of Equation (2.40) at $e = 0$, and $2M$ perpendicular crossings with respect to the $\hat{x}\hat{z}$-plane. Later, the eccentricity is used as a continuation parameter to compute the periodic orbit for $e = 0.0549$, which is the eccentricity of the Moon's orbit around the Earth.

As the orbit in the ER3BP requires a longer integration time and due to the high sensitivity with respect to the eccentricity, a multi-shooting method is used. The halo orbit was divided into $n_s = 8$ segments, each with an integration time $T_s = T_E/n_s$. Following the methodology of free variable and constraint method, the free variable vector is constructed as:

$$\mathbf{X} = \begin{bmatrix} \mathbf{x}_1^0 \\ \vdots \\ \mathbf{x}_7^0 \\ \mathbf{x}_8^0 \\ T_s \end{bmatrix} \tag{3.32}$$

Meanwhile, continuity constraints were enforced for all segments, perpendicular crossing only for the final segment, and the final period to 2π. Accordingly, the constraint vector is expresses as:

$$\mathbf{F}(\mathbf{X}) = \begin{bmatrix} \mathbf{x}_1^f - \mathbf{x}_2^0 \\ \vdots \\ \mathbf{x}_7^f - \mathbf{x}_8^0 \\ \mathbf{x}_8^f - \mathbf{x}_1^0 \\ \mathbf{F}(\mathbf{X}_8) \\ 8T_s - 2\pi \end{bmatrix} \tag{3.33}$$

where $\mathbf{F}(\mathbf{X}_8)$ is similar to Equation (3.28) but evaluated for the last segment

at $8T_s$. Meanwhile, the Jacobian matrix is constructed as:

$$D\mathbf{F}(\mathbf{X}) = \begin{bmatrix} \boldsymbol{\Phi}_1 & -\mathbf{I}_{6\times6} & & & \dot{\mathbf{x}}_1^f \\ & \ddots & \ddots & & \vdots \\ & & \ddots & \ddots & \vdots \\ & & \boldsymbol{\Phi}_7 & -\mathbf{I}_{6\times6} & \dot{\mathbf{x}}_7^f \\ -\mathbf{I}_{6\times6} & & & \boldsymbol{\Phi}_8 & \dot{\mathbf{x}}_8^f \\ & & & \boldsymbol{\Phi}_8(2,4,6) & \dot{\mathbf{F}}(\mathbf{X}_8) \\ & & & & 8 \end{bmatrix} \tag{3.34}$$

where $\boldsymbol{\Phi}_i$ refers to the STM matrix of segment i evaluated from $(i-1)T_s$ to iT_s, $\boldsymbol{\Phi}_i(2,4,6)$ is a matrix containing the second, forth, and sixth raws of the STM matrix of segment i, and the non-dotted elements are all zeros.

3.5.1 Elliptic Halo Orbit around the L2 Point

Similar to the CR3BP, the procedure of generating a periodic halo orbit starts from selecting an accurate initial guess. Following the initial conditions obtained in Equation (3.31), natural parameter continuation is performed using the multi-segment differential correction method. However, this method has some limitations [47] represented by its low convergence domain for nonlinear problems and its high failure probability for long integration times even for a precise initial guess. Moreover, it was shown during the implementation that this method is highly sensitive to the continuation step, requiring a step lower than 10^{-4}, which has considerably increased the simulation time. To avoid those problems, several authors have introduces low-cost alternatives, such as the multiple (or two-level) differential correction method [101], the evolutionary optimization method [102], and the nonlinear programming optimization method [47].

In this investigation, the nonlinear programming optimization method was adopted by implementing the multi-shooting problem using mature solvers. This method possesses considerable advantages comparing with the traditional differential correction method, such as the low simulation cost, high convergence rate even when starting with rough initial conditions, and the ability to select a higher continuation step, e.g. higher than 10^{-3}. The same problem, in terms of the free variable and constraint vectors, is implemented using the *fmincon* optimization function in MATLAB. As provided in Appendix A.1, the optimization variable was taken from the free variable vector in Equation (3.32), meanwhile, the constraint vector in Equation (3.33) was setup as follow; continuity constraints in the nonlinear constraint

function; perpendicular constraints in the cost function; the period constraint as a linear equality. It should be noted that the segments initial conditions of the optimization process were extracted from the halo orbit in the CR3BP shown in Figure 3.3. Moreover, to decrease the simulation cost even more, while keeping accurate results, strict optimization options, in terms of tolerances, steps, and evaluation limits, were only enforced at the final continuation step. Applying the algorithm in Appendix A.1, the resulting initial conditions are obtained as:

$$\mathbf{x}_0 = \begin{bmatrix} 1.14520421356342 \\ 0 \\ 0.160866058153171 \\ 0 \\ -0.220906655170176 \\ 0 \end{bmatrix} \tag{3.35}$$

which corresponds to the periodic elliptic halo orbit shown in Figure 3.4. The obtained orbit is bifurcated from the halo orbit in the CR3BP shown in Figure 3.3, and since the orbit starts at $\theta_0 = 0$ from the right side, it belongs to the right group elliptic halo orbits [47]. Moreover, it consists of $M = 4$ revolutions with a period $T_E = 2\pi$.

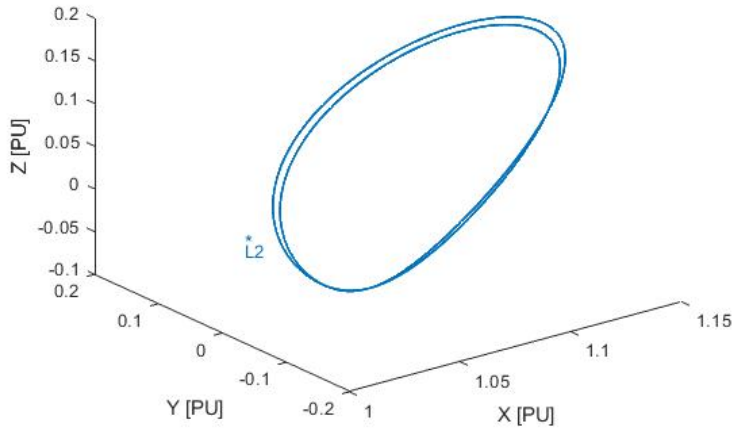

Figure 3.4: The reference L_2 halo orbit in the ER3BP expressed in the pulsating-rotating coordinates where the Position Unit (PU) is the characteristic length, l^*.

Chapter 4

Station Keeping

A variety of station-keeping strategies have been previously investigated for missions in the Sun-Earth system [2] while only a few are devoted to the Earth-Moon system. After the success of the ARTEMIS mission [103], the complex dynamics of libration point in the Earth-Moon system has entered a new era. In particular, the neighborhood of the L_2 point can be used for monitoring, or establishing permanent links, of the lunar far-side, as suggested by Farquhar in 1966 [26]. Libration point orbits in the Earth-Moon system acquire an intrinsic unstable behavior, which leads to fast divergence along with their unstable manifolds if no control is applied [100]. Moreover, the station-keeping for those orbits is considered more challenging [73], mainly due to the shorter time scale and the large orbital eccentricity of the Moon. Therefore, successful station-keeping is required to account for this unstable motion and maintain the spacecraft on, or at least close to, the reference nominal orbit.

4.1 Reference Orbit Representation

In this section, the reference orbit calculated in Chapter 3 is adopted to be used in the station-keeping problem. Since the acquired elliptic halo orbit in Figure 3.4 starts diverging after two periods, two methods are introduced to obtain a periodic orbit that is repeated over the entire time of the simulation to be used as reference orbit for the station-keeping.

4.1.1 Fourier Series

In order to use the state vector acquired from the optimization process as a reference, the data of each component is fitted to a Fourier series of the 8th

order as:

$$s(t) = a_0^s + \sum_{i=1}^{8} \left(a_i^s \cos\left(i\omega^s t\right) + b_i^s \sin\left(i\omega^s t\right) \right) \tag{4.1}$$

where x refers to any component of the state vector, coordinates and velocities, a^s, b^s, and ω^s are the Fourier coefficients associated to that components, and t is the non-dimensional time, which is the true anomaly in the ER3BP. Meanwhile, the curve fitting tool in MATLAB was used to generate the coefficients for all the components as provided in Appendix A.2. The acquired Fourier series equations can generate a roughly periodic orbit even for 500 periods, $t = 1000\pi$, as shown in Figure 4.1

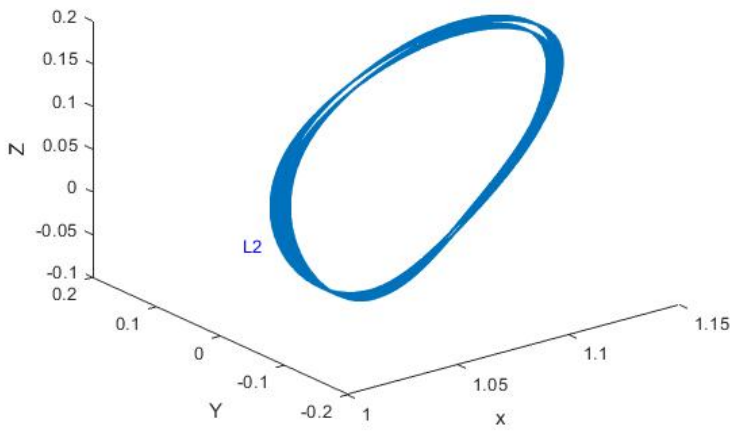

Figure 4.1: The reference L_2 elliptic halo orbit generated using the Fourier series method and propagated for 500 periods.

4.1.2 Interpolation

In this research, the interpolation method is used for its high accuracy in computing the reference orbit comparing with the Fourier series method. For this purpose, the state vector that corresponds to the reference orbit in Figure 3.4 is discretized into 10000 iterations ranging from $t = [0 - 2\pi]$. The spline method was then used to interpolate the state vector over the time range. Meanwhile, the simulation time was scaled to the interpolation range using the following equation:

$$t_s = t - T_E floor(\frac{t}{T_E}) \tag{4.2}$$

where t is the simulation time, t_s is the scaled time $[0-2\pi]$, and the $floor(x)$ function rounds the value of x to the nearest integer less than or equal to x. Using this method, the reference orbit, even if propagated for 500 periods, is identical to Figure 3.4.

4.2 Station-Keeping Constraints

In real missions, the execution of a station-keeping maneuver is subjected to several practical constraints. For example, a maneuver can be canceled (even if advised) during the operation of sensitive equipment. In this case, the station-keeping process is disrupted and postponed to the next control period, posing a challenge to the robustness of the controller. Three constraints have been considered in the simulations, as proposed in [82, 55], and are listed below.

4.2.1 Minimum Time Interval

The first constraint is a minimum time interval between two consecutive maneuvers, denoted by Δt_{min}. This constraint states that the station-keeping maneuvers should be as infrequent as possible because the maneuver execution may have negative impacts on the scientific operations. Only when the time elapsed from the previous maneuver is greater than Δt_{min}, the next one will be allowed. The selection of this value is highly connected to the number of required maneuvers-per-orbit. Assuming that the distribution of correction impulses to be nonuniform in time and that the orbit determination errors are much lower than the maneuver execution, the optimal number of correction maneuvers per orbit is found analytically [2] as:

$$N_{opt} = [2\pi \frac{\log(\mu_1)}{T}] \tag{4.3}$$

where the square brackets denote the integer part, T is the orbital period, and $\mu_1 = 2.4553 \times 10^4$ is the largest eigenvalue of the monodromy matrix, $\mathbf{\Phi}(T, 0)$, which was computed for the elliptic halo orbit shown in Figure 3.4. The minimum time between maneuvers is then calculated as:

$$\Delta t_{min} = \frac{T}{N_{opt}} \tag{4.4}$$

4.2.2 Minimum Maneuver Magnitude

The second constraint is about the magnitude of the maneuver, which must have a lower threshold to avoid tiny ones and is denoted as Δv_{min}. It is due to

the fact that unavoidable errors exist in the implementation of a maneuver, and if the requested maneuver is of the same order of magnitude as the error, it makes no sense to perform it and, therefore, should be canceled.

4.2.3 Minimum Position Deviation

The third constraint is a limit to the position deviation with respect to the nominal orbit, denoted as Δr_{min}. This threshold sets a radius of a torus surrounding the nominal trajectory such that if the spacecraft is within this torus, then it is assumed ″on″orbit and no maneuver should be performed, otherwise, the spacecraft is considered far from the orbit and a maneuver is required.

The values of those constraints are summarized in Table 4.1. Note that while Δt_{min} was calculated using Equation (4.4), Δv_{min} and Δr_{min} were selected similarly to [65].

Table 4.1: Simulation constraints.

Constraint	Value
Δt_{min} $[days]$	2.47
Δv_{min} $[mm/sec]$	1
Δr_{min} $[km]$	0.3

4.3 Station-Keeping Errors

In real missions, there are various unavoidable errors which must be taken into account when assessing the performance of the station-keeping approach. In this work, the three errors were considered similar to [65]; injection, tracking and maneuver execution errors.

4.3.1 Injection Error

Injection error occurs when the spacecraft is injected into the nominal orbit, i.e., when it gets the same position and velocity of a chosen point on the orbit. However, only an approximate state can be accomplished due to various uncertainties. The residual between the two states is the orbit injection error. This error is implemented in the simulation as a perturbation to the initial conditions calculated in Equation (3.35).

4.3.2 Tracking Error

Tracking error, or navigation error, comes from the measurement uncertainties of the determination of the spacecraft state and misleads the controller to exert inaccurate impulses. Moreover, navigation methods play a major role in determining the order of this error [104], e.g. while the full-disk optical navigation yields a position error $< 10^2$ $[km]$, radiometric tracking reduces the error to the order of meters. This error is generally included in the station-keeping problem as measurement perturbations.

4.3.3 Maneuver Execution Error

Maneuver execution error arises from the imperfection of the manufacturing or installation of the thrusters, which leads to inaccuracy in both the magnitude and the direction of the impulse. This error is implemented as a perturbation to the calculated impulse.

All the errors are assumed to have normal distributions with zero means and standard deviations (Std.) as given in Table 4.2, where three sets of values were considered for the injection/tracking errors; (I) small position and velocity errors; (II) large position error and small velocity error; (III) large position and velocity errors. The aim of using different combinations of position and velocity errors is to identify their respective impact on the performance of the controller. Meanwhile, the numbers were selected in compliance with the expected navigation performances of the LUMIO mission in case of autonomous full-disk optical navigation [97, 104].

Table 4.2: Normal distribution standard deviations of the station-keeping errors.

Error	Std.	Case I	Case II	Case III
Injection/tracking	$\sigma_{\lvert r\rvert}$ $[km]$	1	10	10
	$\sigma_{\lvert v\rvert}$ $[mm/sec]$	1	1	100
Maneuver	$\sigma_{\lvert \Delta \mathbf{v}\rvert}$ [%]	2	2	2

4.4 Discrete Linear Quadratic Regulator

In this section, the application of a discrete linear quadratic regulator (DLQR) is investigated using the finite-horizon case. The discrete version was adopted in this work because of its common use in the operational environment, especially that maneuver planning is not just a function of trajectory correction

needs [105], but also spacecraft operations, science operations, momentum management, and communication requirements.

A detailed investigation of the DLQR can be found in [65], where it was used for solving the station-keeping problem in both the CR3BP and the full ephemeris model. In this section, the design methodology used in [65] is revisited in detail and adopted for the station-keeping problem in the ER3BP. After constructing the reference orbit, the DLQR control algorithm is exploited to overcome the instabilities and keep the spacecraft in orbit. Starting from the definition of the STM, by substituting Equation (3.9) in Equation (3.6), the state variation is expressed linearly as:

$$\delta\mathbf{x}(t) = \mathbf{\Phi}(t, t_0)\delta\mathbf{x}(t_0) \tag{4.5}$$

where $\delta\mathbf{x}(t) = \mathbf{x}(t) - \mathbf{x}_{ref}(t)$ and the STM is found by solving Equation (3.10). Rewriting Equation (4.5) in the discrete form:

$$\delta\mathbf{x}(k_c + 1) = \mathbf{\Phi}(k_c + 1, k_c)\delta\mathbf{x}(k_c) \tag{4.6}$$

where k_c denotes the iteration time step of the DLQR, where the orbit was divided into a discrete number of nodes, N. Given an impulsive maneuver, denoted $\Delta\mathbf{v} \in \mathbb{R}^3$, applied at iteration time step k_c, Equation (4.6) is augmented including the velocity increment as:

$$\delta\mathbf{x}(k_c + 1) = \mathbf{\Phi}(k_c + 1, k_c)\delta\mathbf{x}(k_c) + \mathbf{\Phi}(k_c + 1, k_c)\overline{\mathbf{B}}\Delta\mathbf{v}(k_c) \tag{4.7}$$

where $\overline{\mathbf{B}} = [\mathbf{0}_{3\times3}, \mathbf{B}_2]^T$. Setting $\mathbf{B}_2 = \mathbf{I}_{3\times3}$ means that the three components of the control are used. Equation (4.7) is rewritten as:

$$\delta\mathbf{x}(k_c + 1) = \mathbf{A}\delta\mathbf{x}(k_c) + \mathbf{B}\Delta\mathbf{v}(k_c) \tag{4.8}$$

where

$$\mathbf{A} = \mathbf{\Phi}(k_c + 1, k_c)$$
$$\mathbf{B} = \mathbf{\Phi}(k_c + 1, k_c)\overline{\mathbf{B}}$$

For the presented discrete-time system, a cost function, J, is chosen such that it incorporates the time histories of both the system state, $\delta\mathbf{x}$, and the control, $\Delta\mathbf{v}$, as:

$$J(U) = \sum_{k_c=0}^{N-1} \left(\delta\mathbf{x}(k_c)^T\mathbf{Q}\delta\mathbf{x}(k_c) + \Delta\mathbf{v}(k_c)^T\mathbf{R}\Delta\mathbf{v}(k_c)\right) + \delta\mathbf{x}(N)^T\mathbf{Q}_f\delta\mathbf{x}(N) \tag{4.9}$$

where $U = (\Delta\mathbf{v}(0), \ldots, \Delta\mathbf{v}(N\text{-}1))$ denotes a control sequence, $\mathbf{Q}$ and $\mathbf{Q}_f \in \mathbb{R}^{6\times6}$ are positive semi-definite state weighting matrices, and $\mathbf{R} \in \mathbb{R}^{3\times3}$

is the positive definite control weighting matrix. The aim of the control algorithm is then to find the optimal control sequence that minimises the cost function. Therefore, the number of impulses per one period, N, is calculated for the optimal case using Equation (4.3) and its value is shown in Table 4.3 alongside the DLQR sampling time, T_c, which is computed similar to Equation (4.4).

By introducing the Dynamic Programming (DP) method to solve the LQR Discrete-time finite-horizon problem [106], the solution is summarized in the following steps:

- Solving the Ricatti Equation backward in time, for $k_c = N, \ldots, 1$, with the boundary condition $\mathbf{P}(N) = \mathbf{Q}_f$.

$$\mathbf{P}(k_c{-}1) = \mathbf{A}^T\mathbf{P}(k_c)\mathbf{A} - \mathbf{A}^T\mathbf{P}(k_c)\mathbf{B}\big(\mathbf{R}{+}\mathbf{B}^T\mathbf{P}(k_c)\mathbf{B}\big)^{-1}\mathbf{B}^T\mathbf{P}(k_c)\mathbf{A}{+}\mathbf{Q} \tag{4.10}$$

- Calculating the LQR gain matrix, for $k_c = 0, \ldots, N$ - 1.

$$\mathbf{K}(k_c) = \big(\mathbf{R} + \mathbf{B}^T\mathbf{P}(k_c)\mathbf{B}\big)^{-1}\mathbf{B}^T\mathbf{P}(k_c)\mathbf{A} \tag{4.11}$$

- Calculating the linear state-feedback control vector, for $k_c = 0, \ldots, N$-1.

$$\Delta\mathbf{v}(k_c) = -\mathbf{K}(k_c)\delta\mathbf{x}(k_c) \tag{4.12}$$

where the weighting matrices were selected as:

$$\begin{aligned} \mathbf{Q} &= \mathbf{Q}_f = \mathbf{C}^T\mathbf{C} = \mathbf{I}_{6\times6} \\ \mathbf{R} &= \rho_c\mathbf{I}_{3\times3} \end{aligned} \tag{4.13}$$

where $\mathbf{C}$ is the control matrix that maps the state vector to the output vector, which are the same, and ρ_c is the weight factor of the control with respect to the state error. If $\rho_c > 1$, the control effort is penalized with respect to the performance and the opposite is true if $\rho_c < 1$. Note that ρ_c is the only variable that needs to be tuned in the design of the DLQR and its value was selected as shown in Table 4.3.

Table 4.3: DLQR tuning parameters.

Parameter	Value
N	11
T_c $[days]$	2.47
ρ_c	1.5

4.5 Discrete Linear Extended State Observer

Extended state observers (ESOs) are generally introduced to estimate the disturbances affecting the dynamical model. In application to the station-keeping problem, a continuous linear ESO was introduced by Narula in [73], meanwhile, continuous and discrete nonlinear ESOs are investigated by Gao et al. [72]. Continuous versions, however, are not preferred for the operation of the controllers in the real world, meanwhile, the nonlinear approach requires many tuning parameters, is difficult to implement, and has both switching and sliding functions that may cause chattering. In this work, therefore, a discrete linear ESO (DLESO) is designed to have a few tuning parameters for easy and efficient implementation, meanwhile, a discrete version was chosen for being suitable for digital processing and impulsive thrusters.

The general design and implementation of discrete linear ESOs are detailed in [107], where the authors compare different types of linear ESOs and their effects on the performance. As shown in [107], the current discrete ESO with zero-order hold (ZOH) discretization method should be used for improved tracking accuracy and closed-loop stability. Moreover, the ZOH offers better accuracy in estimating the transient velocity with respect to the Euler discretization method. Therefore, in this work, the current type of ESO was adopted with ZOH as a discretization method.

Considering the following second-order system [72]:

$$\ddot{\mathbf{y}}(t) = f(\mathbf{y}, \dot{\mathbf{y}}, \mathbf{w}(t), t) + \mathbf{B}_2\mathbf{u}(t) \tag{4.14}$$

where $\mathbf{y}$ is the output and represents the position, $\mathbf{u}$ is the control input, $\mathbf{B}_2 = \mathbf{I}_{3\times3}$ represents the applicability of the control along the three directions, and $f(\mathbf{y}, \dot{\mathbf{y}}, \mathbf{w}(t), t)$ represents three parts: modelled dynamics, uncertain dynamics, and disturbance. Defining the reference model by the second-order equation:

$$\ddot{\mathbf{y}}_{ref}(t) = f_{ref}(\mathbf{y}_{ref}, \dot{\mathbf{y}}_{ref}, t) + \mathbf{B}_2\mathbf{u}_{ref}(t) \tag{4.15}$$

where $\mathbf{y}_{ref}$ is the output and represents the reference position, $\mathbf{u}_{ref}$ represents the reference control, and $f_{ref}(\mathbf{y}_{ref}, \dot{\mathbf{y}}_{ref}, t)$ represents one part: modelled dynamics. Then, by subtracting Equation (4.15) from Equation (4.14), the following equation is obtained:

$$\delta\ddot{\mathbf{y}} = d(\delta\mathbf{y}, \delta\dot{\mathbf{y}}, \mathbf{w}(t), t) + \mathbf{B}_2\delta\mathbf{u} \tag{4.16}$$

where $\delta\mathbf{y}$, $\delta\dot{\mathbf{y}}$, and $\delta\mathbf{u}$ represent the position, velocity, and control deviation vectors, respectively, while $d(\delta\mathbf{y}, \delta\dot{\mathbf{y}}, w(t), t)$ represents two parts: uncertain

dynamics and disturbances. In fact, in the context of feedback control, $d(\delta\mathbf{y}, \delta\dot{\mathbf{y}}, w(t), t)$, is something to be overcome by the control signal, and therefore, it is denoted as the total disturbance. Equation (4.16) is then rewritten in an augmented, or extended, steady-state form as:

$$\begin{aligned} \delta\dot{\mathbf{x}}_{aug}(t) &= \mathbf{A}_{aug}(t)\delta\mathbf{x}_{aug}(t) + \mathbf{B}_{aug}\delta\mathbf{u}(t) \\ \delta\mathbf{y} &= \mathbf{C}_{aug}\delta\mathbf{x}_{aug}(t) \end{aligned} \tag{4.17}$$

where the augmented state vector, $\delta\mathbf{x}_{aug} = [\delta\mathbf{y}, \delta\dot{\mathbf{y}}, \mathbf{f}]^T$, includes the position deviation, velocity deviation, and disturbance vectors, respectively, while the augmented system matrices are given as:

$$\begin{aligned} \mathbf{A}_{aug} &= \begin{bmatrix} \mathbf{0}_{3\times3} & \mathbf{I}_{3\times3} & \mathbf{0}_{3\times3} \\ \mathbf{0}_{3\times3} & \mathbf{0}_{3\times3} & \mathbf{I}_{3\times3} \\ \mathbf{0}_{3\times3} & \mathbf{0}_{3\times3} & \mathbf{0}_{3\times3} \end{bmatrix}, \quad \mathbf{B}_{aug} = \begin{bmatrix} \mathbf{0}_{3\times3} \\ \mathbf{B}_2 \\ \mathbf{0}_{3\times3} \end{bmatrix} \\ \mathbf{C}_{aug} &= \begin{bmatrix} \mathbf{I}_{3\times3} & \mathbf{0}_{3\times3} & \mathbf{0}_{3\times3} \end{bmatrix} \end{aligned} \tag{4.18}$$

Applying discretization, Equation (4.17) is written as:

$$\begin{aligned} \delta\mathbf{x}(k_o+1) &= \mathbf{\Phi}_{aug}\delta\mathbf{x}(k_o) + \overline{\mathbf{\Gamma}}_{aug}\delta\mathbf{u}(k_o) \\ \delta\mathbf{y}(k_o) &= \mathbf{H}_{aug}\delta\mathbf{x}(k_o) \end{aligned} \tag{4.19}$$

where k_o denotes the iteration time step of the DLESO, meanwhile, the discretized augmented system matrices are found using the ZOH as:

$$\begin{aligned} \mathbf{\Phi}_{aug} &= e^{\mathbf{A}_{aug}T_o} = \sum_{k_o=0}^{\infty} \frac{\mathbf{A}_{aug}^{k_o} T_o^{k_o}}{(k_o)!} \\ \overline{\mathbf{\Gamma}}_{aug} &= \int_0^{T_o} e^{\mathbf{A}_{aug}\tau} d\tau \mathbf{B} = \sum_{k_o=0}^{\infty} \frac{\mathbf{A}_{aug}^{k_o} T_o^{k_o+1}}{(k_o+1)!} \\ \mathbf{H}_{aug} &= \mathbf{C}_{aug} \end{aligned} \tag{4.20}$$

where T_o is the sampling time of the DLESO. Applying Equation (4.20) to Equation (4.18), the discrete augmented system matrices are found as:

$$\begin{aligned} \mathbf{\Phi}_{aug} &= \begin{bmatrix} \mathbf{I}_{3\times3} & \mathbf{I}_{3\times3}T_o & \mathbf{I}_{3\times3}\frac{T_o^2}{2} \\ \mathbf{0}_{3\times3} & \mathbf{I}_{3\times3} & \mathbf{I}_{3\times3}T_o \\ \mathbf{0}_{3\times3} & \mathbf{0}_{3\times3} & \mathbf{I}_{3\times3} \end{bmatrix}, \quad \overline{\mathbf{\Gamma}}_{aug} = \begin{bmatrix} \mathbf{B}_2\frac{T_o^2}{2} \\ \mathbf{B}_2T_o \\ \mathbf{0}_{3\times3} \end{bmatrix} \\ \mathbf{H}_{aug} &= \begin{bmatrix} \mathbf{I}_{3\times3} & \mathbf{0}_{3\times3} & \mathbf{0}_{3\times3} \end{bmatrix} \end{aligned} \tag{4.21}$$

However, since the intended control vector is an impulsive force, velocity increment, instead of an acceleration force, Equation (4.19) is rewritten as:

$$\begin{aligned} \delta\mathbf{x}(k_o+1) &= \mathbf{\Phi}_{aug}\delta\mathbf{x}(k_o) + \mathbf{\Gamma}_{aug}\Delta\mathbf{v}(k_o) \\ \delta\mathbf{y}(k_o) &= \mathbf{H}_{aug}\delta\mathbf{x}(k_o) \end{aligned} \tag{4.22}$$

where

$$\boldsymbol{\Gamma}_{aug} = \boldsymbol{\Phi}_{aug}\boldsymbol{B}_{aug} = \begin{bmatrix} \mathbf{B}_2 T_o \\ \mathbf{B}_2 \\ \mathbf{0}_{3\times 3} \end{bmatrix} \tag{4.23}$$

A discrete linear observer is created next as:

$$\begin{aligned} \delta\hat{\mathbf{x}}(k_o+1) &= \boldsymbol{\Phi}_{aug}\delta\hat{\mathbf{x}}(k_o) + \boldsymbol{\Gamma}_{aug}\Delta\mathbf{v}(k_o) + \mathbf{L}_p(\delta\mathbf{y}(k_o) - \delta\hat{\mathbf{y}}(k_o)) \\ \delta\hat{\mathbf{y}}(k_o) &= \mathbf{H}_{aug}\delta\hat{\mathbf{x}}(k_o) \end{aligned} \tag{4.24}$$

Note that Equation (4.24) represents the predictive discrete ESO because it uses the current estimation error $\delta\mathbf{y}(k_o) - \delta\hat{\mathbf{y}}(k_o)$ to predict the next estimation $\delta\hat{\mathbf{x}}(k_o+1)$. However, to move from the predictive to the current discrete ESO, the predictive estimation gain, $\mathbf{L}_p$, is defined as:

$$\mathbf{L}_p = \boldsymbol{\Phi}_{aug}\mathbf{L}_c \tag{4.25}$$

where $\mathbf{L}_c$ is the current estimation gain. Substituting Equation (4.25) in Equation (4.24), the state estimation is reduced to:

$$\delta\hat{\mathbf{x}}(k_o+1) = \boldsymbol{\Phi}_{aug}\delta\overline{\mathbf{x}}(k_o) + \boldsymbol{\Gamma}_{aug}\Delta\mathbf{v}(k_o) \tag{4.26}$$

where the new state, $\overline{\mathbf{x}}(k_o)$, acquires less time delay as it includes a current time step update and is given as:

$$\delta\overline{\mathbf{x}}(k_o) = \delta\hat{\mathbf{x}}(k_o) + \mathbf{L}_c(\delta\mathbf{y}(k_o) - \delta\hat{\mathbf{y}}(k_o)) \tag{4.27}$$

Rewriting the estimator to output the new state, the current DLESO is obtained as:

$$\begin{aligned} \delta\hat{\mathbf{x}}(k_o+1) &= \big(\boldsymbol{\Phi}_{aug} - \mathbf{L}_p\mathbf{H}_{aug}\big)\delta\hat{\mathbf{x}}(k_o) + \big[\boldsymbol{\Gamma}_{aug}, \mathbf{L}_p\big]\delta\mathbf{u}_d(k_o) \\ \delta\mathbf{y}_d(k_o) &= \big(\mathbf{I}_{9\times 9} - \mathbf{L}_c\mathbf{H}_{aug}\big)\delta\hat{\mathbf{x}}(k_o) + \big[\mathbf{0}_{9\times 3}, \mathbf{L}_c\big]\delta\mathbf{u}_d(k_o) \end{aligned} \tag{4.28}$$

where $\delta\mathbf{u}_d(k_o) = \big[\Delta\mathbf{v}(k_o), \delta\mathbf{y}(k_o)\big]^T$ is the combined observer input, while $\delta\mathbf{y}_d(k_o)$ is the combined output. For simplification, the current estimation gain is designed using a parameterization-based tuning method [108], which relates the design of the observer to a single variable that is the frequency. In order to select the frequency of the observer, the controller frequency is first analysed by finding the location of the closed-loop poles of Equation (4.8), which is the solution of the following characteristic equation:

$$\boldsymbol{\lambda}(s) = \big|s\mathbf{I}_{6\times 6} - \big(\mathbf{A} - \mathbf{B}\mathbf{K}\big)\big| \tag{4.29}$$

The solution of Equation (4.29), propagated over one orbital period, yields a frequency range for each of the closed-loop poles of the DLQR. The frequency of the observer is then computed, similar to [108], as:

$$\omega_o = 10 \times (\omega_c)_{max} \tag{4.30}$$

where $(\omega_c)_{max} = 5\ [Hz]$ is the maximum frequency of the closed-loop poles of the DLQR, which was computed for the reference elliptic halo orbit shown Figure 3.4. Moreover, for simplicity, the observer is designed using pole placement method by placing all the poles in a single location that corresponds to ω_o. Moving to the discrete domain, the discrete poles are found using the following equation:

$$\beta = e^{-\omega_o T_o} \tag{4.31}$$

The poles are then placed in a single location using the closed-loop characteristic equation of the DLESO as:

$$\boldsymbol{\lambda}(z) = \left| z\mathbf{I}_{9\times 9} - \left(\boldsymbol{\Phi}_{aug} - \boldsymbol{\Phi}_{aug}\mathbf{L}_c\mathbf{H}\right)\right| = (z-\beta)^9 \tag{4.32}$$

Substituting Equations (4.21) and (4.31) in Equation (4.32) yields:

$$\mathbf{L}_c = \begin{bmatrix} \mathbf{I}_{3\times 3}(1-\beta^3) \\ \mathbf{I}_{3\times 3}(1-\beta)^2(1+\beta)\frac{3}{2T_o} \\ \mathbf{I}_{3\times 3}(1-\beta)^3\frac{1}{T_o^2} \end{bmatrix} \tag{4.33}$$

Note that the sampling time of the observer, T_o, must be much smaller than the sampling time of the DLQR, T_c, to insure the stability of the observer and its estimation ability [107]. The sampling time of the observer can then be computed as:

$$T_o = \frac{T_c}{\alpha_o} \tag{4.34}$$

where α_o is the DLQR-DLESO sampling ratio, which was selected experimentally, and is given in Table 4.4 alongside the frequency of the DLESO.

Table 4.4: DLESO tuning parameters.

Parameter	Value
α_o	200
$\omega_o\ [Hz]$	50

4.6 Discrete Active Disturbance Rejection Control

Active disturbance rejection control (ADRC) was originally introduced as an alternative to the proportional-integral-derivative (PID) controller [109]. The success of the ADRC comes from being error-driven, rather than model-based, control law [109]. The application of the ADRC into the station-keeping problem has already been investigated in the literature using continuous linear ESO [73] and continuous/discrete nonlinear ESOs [72]. In this research, however, a novel discrete ADRC (DADRC) is investigated adopting the DLESO designed in Section 4.5. The presented approach offers discrete-time disturbance rejection and is suitable for digital implementation and impulsive control. This allows enhancing the robustness of the DLQR against uncertainties and disturbances. The maneuver calculation using the DADRC is introduced by extending the maneuver, calculated by the DLQR, with a disturbance term, estimated by the DLESO, as:

$$\Delta\mathbf{v}(k_c) = -\mathbf{K}(k_c)\delta\mathbf{x}(k_c) - T_o\hat{\mathbf{f}}(k_o)|_{k_o=k_c} \tag{4.35}$$

where $\mathbf{K}(k_c)$ and $\delta\mathbf{x}(k_c)$ are the DLQR gain matrix and the position deviation computed at the iteration time step, k_c, shown in Equations (4.11) and (4.12). Meanwhile, $\hat{\mathbf{f}}(k_o)|_{k_o=k_c}$ is the disturbance estimated by the DLESO in Equation (4.28), substituted when the iteration time steps of the DLQR and the DLESO are equal. Having different iteration time steps is logical as both controllers were designed considering different sampling times as expressed through Equation (4.34). Since the finite-horizon DLQR was designed considering the optimal number of maneuvers-per-orbit, as shown through Equation (4.3), the maneuver calculation and execution, $\Delta\mathbf{v}(k_c)$, is primarily related to the sampling time of the DLQR. Therefore, the disturbance estimated by the DLESO is going to be compensated only when a maneuver is applied ($k_o = k_c$).

It is worthy to mention that the disturbance in Equation (4.35) is multiplied by the sampling time of the DLESO, T_o, to allow the calculated impulse (velocity) to compensate the estimated disturbance (acceleration). Moreover, by substituting Equation (4.35) in Equation (4.28), it is noticed that the disturbance term is completely eliminated for the estimation of $\delta\dot{\hat{\mathbf{y}}}$. Meanwhile, a residual of $-(T_o^2/2)\hat{\mathbf{d}}$ remains in the estimation of $\delta\hat{\mathbf{y}}$, which is mainly due to the impulsive control implementation as seen in Equations (4.19) through (4.23). However, it will be shown in Chapter 5 that this residual does not affect neither the functionality nor the accuracy of the proposed control approach and can be neglected.

Chapter 5

Simulation and Results

In this sections, the algorithms developed in Chapter 4 are implemented for station-keeping the elliptic halo orbit computed in Chapter 3. The simulation model is first introduced to describe the environment and the maneuver execution process. Several station-keeping scenarios are then investigated for assessing the functionality and performances of both the DLQR and the DADRC against various situations. A Monte-Carlo simulation is finally established for a qualitative examination of both controllers against station-keeping errors.

5.1 Simulation Model

The mathematical model of the ER3BP developed in Chapter 2 was adopted to simulate the motion of the spacecraft in the vicinity of the Earth-Moon L_2 libration point. In general, higher fidelity models, such as the N-body system, are preferred for more accurate simulation results. However, for this research, the ER3BP, supported by the SRP effect and station-keeping errors and constraints, provided a sufficient environment for testing the efficiency of the developed control approach. Therefore, the equations of motion in Equation (2.49) are employed with the non-dimensional units of the pulsating-rotating frame as summarized in Table 5.1. Moreover, the initial conditions in Equation (3.35) were adopted as summarized in Table 5.2 alongside the starting and ending epochs.

5.1.1 Maneuver Implementation

Once a maneuver is calculated using Equation (4.12) or Equation (4.35), the spacecraft is then required to provide this velocity increment using the propulsion system introduced in Section 2.5. However, the maneuver is only

Table 5.1: Non-dimensional units expressed in the pulsating-rotating frame.

Unit	Value
Time Unit (TU) $[sec]$	3.743077×10^5
Position Unit (PU) $[km]$	$3.838000 \times \rho \times 10^5$
Velocity Unit (VU) $[km/sec]$	$1.025359 \times \rho \times 10^0$
Acceleration Unit (AccU) $[km/sec^2]$	$2.739349 \times \rho \times 10^{-6}$

Table 5.2: Simulation boundary conditions.

Parameter	Value
$\mathbf{x}_0$	$\begin{bmatrix} 1.14520421356342 \\ 0 \\ 0.160866058153171 \\ 0 \\ -0.220906655170176 \\ 0 \end{bmatrix}$
Start Epoch	01/01/2030
End Epoch	01/01/2031

applied when all station-keeping constraints are satisfied as introduced in Section 4.2. Furthermore, since the station-keeping maneuver is going to be performed by a single thruster, the maneuver will only be executed after a wait time, t_{wait}. This wait time allows the attitude determination and control subsystem (ADCS) to perform the slewing maneuver required to reorient the thruster with the desired maneuver direction, which is the unit vector of the calculated impulse. In this investigation, a large value for the wait time was considered, $15[min]$, to cover for unaccounted requirements and add more flexibility to the ADCS design, e.g. choosing smaller reaction wheels. After the thruster is oriented along the desired direction, it is then switched on for an operational time as given in Equation (2.48).

5.2 Control System Architecture

The block diagram of the control approach developed in Chapter 4 is expressed here for both the DLQR and the DADRC.

5.2.1 DLQR Architecture

Incorporating the simulation model with the DLQR designed in Section 4.4, the final control system architecture is shown in Figure 5.1.

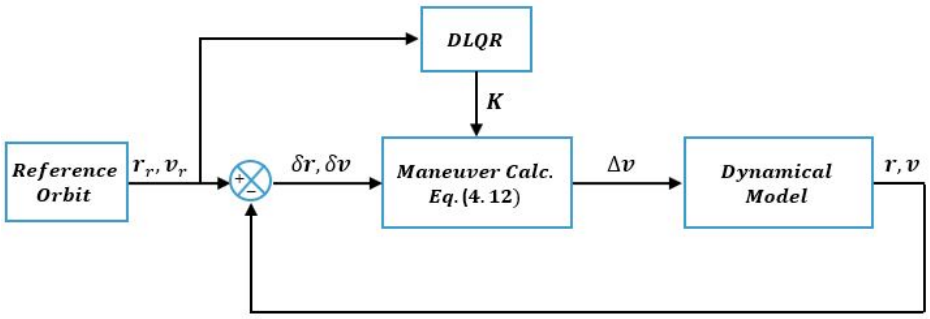

Figure 5.1: DLQR control system architecture.

5.2.2 DADRC Architecture

Incorporating the simulation model with the DADRC designed in Section 4.6, the final control system architecture is shown in Figure 5.2. Note how the combination of both the DLQR and the DLESO forms DADRC.

5.3 Station-Keeping with SRP

In this section, the control approach is tested under the presence of SRP disturbance, without considering the station-keeping errors. This simulation allows verifying the functionality of the DLESO in capturing the added SRP disturbance.

5.3.1 DLQR Results

Running simulation for a mission duration of one year, the controlled orbit is obtained as shown in Figure 5.3. The orbit in Figure 5.3 was obtained at a cost of 15.5607 $[m/sec/year]$ performed over 147 maneuvers distributed as shown in Figure 5.4. Meanwhile, the position deviation from the reference orbit is shown in Figure 5.5, where the deviation is following an oscillation pattern inherited from the sole effect of the SRP disturbance.

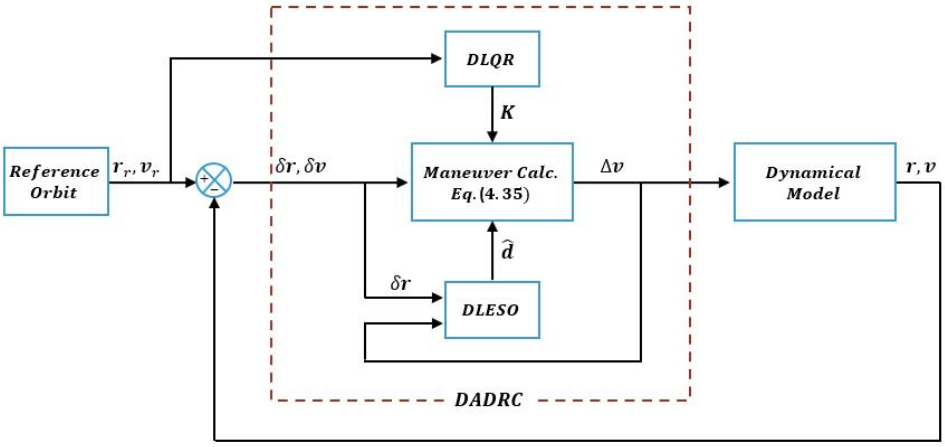

Figure 5.2: DADRC control system architecture.

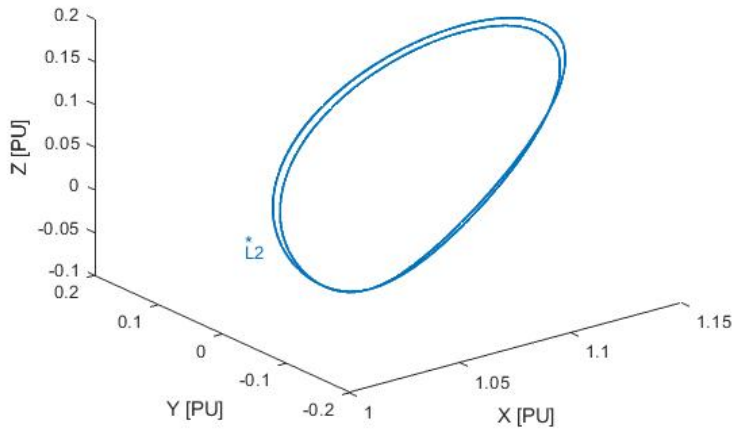

Figure 5.3: Controlled halo orbit using DLQR under the presence of SRP.

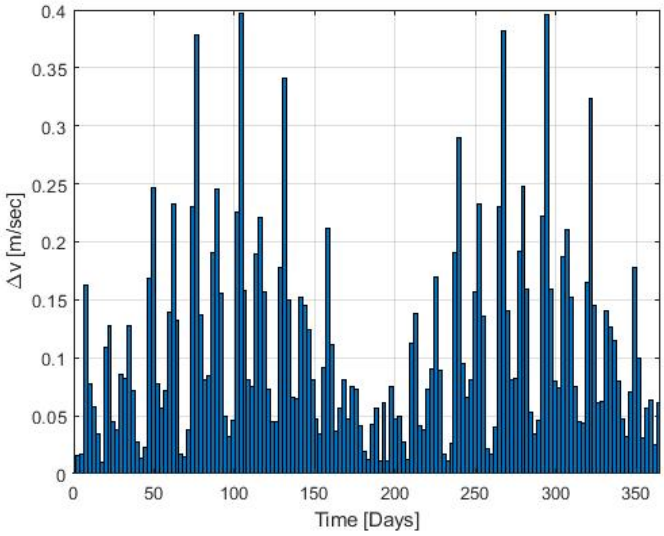

Figure 5.4: Maneuvers distribution using DLQR under the presence of SRP.

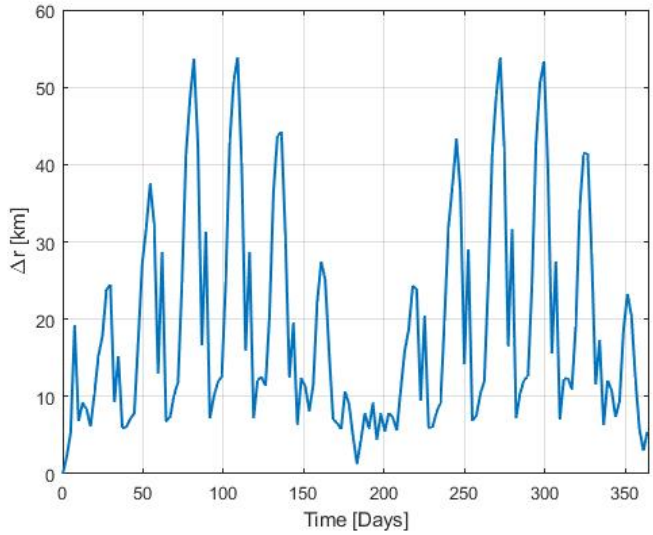

Figure 5.5: Position deviation using DLQR under the presence of SRP.

5.3.2 DADRC Results

Running simulation for a mission duration of one year, the controlled orbit is obtained as shown in Figure 5.6. The orbit in Figure 5.6 was obtained at

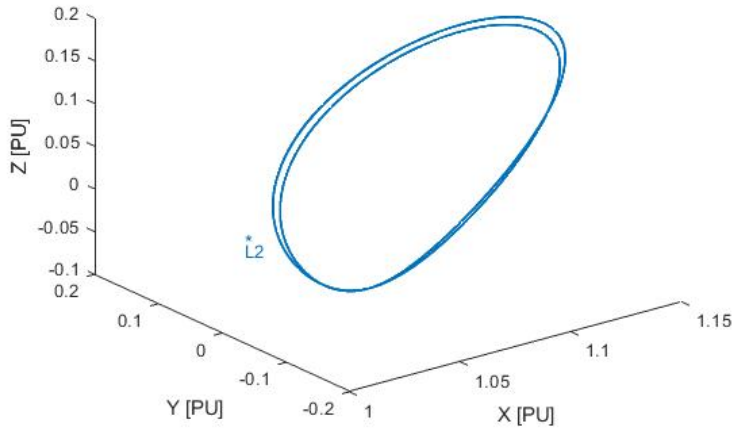

Figure 5.6: Controlled halo orbit using DADRC under the presence of SRP.

a cost of 10.9111 $[m/sec/year]$ performed over 147 maneuvers with the time distribution shown in Figure 5.7. Meanwhile, the real position deviation from the reference orbit is shown in Figure 5.8. Note that comparing with Figure 5.5, the position deviation maintain the same oscillation pattern at a less magnitude. This behaviour is mainly due to the fact that the estimated disturbance is only being compensated when the station-keeping constrains are met, as discussed in Subsection 5.1.1. Comparing Figures 5.4 and 5.5 with Figures 5.7 and 5.8, it is noticed that by adding the DLESO, both the cost and position deviation are decreased with respect to the DLQR controller. This fact comes from the ability of the DLESO to compensate for the external disturbances, represented by the SRP, as shown in Figure 5.9. An important note, looking at both Figure 2.5 and Figure 5.9, it is obvious that the pattern of all the components of the SRP disturbance are captured by the observer. However, while the magnitude of the SRP disturbance lies within the order of 10^{-7} $[m/sec^2]$, the magnitude of the observed disturbance lies within the order of 10^{-5} $[m/sec^2]$. This difference comes from the fact that the DLESO is not only estimating the external disturbances but also both the instabilities inherited from the reference solution and the nonlinearities associated with the use of a linear observer. Furthermore, the

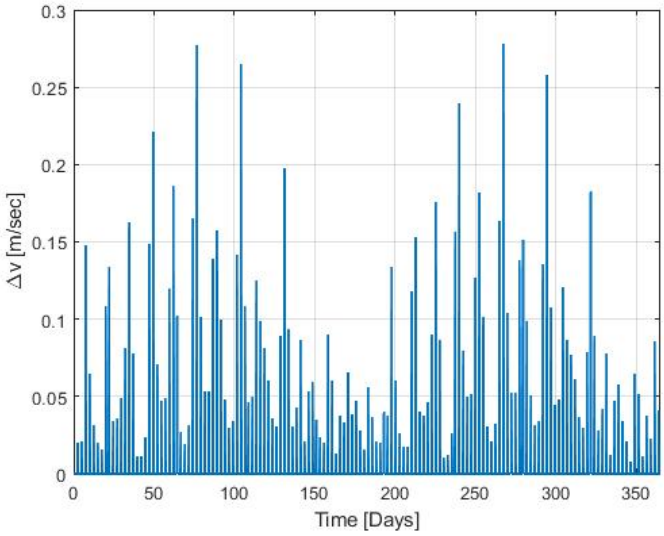

Figure 5.7: Maneuvers distribution using DADRC under the presence of SRP.

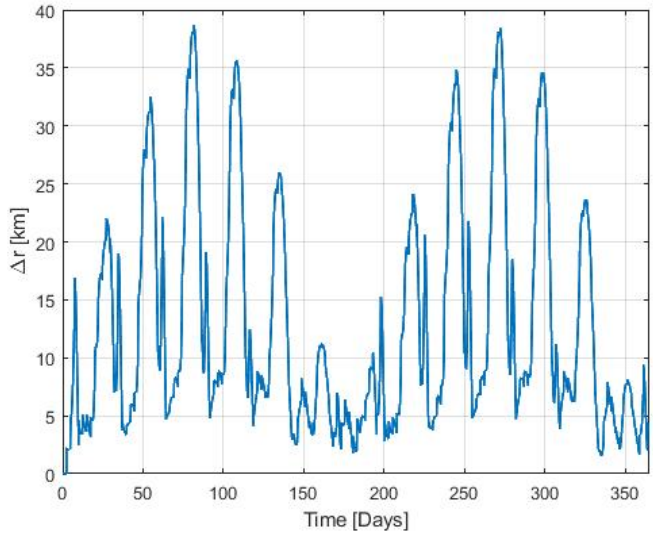

Figure 5.8: Position deviation using DADRC under the presence of SRP.

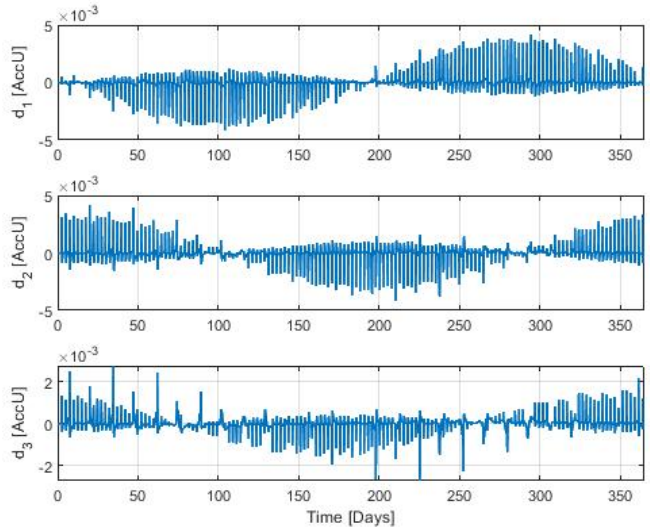

Figure 5.9: Disturbances observed using DLESO under the presence of SRP.

performance of the DLESO is assessed by computing the estimation error of both the position and the velocity deviations. As shown in Figures 5.10 and 5.11, the position estimation error corresponds to an accuracy lies within $[-2, 2]$ $[km]$, meanwhile, the velocity estimation error corresponds to an accuracy lies within $[-0.2, 0.2]$ $[m/sec]$. Considering the presented dynamics and station-keeping constraints, these ranges were considered to offer an acceptable range of accuracy. Moreover, considering the discussion in Section 4.6 regarding the residual in the estimation of the position deviation, an accuracy wthin $[-2, 2]$ $[km]$, under the presence of the SRP disturbance, reflects the fact that this residual can be neglected. Additionally, since the DADRC managed to reduce both the cost and the position deviations comparing to the DLQR, the residual does not affect the functionality of the proposed control.

Finally, a summary of the main station-keeping results under the presence of the SRP disturbance for both the DLQR and the DADRC is listed in Table 5.3.

Table 5.3: Results summary of station-keeping with SRP per one year.

Controller	Δv_{tot} $[m/sec]$	Δr_{max} $[km]$
DLQR	15.5607	53.879
DADRC	10.9111	38.6502

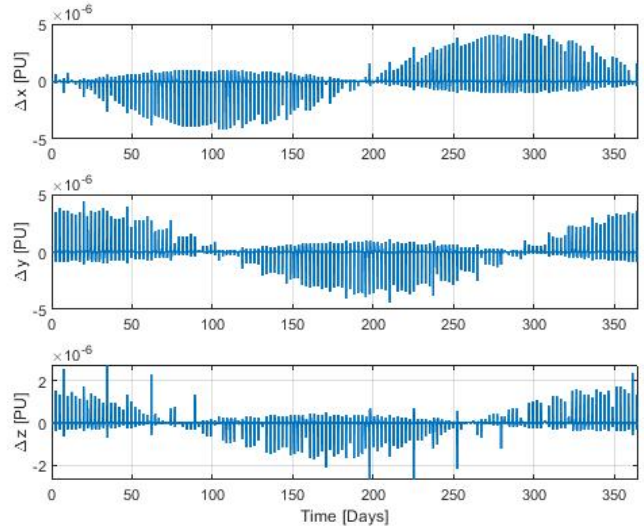

Figure 5.10: Position observation error of the DLESO under the presence of SRP.

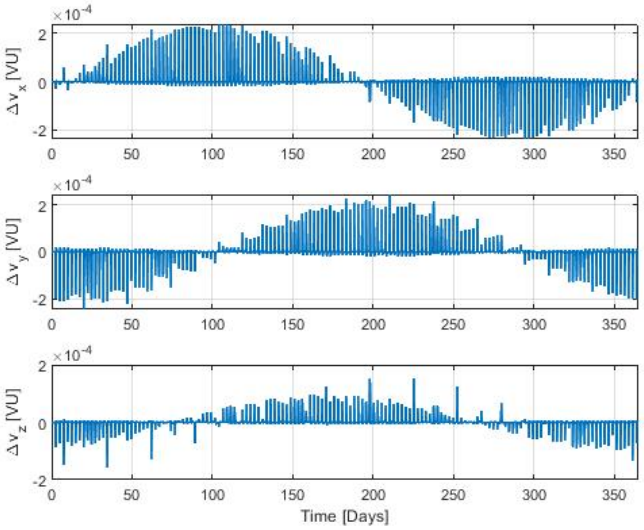

Figure 5.11: Velocity observation error of the DLESO under the presence of SRP.

5.4 Station-Keeping with Errors

In this section, the control approach is tested under the presence of station-keeping errors, without the SRP effect. This simulation allows to verify the functionality of the DLESO in adding robustness and enhancing the performance of the DLQR against the sole effect of station-keeping errors. For this purpose, random errors were considered with normal distributions of zero mean and standard deviations as shown in Table 5.4.

Table 5.4: Standard deviations of the station-keeping errors used in the station-keeping scenarios.

Error	Parameter	Value
Injection	$\sigma_{\lvert r\rvert}$ $[km]$	5
	$\sigma_{\lvert v\rvert}$ $[mm/sec]$	10
Tracking	$\sigma_{\lvert r\rvert}$ $[km]$	5
	$\sigma_{\lvert v\rvert}$ $[mm/sec]$	10
Maneuver	$\sigma_{\lvert \Delta \mathbf{v}\rvert}$ [%]	2

Using the values in Table 5.4, the injection error is generated randomly along the state components as shown in Table 5.5. Meanwhile, the tracking

Table 5.5: Random injection error components used in the station-keeping scenarios.

Parameter		Value
Position $[km]$	Δx	1.2512
	Δy	0.1754
	Δz	1.2616
	$\lvert r\rvert$	1.7855
Velocity $[mm/sec]$	$\Delta \dot{x}$	0.3368
	$\Delta \dot{y}$	0.9618
	$\Delta \dot{z}$	1.8888
	$\lvert v\rvert$	2.1462

and maneuver errors were generated randomly for the entire mission duration to be applied at the tracking and maneuver intervals, respectively, as shown in Figures 5.12 and 5.13.

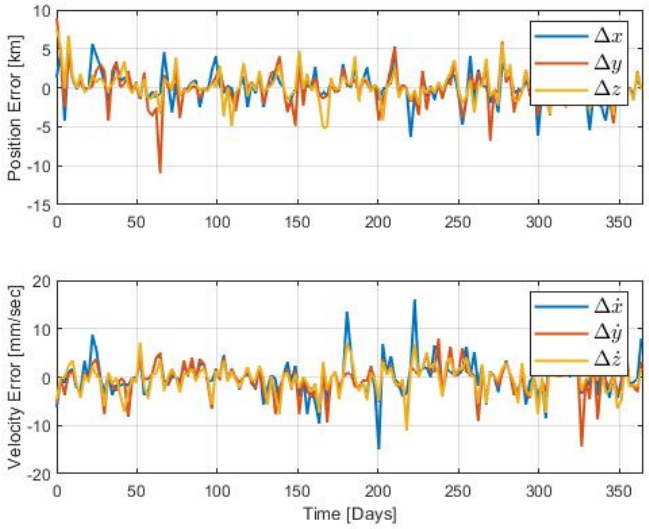

Figure 5.12: Random tracking error components used in the station-keeping scenarios.

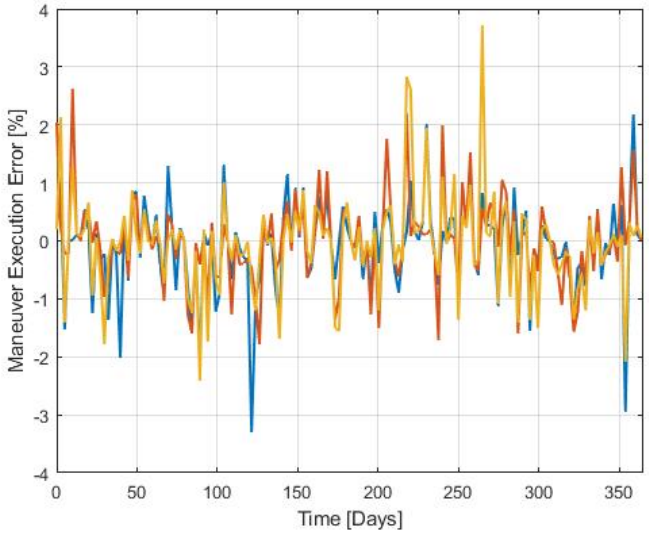

Figure 5.13: Random maneuver execution error components used in the station-keeping scenarios.

5.4.1 DLQR Results

Running simulation for a mission duration of one year, the controlled orbit is obtained as shown in Figure 5.14. The orbit in Figure 5.14 was obtained

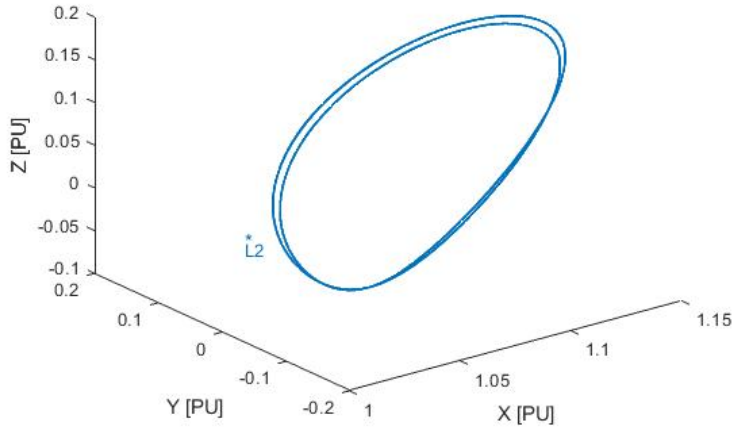

Figure 5.14: Controlled halo orbit using DLQR under the presence of station-keeping errors.

at a cost of 12.2968 $[m/sec/year]$ performed over 148 maneuvers distributed as shown in Figure 5.15. Note that comparing with Figure 5.4, the calculated impulse follows a random behaviour that is inherited from the random tracking and maneuver errors shown in Figures 5.12 and 5.13. Meanwhile, the position deviation is shown in Figure 5.16, which comparing with Figure 5.5, it is noticed that the oscillation pattern due to the SRP is no longer existed. Moreover, the position deviation in Figure 5.16 also reflects a random behaviour that is inherited from the applied random tracking and maneuver errors.

5.4.2 DADRC Results

Running simulation for a mission duration of one year, the controlled orbit is obtained as shown in Figure 5.17. The orbit in Figure 5.17 was obtained at a cost of 10.6426 $[m/sec/year]$ performed over 148 maneuvers with the time distribution shown in Figure 5.18. Comparing with Figure 5.15, the cost is only decreased in magnitude, while the pattern is kept the same. Moreover, the real position deviation shown in Figure 5.19 inherits the same pattern shown in Figure 5.16 at a less magnitude. This behaviour, for both the cost

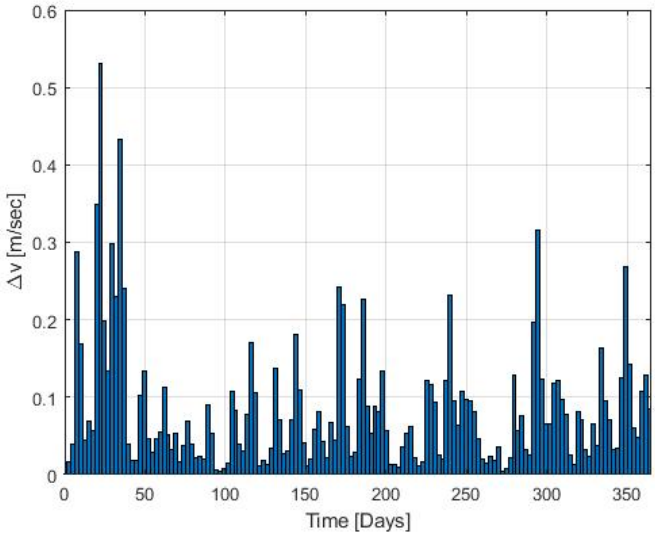

Figure 5.15: Maneuvers distribution using DLQR under the presence of station-keeping errors.

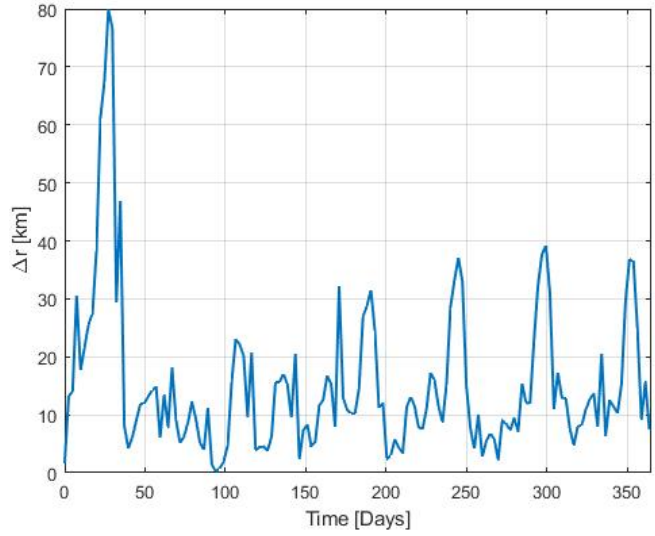

Figure 5.16: Position deviation using DLQR under the presence of station-keeping errors.

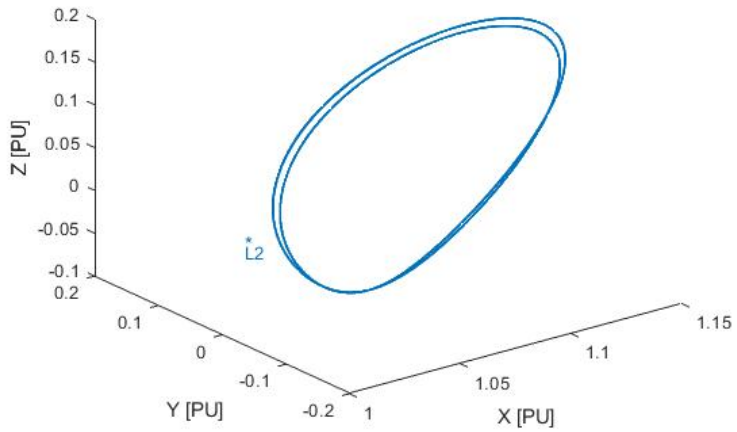

Figure 5.17: Controlled halo orbit using DADRC under the presence of station-keeping errors.

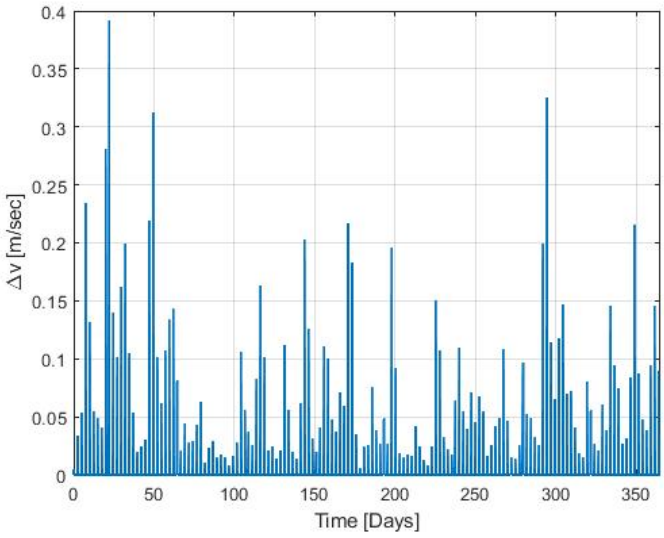

Figure 5.18: Maneuvers distribution using DADRC under the presence of station-keeping errors.

and the position deviation, is mainly due to the fact that the same set of random tracking and maneuver errors is applied for both the DLQR and the DADRC. In turn, this illustrates how that DADRC compensates for the estimated disturbance without changing the dynamics of the DLQR. In other words, the DADRC is adding robustness to the system by compensating for the errors and instabilities as shown in Figure 5.20. The performance of

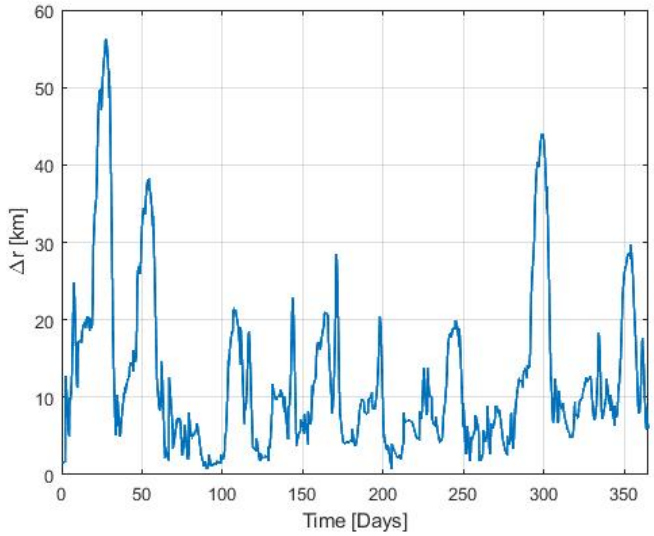

Figure 5.19: Position deviation using DADRC under the presence of station-keeping errors.

the DLESO is then assessed by computing the estimation errors of both the position and the velocity deviations. As shown in Figures 5.21 and 5.22, the position estimation error corresponds to an accuracy lies within $[-4, 4]$ $[km]$, meanwhile, the velocity estimation error corresponds to an accuracy lies within $[-1, 1]$ $[m/sec]$. These values present an acceptable ranges of accuracy considering the presented dynamics, the station-keeping constraints, and the station-keeping errors, especially the tracking error, which represents a measurement noise rather than a disturbance. Therefore, the results reflects the robustness of the control approach not only against disturbances but also measurement noises.

Finally, a summary of the main station-keeping results under the presence of the station-keeping errors for both the DLQR and the DADRC is listed in Table 5.6.

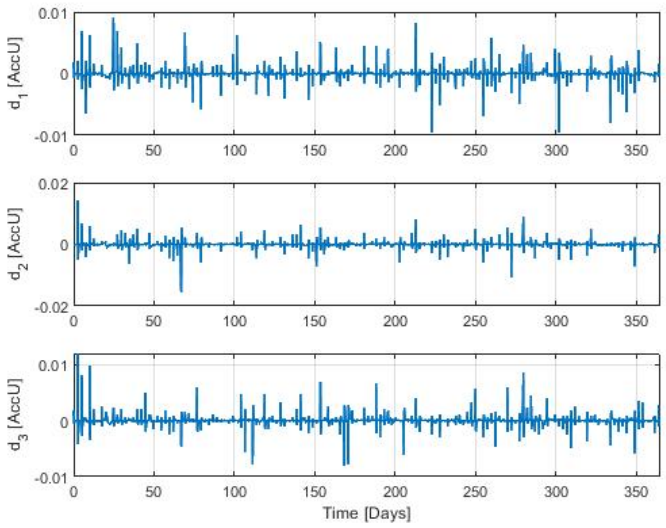

Figure 5.20: Disturbances observed using DLESO under the presence of station-keeping errors.

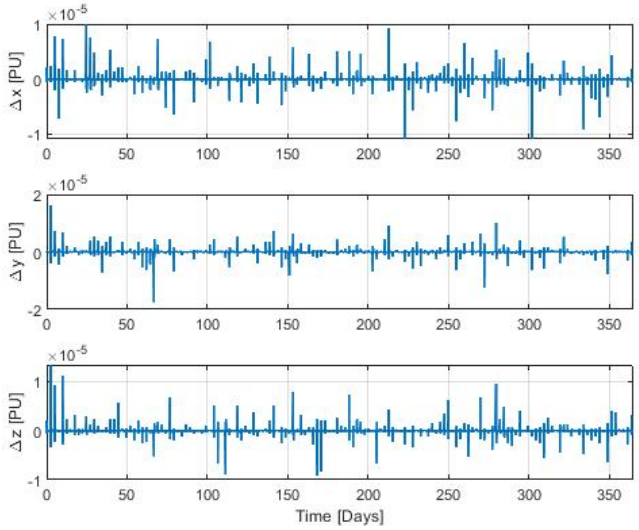

Figure 5.21: Position observation error of the DLESO under the presence of station-keeping errors.

Table 5.6: Results summary of station-keeping with errors per one year.

Controller	Δv_{tot} $[m/sec]$	Δr_{max} $[km]$
DLQR	12.2968	79.8917
DADRC	10.6426	56.216

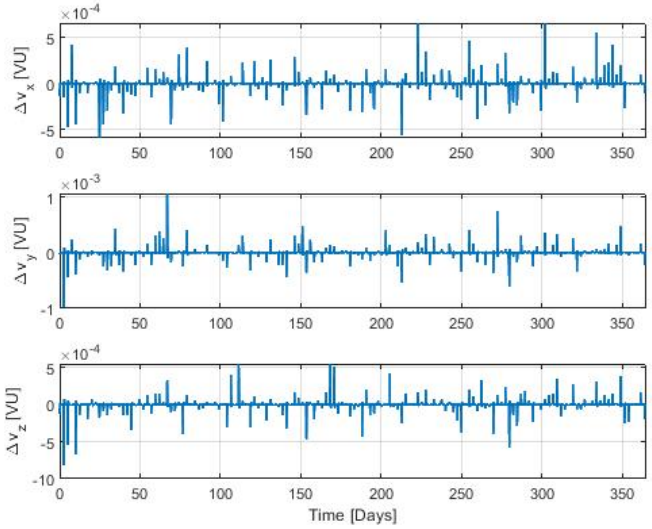

Figure 5.22: Velocity observation error of the DLESO under the presence of station-keeping errors.

5.5 Station-Keeping with SRP and Errors

In this section, the control approach is tested under the presence of both the SRP disturbance and the station-keeping errors. This simulation allows verifying the functionality of the DLESO in a real-like situation.

5.5.1 DLQR Results

Running simulation for a mission duration of one year, the controlled orbit is obtained as shown in Figure 5.23. The orbit in Figure 5.23 was obtained at a cost of 21.0148 $[m/sec/year]$ performed over 148 maneuvers distributed as shown in Figure 5.24. As noticed, the maneuver distribution follows a combined pattern of the maneuvers in Figures 5.4 and 5.15. Moreover, it is noticed that the position deviation, shown in Figure 5.25, also inherits the dynamics of both Figures 5.5 and 5.16. This behaviour, for both the maneuver distribution and the position deviation, could be explained by the presence of both the SRP disturbance and the station-keeping errors. In turn, this reflects the accuracy of the model and its implementation.

5.5.2 DADRC Results

Running simulation for a mission duration of one year, the controlled orbit is obtained as shown in Figure 5.26. The orbit in Figure 5.26 was obtained at

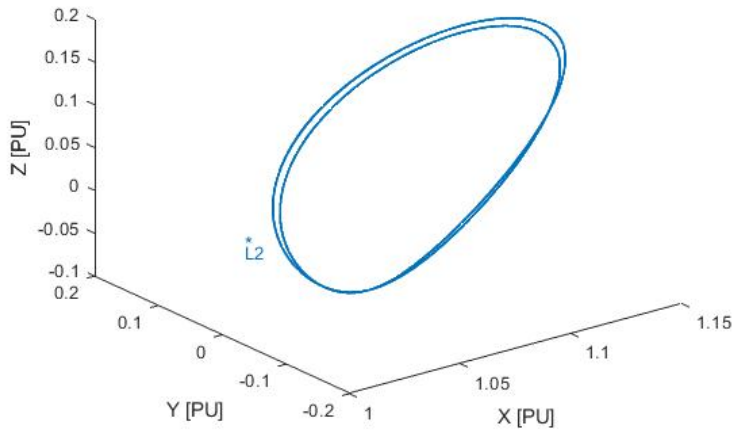

Figure 5.23: Controlled halo orbit using DLQR under the presence of SRP and station-keeping errors.

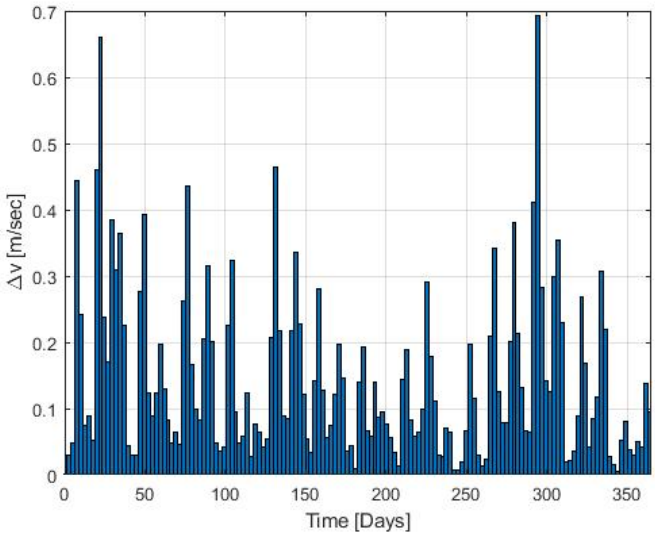

Figure 5.24: Maneuvers distribution using DLQR under the presence of SRP and station-keeping errors.

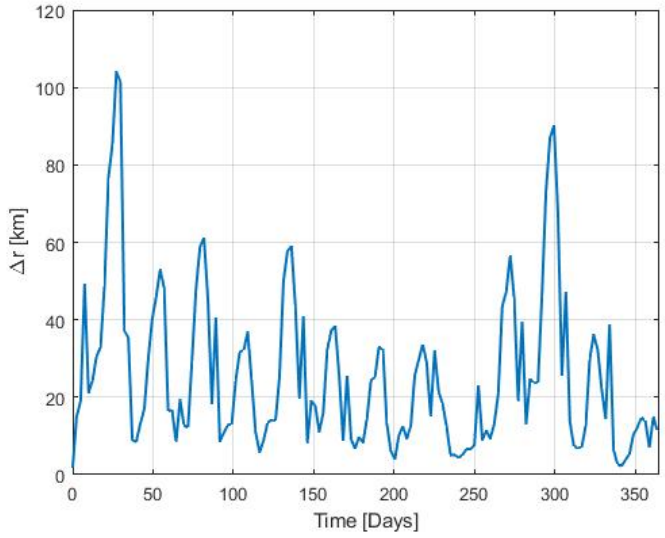

Figure 5.25: Position deviation using DLQR under the presence of SRP and station-keeping errors.

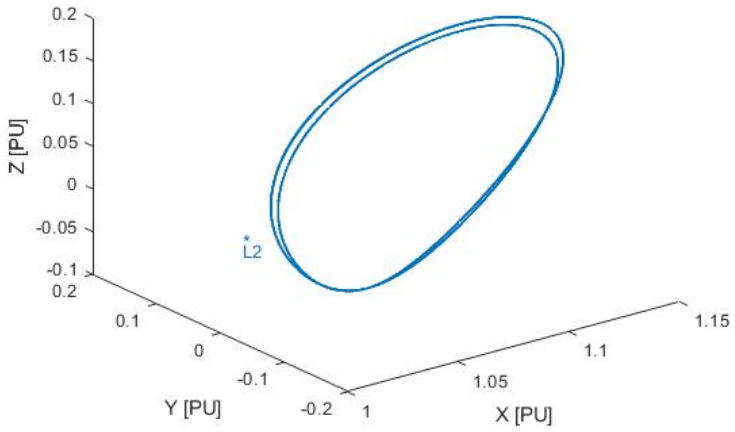

Figure 5.26: Controlled halo orbit using DADRC under the presence of SRP and station-keeping errors.

a cost of 16.3082 $[m/sec/year]$ performed over 147 maneuvers with the time distribution shown in Figure 5.27. Meanwhile, the real position deviation is

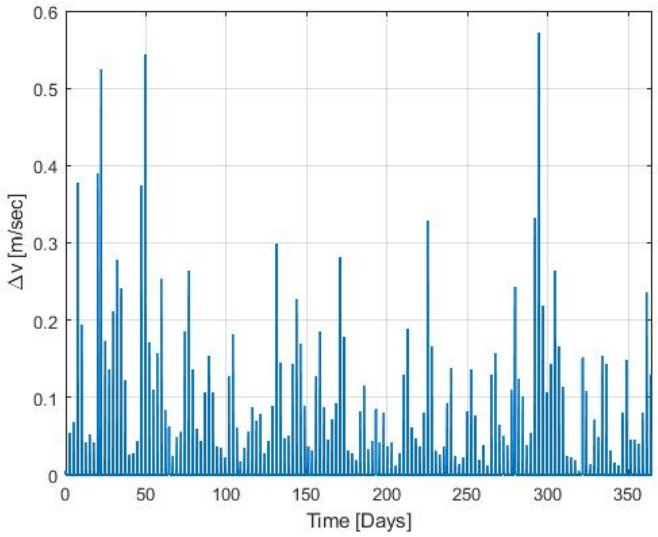

Figure 5.27: Maneuvers distribution using DADRC under the presence of SRP and station-keeping errors.

shown in Figure 5.28. Comparing Figures 5.24 and 5.25 with Figures 5.27 and 5.28, it is noticed that by adding the DLESO, both the cost and position deviation are decreased. This fact comes from the ability of the DLESO to compensate for the external disturbances, instabilities, and measurement noises, as shown in Figure 5.29. The performance of the DLESO is then assessed by computing the estimation errors of the position and the velocity deviations. As shown in Figures 5.30 and 5.31, the position estimation error corresponds to an accuracy lies within $[-7.5, 7.5]$ $[km]$, meanwhile, the velocity estimation error corresponds to an accuracy lies within $[-1, 1]$ $[m/sec]$. Note that the DLESO offers a lower accuracy to the position deviation estimation comparing with the velocity deviation. This behavior is mainly due to the residual left in the estimation of the position deviation as discussed in section 4.6. However, since the DLESO is only used for disturbance estimation and considering the acquired results, the residual does not affect the functionality of the DADRC. Therefore, these ranges were considered within an acceptable accuracy, especially under the presence of both the SRP disturbance and the station-keeping errors.

Finally, a summary of the main station-keeping results under the presence of both the SRP disturbance and the station-keeping errors is listed in Table 5.7 for both the DLQR and the DADRC.

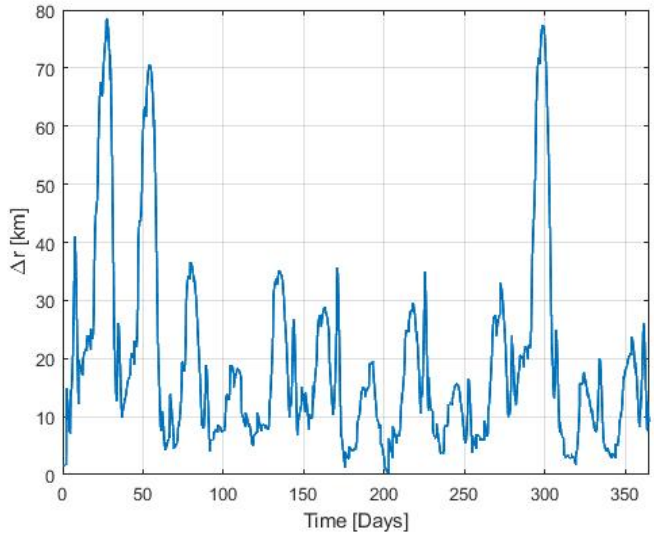

Figure 5.28: Position deviation using DADRC under the presence of SRP and station-keeping errors.

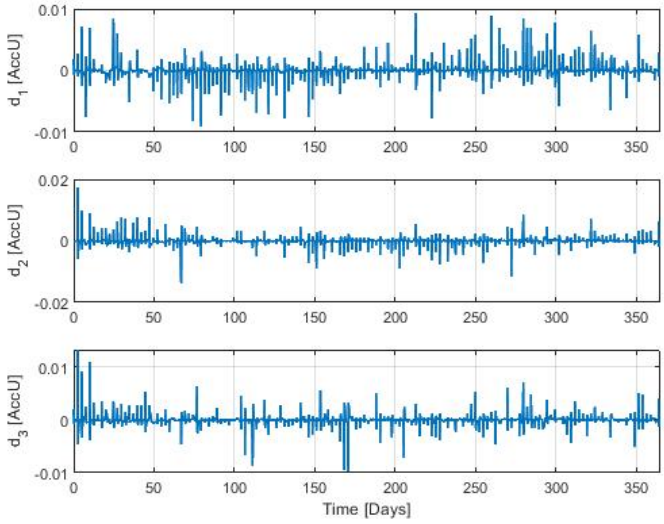

Figure 5.29: Disturbances observed using DLESO under the presence of SRP and station-keeping errors.

Table 5.7: Results summary of station-keeping with errors per one year.

Controller	Δv_{tot} $[m/sec]$	Δr_{max} $[km]$
DLQR	21.0148	103.9796
DADRC	16.3082	78.4859

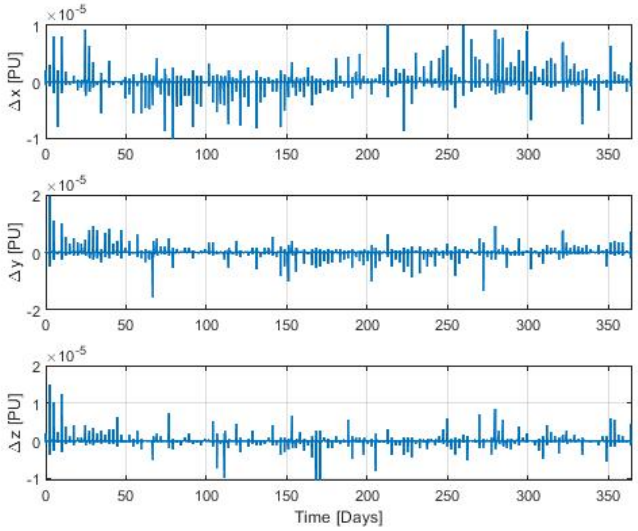

Figure 5.30: Position observation error of the DLESO under the presence of SRP and station-keeping errors.

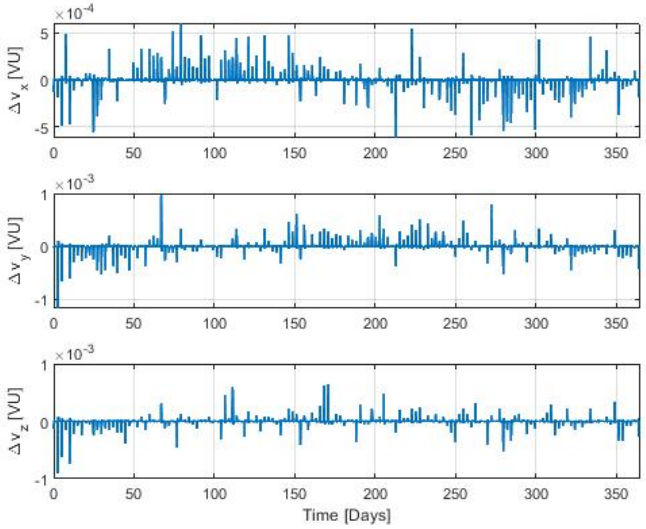

Figure 5.31: Velocity observation error of the DLESO under the presence of SRP and station-keeping errors.

5.6 Monte-Carlo Simulation

In reality, the simulation in Section 5.5 represents only one possibility of the station-keeping errors. Therefore, to estimate the results qualitatively, the standard deviations of the station-keeping errors given in Table 4.2, alongside the SRP disturbance, are used to generate a Monte-Carlo simulation. Accounting the limitation in the computational power, only 1000 random trials were considered for every error distribution shown in Table 4.2. The results of the Monte-Carlo simulation are assessed in terms of the average (Avg.), standard deviation (Std.), maximum (Max), and minimum (Min.) quantities. Moreover, the average and standard deviation were calculated similar to [65] as:

$$\begin{aligned} \overline{q} &= \frac{\sum_{i=0}^{n} q_i}{n} \\ \sigma_q &= \sqrt{\frac{\sum_{i=0}^{n} (q_i - \overline{q})^2}{n-1}} \end{aligned} \tag{5.1}$$

where q is the quantity of interest, n is the total number of trials, $\overline{q}$ is the average, and σ_q is the standard deviation. Meanwhile, the quantities of interest were the total cost, Δv_{tot}, the maximum position deviation, Δr_{max}, the maximum time between two consecutive maneuvers, Δt_{max}, and the number of maneuvers, $N_{\Delta \mathbf{v}}$.

5.6.1 DLQR Results

The Monte-Carlo simulation results for the DLQR over a mission duration of one year are summarized in Table 5.8.

5.6.2 DADRC Results

The Monte-Carlo simulation results for the DADRC over a mission duration of one year are summarized in Table 5.9. Having different error sets allows to evaluate the impact of both the position and the velocity errors individually. As seen from Tables 5.8 and 5.9, increasing the position error, expressed by the difference between Case I and Case II, reflects a higher impact on the performance than increasing the velocity error, expressed by the difference between Case II and Case III. Moreover, the output of the Monte-Carlo simulation illustrates the operational success of the proposed DADRC strategy in increasing the robustness of the DLQR against uncertainties, disturbances, and measurement errors. Hence, achieving the station-keeping at a lower cost and position deviation.

Table 5.8: Monte-Carlo simulation results of the DLQR per one year.

Case	Value	Δv_{tot} $[m/sec]$	Δr_{max} $[km]$	Δt_{max} $[days]$	$N_{\Delta \mathbf{v}}$
I	Max.	17.6194	82.9673	4.9491	148
	Avg.	16.3617	63.1542	4.9343	147.006
	Min.	15.1811	52.3242	2.4745	147
	Std.	0.38037	4.5936	0.1912	0.077266
II	Max.	46.116	339.7812	4.9491	148
	Avg.	27.7644	151.6301	4.8798	147.028
	Min.	15.4582	63.6135	2.4745	147
	Std.	4.2052	40.326	0.4084	0.16506
III	Max.	53.4531	357.3752	4.9491	148
	Avg.	32.3329	166.9776	2.5686	147.962
	Min.	19.8572	69.3658	2.4745	147
	Std.	4.682	42.9747	0.4733	0.19129

Table 5.9: Monte-Carlo simulation results of the DADRC per one year.

Case	Value	Δv_{tot} $[m/sec]$	Δr_{max} $[km]$	Δt_{max} $[days]$	$N_{\Delta \mathbf{v}}$
I	Max.	13.1335	53.906	7.4238	148
	Avg.	12.0017	43.3367	6.4314	146.401
	Min.	10.6615	36.458	2.4746	146
	Std.	0.27927	2.9209	1.2184	0.49238
II	Max.	36.6871	202.8684	7.4238	148
	Avg.	18.6876	105.2993	5.6668	146.71
	Min.	11.1836	36.179	2.4746	146
	Std.	2.9877	25.0809	1.1767	0.47553
III	Max.	41.8932	231.4512	4.9492	148
	Avg.	23.9144	128.343	3.217	147.7
	Min.	15.5334	47.6805	2.4746	147
	Std.	3.21	27.5512	1.1346	0.45849

Chapter 6

Conclusion and Recommendations

6.1 Conclusion

In this investigation, a novel impulsive robust control approach was developed for station-keeping an L_2 elliptic halo orbit in the Earth-Moon system. Using a few tuning parameters, the constructed control strategy has demonstrated its robustness against unmodeled dynamics and disturbances, such as solar radiation pressure and station-keeping errors.

The dynamical model used to describe the motion of the spacecraft in the Earth-Moon system was first derived in the CR3BP as seen in Chapter 2. The eccentricity of the moon was then considered by reformulating the differential equations in the ER3BP as seen from Equation (2.40). The SRP disturbance was later introduced into the dynamics alongside the propulsion system as noticed through Equation (2.49). In Chapter 3, the mathematical models used to compute the reference trajectory around the L_2 libration point are presented. Following the derivation of the variational equation, the STM was formulated for both the CR3BP and the ER3BP. Adopting the single shooting methods, differential correction strategies were then introduced as an effective tool to compute the periodic halo orbit in the CR3BP, shown in Figure 3.3. Meanwhile, multi-segment shooting methods and natural parameter continuation were implemented using nonlinear programming optimization to compute the reference halo orbit in the ER3BP, shown in Figure 3.4. The control methods used to achieve the station-keeping were then introduced in detail in Chapter 4. Finite-horizon DLQR was first designed for optimal maneuver calculations, as shown through Equation (4.12), required to overcome the instabilities inherited in the reference solution. Meanwhile,

disturbance estimation was investigated using a DLESO that was adopted for impulsive maneuvers, as shown through Equation (4.28). The novel DADRC was finally structured in Equation (4.35) by extending the calculated maneuver with a disturbance rejection term.

As stated earlier, the novelty of this control strategy compared to the state of the art ones is its usability in discrete-time and suitability for digital implementation and impulsive thrusters. As shown in Chapter 4, the design of the DADRC was carried using a few tuning parameters; while the sampling time of the DLQR is inherited from the dynamics, as expressed in Equations (4.3) and (4.4), the designer needs only to choose the weight factor, ρ_c; meanwhile, as the frequency of the DLESO was determined using Equation (4.30), the designer needs only to choose the DLQR-DLESO sampling ratio, α_o. In Chapter 5, the proposed control approach was tested in several simulation scenarios under the presence of the SRP disturbance, the station-keeping constraints, and the station-keeping errors. Comparing the DADRC with the DLQR, as seen in Sections 5.3 through 5.5, the DADRC was found to offer an increased robustness against the SRP disturbance and the station-keeping errors. Two Monte-Carlo simulations were also performed for both the DLQR and the DADRC for a qualitative examination of the effect of the random station-keeping errors listed in Table 4.2. Meanwhile, for comparison reasons, the average results of the Monte-Carlo simulation shown in Tables 5.8 and 5.9 are now summarized in Table 6.1.

Table 6.1: Average results obtained from the Monte-Carlo simulations of both the DLQR and the DADRC.

Case	Parameter	DLQR	DADRC
I	Δv_{tot} $[m/sec]$	16.3617	12.0017
	Δr_{max} $[km]$	63.1542	43.3367
	Δt_{max} $[days]$	4.9343	6.4314
	$N_{\Delta \mathbf{v}}$	147.006	146.401
II	Δv_{tot} $[m/sec]$	27.7644	18.6876
	Δr_{max} $[km]$	151.6301	105.2993
	Δt_{max} $[days]$	4.8798	5.6668
	$N_{\Delta \mathbf{v}}$	147.028	146.71
III	Δv_{tot} $[m/sec]$	32.3329	25.5366
	Δr_{max} $[km]$	166.9776	114.026
	Δt_{max} $[days]$	2.5686	3.217
	$N_{\Delta \mathbf{v}}$	147.962	147.7

From Table 6.1, it can be noticed that the addition of the DLESO to the DLQR decreases both the cost and the position deviation by approximately 25 - 35 [%] in all station-keeping scenarios. Moreover, the maximum time between maneuvers increases when using the DADRC, allowing for a longer time dedicated to the scientific mission. Therefore, the DADRC that was suggested and designed during this investigation succeeded in adding robustness and enhancing the performance of the DLQR against external disturbances, uncertainties, and measurement noises.

6.2 Recommendations for Future Work

Following to the development of the DADRC in this investigation, further examination and improvement are suggested as:

- To increase the fidelity of the simulation environment, represented by the dynamical model, this control approach must be investigated in the N-body full ephemeris model. However, when using the full ephemeris model, the nominal orbit must be redesigned considering the new N-body dynamics as done in [22].

- Although a wait time, t_{wait}, was added to compensate for the required slewing maneuver, the control approach can be investigated using a higher fidelity model that incorporates both the orbital and the attitude dynamics. In turn, this increases the accuracy of the maneuver implementation, hence, the station-keeping calculations.

- The overall algorithm can be digitally implemented using a processor in the loop (PiL) simulation. This introduces more preliminary, reliable, and accurate calculations that can be used later in practical implementation with real missions.

This page was intentionally left blank

Bibliography

[1] Robert Farquhar, Daniel Muhonen, and L. Church. "Trajectories and orbital maneuvers for the ISEE-3/ICE comet mission". In: *Astrodynamics Conference*. 1984, p. 1976.

[2] Maksim Shirobokov, Sergey Trofimov, and Mikhail Ovchinnikov. "Survey of station-keeping techniques for libration point orbits". In: *Journal of Guidance, Control, and Dynamics* 40.5 (2017), pp. 1085–1105.

[3] Isaac Newton. *The Principia: mathematical principles of natural philosophy/new translation by I. Bernard Cohen and Anne Whitman assisted by Julia Budenz, preceded by a guide to Newton's" Principia" by I. Bernard Cohen*. Univ of California Press, 1999.

[4] June Barrow-Green. *Poincaré and the three body problem*. Vol. 11. American Mathematical Soc., 1997.

[5] Victor Szebehely. *Theory of Orbits: The Restricted Problem of Three Bodies*. Academic Press, Inc., 1967.

[6] George William Hill. "Researches in the lunar theory". In: *American journal of Mathematics* 1.1 (1878), pp. 5–26.

[7] Henri Poincaré. *"Les" méthodes nouvelles de la mécanique céleste: Invariants intégraux*. Vol. 3. Gauthier-Villars it fils, 1899.

[8] Mark Woodard, David Folta, and Dennis Woodfork. "ARTEMIS: the first mission to the lunar libration orbits". In: *21st International Symposium on Space Flight Dynamics, Toulouse, France*. 2009.

[9] LIU Lei and HU Chunyang. "Scheme design of the CHANG'E-5T1 extended mission". In: *Chinese Journal of Aeronautics* 31.7 (2018), pp. 1559–1567.

[10] Craig E Roberts. "Long term missions at the Sun-Earth Libration Point L1: ACE, SOHO, and WIND". In: (2011).

[11] Martin W Lo et al. "Genesis mission design". In: *The Journal of the astronautical sciences* 49.1 (2001), pp. 169–184.

[12] M Limon et al. *Wilkinson Microwave Anisotropy Probe (WMAP): Explanatory Supplement*. 2003.

[13] Kenshiro Oguri et al. "EQUULEUS mission analysis: Design of the science orbit phase". In: 72. 2017, pp. 1–7.

[14] Stefano Speretta et al. "LUMIO: achieving autonomous operations for Lunar exploration with a CubeSat". In: *2018 SpaceOps Conference*. 2018, p. 2599.

[15] Francesco Topputo et al. "LUMIO: a cubesat at Earth-Moon L2". In: *4S Symposium*. 2018, pp. 1–15.

[16] Francesco Topputo et al. "Lumio: Charazterizing lunar meteoroid impacts with a cubesat". In: *69th International Astronautical Congress (IAC 2018)*. International Astronautical Federation, IAF. 2018, pp. 1–11.

[17] Herbert B Keller. *Numerical solution of two point boundary value problems*. SIAM, 1976.

[18] SM Roberts and JS Shipman. "Continuation in shooting methods for two-point boundary value problems". In: *Journal of Mathematical Analysis and Applications* 18.1 (1967), pp. 45–58.

[19] SM Roberts and JS Shipman. "Justification for the continuation method in two-point boundary value problems". In: *Journal of Mathematical Analysis and Applications* 21.1 (1968), pp. 23–30.

[20] Mike R Osborne. "On shooting methods for boundary value problems". In: *Journal of Mathematical Analysis and Applications* 27.2 (1969), pp. 417–433.

[21] Thomas A Pavlak. "Trajectory Design and Orbit Maintenance Strategies in Multi-Body Dynamical Regimes". PhD thesis. Purdue University, 2013.

[22] Emily M. Zimovan. "Characteristics and Design Strategies for Near Rectilinear Halo Orbits within the Earth-Moon System". MA thesis. Indiana: Purdue University, 2017.

[23] Forest Ray Moulton et al. "Periodic orbits". In: *peor* (1920).

[24] J. Grebow Daniel. "Generating Periodic Orbits in the Circular Restricted Three-Body Problem with Applications to Lunar South Pole Coverage". PhD thesis. Ph.D. thesis, Ms dissertation, Purdue University, West Lafayette, Indiana, 2006.

[25] Wayne R Schlei. "Interactive Spacecraft Trajectory Design Strategies Featuring Poincaré Map Topology". PhD thesis. Purdue University, 2017.

[26] Robert Willard Farquhar. *The control and use of libration-point satellites*. Vol. 346. National Aeronautics and Space Administration, 1970.

[27] Robert W Farquhar and Ahmed A Kamel. "Quasi-periodic orbits about the translunar libration point". In: *Celestial mechanics* 7.4 (1973), pp. 458–473.

[28] John V Breakwell and John V Brown. "The 'halo'family of 3-dimensional periodic orbits in the Earth-Moon restricted 3-body problem". In: *Celestial mechanics* 20.4 (1979), pp. 389–404.

[29] David L Richardson. "Analytic construction of periodic orbits about the collinear points". In: *Celestial mechanics* 22.3 (1980), pp. 241–253.

[30] Kathleen Connor Howell. "Three-dimensional, periodic,'halo'orbits". In: *Celestial mechanics* 32.1 (1984), pp. 53–71.

[31] Kathleen Connor Howell. "Families of orbits in the vicinity of the collinear libration points". In: *The Journal of the Astronautical Sciences* 49.1 (2001), pp. 107–125.

[32] Kathleen C Howell, Brian T Barden, and MARTIN W Lo. "Application of dynamical systems theory to trajectory design for a libration point mission". In: *The Journal of the Astronautical Sciences* 45.2 (1997), pp. 161–178.

[33] Wang Sang Koon et al. "Shoot the Moon, Spaceflight Mechanics". In: *AAS* 105.Part II (2000), pp. 107–1181.

[34] Gerard Gómez et al. "Connecting orbits and invariant manifolds in the spatial restricted three-body problem". In: *Nonlinearity* 17.5 (2004), p. 1571.

[35] Shane D Ross et al. *Dynamical Systems, the Three-Body Problem, and Space Mission Design*. Marsden Books, 2011.

[36] Roger Broucke. "Stability of periodic orbits in the elliptic, restricted three-body problem". In: *AIAA journal* 7.6 (1969), pp. 1003–1009.

[37] TA Heppenheimer. "Out-of-plane motion about libration points: Nonlinearity and eccentricity effects". In: *Celestial mechanics* 7.2 (1973), pp. 177–194.

[38] Simos Ichtiaroglou. "Elliptic Hill's problem: The continuation of periodic orbits". In: *Astronomy and Astrophysics* 92 (1980), pp. 139–141.

[39] Simos Ichtiaroglou and M Michalodimitrakis. "Three-body problem-the existence of families of three-dimensional periodic orbits which bifurcate from planar periodic orbits". In: *Astronomy and Astrophysics* 81 (1980), pp. 30–32.

[40] E Sarris. "Families of symmetric-periodic orbits in the elliptic three-dimensional restricted three-body problem". In: *Astrophysics and space science* 162.1 (1989), pp. 107–122.

[41] Stefano Campagnola, Martin Lo, and Paul Newton. "Subregions of motion and elliptic halo orbits in the elliptic restricted three-body problem". In: (2008).

[42] XY Hou and L Liu. "On motions around the collinear libration points in the elliptic restricted three-body problem". In: *Monthly Notices of the Royal Astronomical Society* 415.4 (2011), pp. 3552–3560.

[43] Pini Gurfil and N Jeremy Kasdin. "Niching genetic algorithms-based characterization of geocentric orbits in the 3D elliptic restricted three-body problem". In: *Computer Methods in Applied Mechanics and Engineering* 191.49-50 (2002), pp. 5683–5706.

[44] Pini Gurfil and Dani Meltzer. "Semi-analytical method for calculating the elliptic restricted three-body problem monodromy matrix". In: *Journal of guidance, control, and dynamics* 30.1 (2007), pp. 266–271.

[45] KI Antoniadou and G Voyatzis. "2/1 resonant periodic orbits in three dimensional planetary systems". In: *Celestial Mechanics and Dynamical Astronomy* 115.2 (2013), pp. 161–184.

[46] Bharat Mahajan and Henry Pernicka. "Halo orbits near small bodies in the elliptic restricted problem". In: *AIAA/AAS Astrodynamics Specialist Conference*. 2012, p. 4876.

[47] Hao Peng and Shijie Xu. "Stability of two groups of multi-revolution elliptic halo orbits in the elliptic restricted three-body problem". In: *Celestial Mechanics and Dynamical Astronomy* 123.3 (2015), pp. 279–303.

[48] Pini Gurfil and Dani Meltzer. "Stationkeeping on unstable orbits: generalization to the elliptic restricted three-body problem". In: *The Journal of the Astronautical Sciences* 54.1 (2006), pp. 29–51.

[49] Morad Nazari, William M Anthony, and Eric Butcher. "Continuous thrust stationkeeping in Earth-Moon L1 halo orbits based on LQR control and Floquet theory". In: *AIAA/AAS Astrodynamics Specialist Conference*. 2014, p. 4140.

[50] TA Heppenheimer. “Optimal about Controls for Out-of-Plane Motion the Translunar Libration Point”. In: *Journal of Spacecraft and Rockets* 7.9 (1970), pp. 1088–1092.

[51] ML Lidov and VA Lyakhova. “The guaranteeing synthesis of control for stabilization of the motion of a space vehicle in the vicinity of unstable libration points”. In: *KosIs* 30.5 (1992), pp. 579–595.

[52] IS Ilyin. “Quasi-periodic orbits around Sun-Earth L_2 libration point and their transfer trajectories in Russian space missions”. In: (2015).

[53] William Wiesel and William Shelton. “Modal control of an unstable periodic orbit”. In: *Journal of the Astronautical Sciences* (1983).

[54] Gerard Gómez et al. “Station keeping of a quasiperiodic halo orbit using invariant manifolds”. In: *Proceed. 2nd Internat. Symp. on spacecraft flight dynamics, Darmstadt*. 1986, pp. 65–70.

[55] Carles Simó et al. “On the optimal station keeping control of halo orbits”. In: *Acta Astronautica* 15.6-7 (1987), pp. 391–397.

[56] A Yu Kogan. “An optimal program of impulse corrections of unstable periodic orbits”. In: *KosIs* 30.5 (1992), pp. 712–714.

[57] Timothy M Keeter. “Station-keeping strategies for libration point orbits: Target point and floquet mode approaches”. MA thesis. Purdue University, 1994.

[58] Gerard Gómez et al. “Station-keeping strategies for translunar libration point orbits”. In: *Advances in Astronautical Sciences* 99.2 (1998), pp. 949–967.

[59] Simone Cravedi. “Orbit maintenance strategy for libration point orbits. Floquet modes approach”. MA thesis. Milan: Politecnico di Milano, 2019.

[60] PY Elyasberg and TA Timokhova. “Control of Spacecraft Motion in Neighborhood of Collinear Libration Center in Restricted Elliptical Three-body Problem”. In: *Kosmicheskie Issledovaniya* 24.4 (1986), pp. 497–512.

[61] JV Breakwell. “Investigation of halo satellite orbit control[Final Report]”. In: (1973).

[62] John V Breakwell, Ahmed A Kamel, and Martin J Ratner. “Station-keeping for a translunar communication station”. In: *Celestial Mechanics* 10.3 (1974), pp. 357–373.

[63] JA Erickson and AB Glass. "Implementation of ISEE-3 trajectory control". In: (1979).

[64] Mehrdad Ghorbani and Nima Assadian. "Optimal station-keeping near Earth–Moon collinear libration points using continuous and impulsive maneuvers". In: *Advances in Space Research* 52.12 (2013), pp. 2067–2079.

[65] Yijun Lian et al. "Station-keeping of real Earth–Moon libration point orbits using discrete-time sliding mode control". In: *Communications in nonlinear science and numerical simulation* 19.10 (2014), pp. 3792–3807.

[66] P Di Giamberardino and S Monaco. "On halo orbits spacecraft stabilization". In: *Acta Astronautica* 38.12 (1996), pp. 903–925.

[67] Yuki Akiyama, Mai Bando, and Shinji Hokamoto. "Station-keeping and formation flying for periodic orbit around Lagrangian points by Fourier series". In: *25th International Symposium on Space Flight Dynamics, Munich, Germany*. 2015.

[68] Ming Xu, Nan Zhou, and Jinlong Wang. "Robust adaptive strategy for stationkeeping of halo orbit". In: *2012 24th Chinese Control and Decision Conference (CCDC)*. IEEE. 2012, pp. 3086–3091.

[69] Yuri Ulybyshev. "Long-term station keeping of space station in lunar halo orbits". In: *Journal of Guidance, Control, and Dynamics* 38.6 (2015), pp. 1063–1070.

[70] David Hoffman. "Station-keeping at the Collinear Equilibrium Points of the Earth-Moon System". In: *NASA JSC-26189, September* (1993).

[71] David Cielaszyk and Bong Wie. "New approach to halo orbit determination and control". In: *Journal of guidance, control, and dynamics* 19.2 (1996), pp. 266–273.

[72] Min Zhu et al. "Active disturbance rejection station-keeping control of cislunar point orbits". In: IEEE, 2014, pp. 4061–4066.

[73] Aman Narula. "Fault-Tolerant Station keeping on Halo orbit in the Earth-Moon System". MA thesis. Milan: Politecnico di Milano, 2017.

[74] James D. Biggs, Helen C. Henninger, and Aman Narula. "Enhancing station-keeping control with the use of extended state observers". In: *Frontiers in Applied Mathematics and Statistics* 4 (2018), p. 24.

[75] Chuanjiang Li et al. "Stationkeeping Control for Collinear Libration Point Orbits Using NMPC". In: *AAS/AIAA Astrodynamics Specialist Conference*. 2015, pp. 15–692.

[76] Gaurav Misra, Hao Peng, and Xiaoli Bai. "Halo orbit station-keeping using nonlinear MPC and polynomial optimization". In: *2018 Space Flight Mechanics Meeting*. 2018, p. 1454.

[77] Andrew W. Berning Jr et al. "Suboptimal Nonlinear Model Predictive Control Strategies for Tracking Near Rectilinear Halo Orbits". In: *arXiv preprint arXiv:2008.09240* (2020).

[78] Brian L Jones and Robert H Bishop. "H2 optimal halo orbit guidance". In: *Journal of guidance, control, and dynamics* 16.6 (1993), pp. 1118–1124.

[79] Jayant Kulkarni and Mark Campbell. "Asymptotic stabilization of motion about an unstable orbit: application to spacecraft flight in Halo orbit". In: *Proceedings of the 2004 American Control Conference*. Vol. 2. IEEE. 2004, pp. 1025–1030.

[80] Jayant E Kulkarni, Mark E Campbell, and Geir E Dullerud. "Stabilization of Spacecraft Flight in Halo Orbits: An H_infty Approach". In: *IEEE transactions on control systems technology* 14.3 (2006), pp. 572–578.

[81] Steven Craig Gordon. "Orbit determination error analysis and station-keeping for liberation point trajectories". In: *PhDT* (1991).

[82] Kathleen C. Howell and Henry J. Pernicka. "Station-keeping method for libration point trajectories". In: *Journal of Guidance, Control, and Dynamics* 16.1 (1993), pp. 151–159.

[83] Kathleen C Howell and Steven C Gordon. "Orbit determination error analysis and a station-keeping strategy for Sun-Earth L1 libration point orbits". In: *JAnSc* 42.2 (1994), pp. 207–228.

[84] Thomas A Pavlak. "Mission design applications in the Earth-Moon system". MA thesis. Purdue University, 2010.

[85] Thomas Pavlak and Kathleen C Howell. "Strategy for optimal, long-term stationkeeping of libration point orbits in the Earth-Moon system". In: *AIAA/AAS Astrodynamics Specialist Conference*. 2012, p. 4665.

[86] Xiaoli Bai and John L Junkins. "Modified Chebyshev-Picard iteration methods for station-keeping of translunar halo orbits". In: *Mathematical Problems in Engineering* 2012 (2012).

[87] James D. Biggs, Colin R. McInnes, and Thomas Waters. "Control of Solar Sail Periodic orbits in the Elliptic Three-Body Problem". In: *Journal of Guidance, Control, and Dynamics* 32.1 (2009).

[88] Jia Huang, James D Biggs, and Naigang Cui. "Families of halo orbits in the elliptic restricted three-body problem for a solar sail with reflectivity control devices". In: *Advances in Space Research* 65.3 (2020), pp. 1070–1082.

[89] Jia Huang et al. "Integrated guidance and control for solar sail station-keeping with optical degradation". In: *Advances in Space Research* (2020).

[90] Jia Huang, James D Biggs, Naigang Cui, et al. "Station-Keeping for Halo Orbits Using a Solar Sail with One-Degree-of-freedom Electric Propulsion". In: *1st Aerospace Europe Conference (AEC 2020)*. 2020, pp. 1–9.

[91] Yijun Lian et al. "A note on the dynamics around the Lagrange collinear points of the Earth–Moon system in a complete Solar System model". In: *Celestial mechanics and dynamical astronomy* 115.2 (2013), pp. 185–211.

[92] Howard D. Curtis. *Orbital mechanics for engineering students*. Butterworth-Heinemann, 2013.

[93] Bong Wie. *Space vehicle dynamics and control*. American Institute of Aeronautics and Astronautics, 2008.

[94] Meysam Mahooti. *NASA JPL Developement Ephemerides (DE430)*. 2020. URL: `https://www.mathworks.com/matlabcentral/fileexchange/60504-nasa-jpl-developement-ephemerides-de430` (visited on 11/03/2020).

[95] A Romero Calvo, James Biggs, and Francesco Topputo. "Attitude Control for the LUMIO CubeSat in Deep Space". In: *70th International Astronautical Congress (IAC 2019)*. 2019, pp. 1–13.

[96] Stefano Speretta et al. "LUMIO: an autonomous CubeSat for lunar exploration". In: *Space Operations: Inspiring Humankind's Fu ture*. Springer, 2019, pp. 103–134.

[97] Herbert J. Kramer. *Lumio (Lunar Meteoroid Impact Observer)*. 2020. URL: `https://directory.eoportal.org/web/eoportal/satellite-missions/content/-/article/lumio` (visited on 10/17/2020).

[98] Bradford ECAPS. *High Performance Green Propulsion*. 2020. URL: `https://www.ecaps.space/assets/pdf/Bradford_ECAPS_Folder_2017.pdf` (visited on 10/18/2020).

[99] K Anflo and B Crowe. "In-space demonstration of an ADN-based propulsion system". In: *47th AIAA/ASME/SAE/ASEE Joint Propulsion Conference & Exhibit*. 2011, p. 5832.

[100] Gerard Gómez et al. *Dynamics And Mission Design Near Libration Points-Vol I: Fundamentals: The Case Of Collinear Libration Points*. Vol. 2. World Scientific, 2001.

[101] Kathleen C. Howell and Henry J. Pernicka. "Numerical determination of Lissajous trajectories in the restricted three-body problem". In: *Celestial Mechanics* 41.1-4 (1987), pp. 107–124.

[102] Christopher Martin, Bruce A. Conway, and Pablo Ibanez. "Optimal Low-Thrust Trajectories to the Interior Earth-Moon Lagrange Point". In: *Space Manifold Dynamics*. New York: Springer, 2010, pp. 161–184.

[103] David C. Folta et al. "Earth–Moon libration point orbit stationkeeping: theory, modeling, and operations". In: *Acta Astronautica* 94.1 (2014), pp. 421–433.

[104] Vittorio Franzese, Pierluigi Di Lizia, and Francesco Topputo. "Autonomous optical navigation for lumio mission". In: *2018 Space Flight Mechanics Meeting*. 2018, p. 1977.

[105] David Folta and Frank Vaughn. "A survey of earth-moon libration orbits: stationkeeping strategies and intra-orbit transfers". In: *AIAA/AAS Astrodynamics Specialist Conference and Exhibit*. 2004, p. 4741.

[106] Peter Dorato, Vito Cerone, and Chaouki Abdallah. *Linear-Quadratic Control: An Introduction*. New York: Simon & Schuster, Inc., 1994.

[107] Robert Miklosovic, Aaron Radke, and Zhiqiang Gao. "Discrete implementation and generalization of the extended state observer". In: IEEE, 2006, 6–pp.

[108] Zhiqiang Gao. "Scaling and bandwidth-parameterization based controller tuning". In: *Proceedings of the American control conference*. Vol. 6. 2006, pp. 4989–4996.

[109] Jingqing Han. "From PID to active disturbance rejection control". In: *IEEE transactions on Industrial Electronics* 56.3 (2009), pp. 900–906.

This page was intentionally left blank

Appendix A

MATLAB Algorithms

A.1 Multi-Segment Optimization Algorithm

Main Code

```
clear
close all
clc

% Mass Ratio
mu = 1.215059e-2;
% Number of Segments:
ns = 8;
% -- Initial conditions of the optimization parameter, x0
%    The converged solution in the CR3BP (or ER3BP at e = 0):
x_vec_0(:,1) = [1.14375036395082 ,           0      , 0.157506628901084,...
                        0        ,-0.221868821703554,       0          ]';
x_vec_0(:,2) = [1.093998124290866,-0.130591144973532, 0.075986020744445,...
               -0.102043093021459,-0.055978238476017,-0.198618851777981]';
x_vec_0(:,3) = [1.045419753104489, 0.000058622537453,-0.075565387111222,...
               -0.000009622233655, 0.387224067449988, 0.000174602244662]';
x_vec_0(:,4) = [1.094095276098634, 0.130514362792165, 0.076284386663097,...
                0.101952889160582,-0.056570811601691, 0.198328951269294]';
x_vec_0(:,5) = x_vec_0(:,1);
x_vec_0(:,6) = x_vec_0(:,2);
x_vec_0(:,7) = x_vec_0(:,3);
x_vec_0(:,8) = x_vec_0(:,4);
x_vec_0 = reshape(x_vec_0,[ns*6,1]); % Vectorizing
x_vec_0(ns*6+1) = 2*pi/ns;           % Initial segment time, Ts
% -- Initializing x_vec
%    The optimization process considers x_vec_0 as the optimization
%    parameter and not x_vec. Therefore, since x_vec is used as one of the
%    inputs of the utilized functions, it should be given an initial value.
%    However, the initial value is not important because x_vec changes
```

```
%    during the solution.
x_vec = ones(ns*6,1);
% ── Constraining the period to 2*pi
Aeq = [zeros(1,ns*6),ns];
beq = 2*pi;
% ── Optmization Process
start_loop = tic;
for e = 0:(0.0549/50):0.0549
    disp(['e = ', num2str(e)])
    options = optimoptions('fmincon');
     % Adding strict optimization options for the last continuation step
    if e == 0.0549
        options = optimoptions('fmincon', 'MaxFunEvals', Inf,...
            'ConstraintTolerance', 1e-14, 'OptimalityTolerance', 1e-14,...
            'StepTolerance', 1e-14);
    end
    start_iteration = tic;
    x_vec_0 = fmincon(...
        @(x_vec_0) fun_cost(x_vec,ns),x_vec_0,[],[],Aeq,beq,[],[],...
        @(x_vec_0) fun_nonlinear_constraints(x_vec_0,x_vec,ns,e,mu),...
        options);
    disp(['Iteration time = ',...
        num2str(toc(start_iteration)/60),'[min] = ',...
        num2str(toc(start_iteration)),'[sec]'])
end
disp(['Optimization time = ',...
    num2str(toc(start_loop)/3600),'[hr] = ',...
    num2str(toc(start_loop)/60),'[min] = ',...
    num2str(toc(start_loop)),'[sec]'])
% ── Dispalying the results
%%
fprintf('\n\n──────────────────────────────────────────────────────────\n')
fprintf('                    Converged Solution \n')
fprintf('──────────────────────────────────────────────────────────\n')
fprintf('Initial conditions of all segments:\n')
for i = 1:ns
    disp(['x_vec_0(:,',num2str(i),') = ', mat2str(x_vec_0(6*i-5:6*i)),';'])
end
fprintf('\n Segment time:\n')
disp(['x_vec_0(end) = ',num2str(x_vec_0(end))])
disp(['Period = ',num2str(x_vec_0(end)*ns/pi),'*pi [rad]'])
fprintf('──────────────────────────────────────────────────────────\n')

% ── Ploting the results
% Plotting all segments starting from their initial conditions
figure
opts = odeset('RelTol',3e-14,'AbsTol',3e-14);
for i = 1:ns
    [~, x_vec] = ode45(@(t,y) fun_EOM_ER3BP(t,y,e,mu), ...
```

```
        [(i-1)*x_vec_0(6*ns+1) i*x_vec_0(6*ns+1)],x_vec_0(6*i-5:6*i),opts);
    plot3(x_vec(:,1),x_vec(:,2),x_vec(:,3),'LineWidth',1.5), hold on
end
x_L2 = 1.0100740; text(x_L2,0,0,'L2','Color','blue','FontSize',10)
xlabel('x'), ylabel('Y'), zlabel('Z')
xlim([1 1.15])
% Plotting the whole orbit starting from the initial condition of the first
% segment
figure
opts = odeset('RelTol',3e-14,'AbsTol',3e-14);
[~, x_vec] = ode45(@(t,y) fun_EOM_ER3BP(t,y,e,mu), [0 2*pi],...
    x_vec_0(1:6), opts);
plot3(x_vec(:,1),x_vec(:,2),x_vec(:,3),'LineWidth',1.5), grid off, hold on
x_L2 = 1.0100740; text(x_L2,0,0,'L2','Color','blue','FontSize',10)
xlabel('x'), ylabel('Y'), zlabel('Z')
xlim([1 1.15])
```

ODE Function

```
function f_vec = fun_EOM_ER3BP(t, x_vec, e, mu)
%   This function contains the differential equations of the ER3BP
x = x_vec(1);
y = x_vec(2);
z = x_vec(3);
x_dot = x_vec(4);
y_dot = x_vec(5);
z_dot = x_vec(6);

r_1 = norm([x+mu    , y, z]);
r_2 = norm([x-(1-mu), y, z]);

dU_dx = -(1-mu)/(r_1^3)*(x+mu) - mu/r_2^3*(x-(1-mu))+ x;
dU_dy = -(1-mu)/(r_1^3)*y      - mu/r_2^3*y         + y;
dU_dz = -(1-mu)/(r_1^3)*z      - mu/r_2^3*z         - z*e*cos(t);

f_vec = zeros(6,1);
f_vec(1) = x_dot;
f_vec(2) = y_dot;
f_vec(3) = z_dot;
f_vec(4) = (1/(1+e*cos(t)))*dU_dx + 2*y_dot;
f_vec(5) = (1/(1+e*cos(t)))*dU_dy - 2*x_dot;
f_vec(6) = (1/(1+e*cos(t)))*dU_dz;

end
```

Nonlinear Constraints Function

```
function [c, ceq] = fun_nonlinear_constraints(x_vec_0, x_vec, ns, e, mu)
%   This function accounts for the continuity contraints between the
%   segments, such that:
%   the final state of segment i = the initial state of segment i+1
%   in addition, a continuity constraint between the final and first
%   segments were added to obtain a closed orbit.

opts = odeset('RelTol',3e-14,'AbsTol',3e-14);
for i = 1:ns
    [~, x_vec_i] = ode45(@(t,y) fun_EOM_ER3BP(t,y,e,mu),...
        [(i-1)*x_vec_0(6*ns+1) i*x_vec_0(6*ns+1)],x_vec_0(6*i-5:6*i),opts);
    x_vec(6*i-5:6*i) = x_vec_i(end,:)';
    if i < ns
        ceq(6*i-5:6*i,1) = x_vec(6*i-5:6*i,1) - x_vec_0(6*(i+1)-5:6*(i+1));
    elseif i == ns
        ceq(6*i-5:6*i,1) = x_vec(6*i-5:6*i,1) - x_vec_0(1:6);
    end
end
c = [];
end
```

Cost Function

```
function cost = fun_cost(x_vec, ns)
%   This function includes the objective of the optimization process that
%   is to obtain a perpendicular crossing after a complete period

cost = norm([x_vec(ns*6-4),  x_vec(ns*6-2),  x_vec(ns*6)]);
end
```

A.2 Fourier Series Coefficients Algorithm

```
clear
close all
clc

% ── Initial conditions
x_vec_0 = [1.14520421356342;0;0.160866058153171;0;-0.220906655170176;0];
e = 0.0549;       % Eccentricity
mu = 1.215059e-2; % Mass Ratio
% ── State vector propagation for 4*pi
opts = odeset('RelTol',3e-14,'AbsTol',3e-14);
[time, x_vec] = ode45(@(t,y) fun_EOM_ER3BP(t,y,e,mu), [0 4*pi],...
    x_vec_0(1:6), opts);
% ── Fitting the acquired state vector via Fourier Series of the 8th order
Model = 'fourier8';
for i = 1:6
    coeff = coeffvalues(fit(time,x_vec(:,i),Model));
    a0(i) = coeff(1);
    ka = 0;
    kb = 0;
    for j = 2:(length(coeff)-1)
        if rem(j,2)==0
            ka = ka+1;
            a(i,ka) = coeff(j);
        else
            kb = kb+1;
            b(i,kb) = coeff(j);
        end
    end
    w(i) = coeff(end);
end
% ── Display the acquired coefficients
fprintf('\n\n──────────────────────────────────────────────────────────────\n')
fprintf('                Fourier Coefficients \n')
fprintf('──────────────────────────────────────────────────────────────\n')
fprintf('(The lines of the matrices correspond to the state elements)\n\n')
disp('a0 = ')
for i = 1:6
    disp(['   ',mat2str(a0(i))])
end
fprintf('\n')
disp('a = ')
for i = 1:6
    disp(['   ',mat2str(a(i,:))])
end
fprintf('\n')
disp('b = ')
for i = 1:6
```

```
    disp(['   ',mat2str(a(i,:))])
end
fprintf('\n')
disp('w = ')
for i = 1:6
    disp(['   ',mat2str(w(i))])
end
fprintf('————————————————————————————————————————————————————————\n')
%—— Propagating the orbit using the Fourier series
i = 0;
t_end = 1000*pi;
dt = (t_end/(200*(t_end/2/pi)));
for t = 0:dt:t_end
    i = i+1;
    x_vec_F(i,:) = a0(1:3);
    for j = 1:(length(coeff)-2)/2
        for k = 1:3
            x_vec_F(i,k) = x_vec_F(i,k) + a(k,j)*cos(j*t*w(k)) + ...
                                          b(k,j)*sin(j*t*w(k));
        end
    end
end
figure
plot3(x_vec_F(:,1),x_vec_F(:,2),x_vec_F(:,3),'LineWidth',1.5), hold on
x_L2 = 1.0100740; text(x_L2,0,0,'L2','Color','blue','FontSize',10)
xlabel('x'), ylabel('Y'), zlabel('Z')
xlim([1 1.15])
```